

Application of additive manufacturing in vascular self-healing cementitious materials

Wan, Z.

DOI

[10.4233/uuid:7e1ad6f0-ef77-4cef-8f9b-b6fde94988b0](https://doi.org/10.4233/uuid:7e1ad6f0-ef77-4cef-8f9b-b6fde94988b0)

Publication date

2023

Document Version

Final published version

Citation (APA)

Wan, Z. (2023). *Application of additive manufacturing in vascular self-healing cementitious materials*. [Dissertation (TU Delft), Delft University of Technology]. <https://doi.org/10.4233/uuid:7e1ad6f0-ef77-4cef-8f9b-b6fde94988b0>

Important note

To cite this publication, please use the final published version (if applicable).
Please check the document version above.

Copyright

Other than for strictly personal use, it is not permitted to download, forward or distribute the text or part of it, without the consent of the author(s) and/or copyright holder(s), unless the work is under an open content license such as Creative Commons.

Takedown policy

Please contact us and provide details if you believe this document breaches copyrights.
We will remove access to the work immediately and investigate your claim.

APPLICATION OF ADDITIVE MANUFACTURING IN VASCULAR SELF-HEALING CEMENTITIOUS MATERIALS

APPLICATION OF ADDITIVE MANUFACTURING IN VASCULAR SELF-HEALING CEMENTITIOUS MATERIALS

Dissertation

for the purpose of obtaining the degree of doctor
at Delft University of Technology
by the authority of the Rector Magnificus Prof.dr.ir. T.H.J.J. van der Hagen
chair of the Board for Doctorates
to be defended publicly on
Monday 27 November 2023 at 10:00 o'clock

by

Zhi WAN

Master of Engineering in Structural Engineering,
Shandong University, China,
born in Hubei, China.

This dissertation has been approved by the promotors.

Composition of the doctoral committee:

Rector Magnificus,	chairperson
Dr. B. Šavija	Delft University of Technology, promotor
Prof.dr.ir. E. Schlangen	Delft University of Technology, promotor

Independent Members:

Prof.dr.ir. E. Gruyaert	KU Leuven, Belgium
Dr. I.B.C.M. Rocha	Delft University of Technology
Prof.dr. B. Han	Shandong University, China
Prof.dr. H.M. Jonkers	Delft University of Technology
Dr. S.J. Garcia	Delft University of Technology
Prof.dr.ir. P.C. Louter	Delft University of Technology, reserve member



Keywords: Additive manufacturing, Self-healing, Cementitious materials,
Machine learning, Optimization, Printing parameters

Printed by: Ipskamp Printing, the Netherlands

Cover design: Zhi Wan and Rong Wan

Copyright © 2023 by Z. Wan

All rights reserved. This copy of the thesis has been supplied on condition that anyone who consults it is understood to recognize that its copyright rests with its author and that no quotation from the thesis and no information derived from it may be published without the author's prior consent.

ISBN 978-94-6384-503-8

An electronic version of this dissertation is available at
<http://repository.tudelft.nl/>.

To my family

CONTENTS

List of Figures	xi
List of Tables	xvii
Summary	xix
Samenvatting	xxi
1 Introduction	1
1.1 Research background	2
1.1.1 Self-healing materials	2
1.1.2 Vascular self-healing concrete	3
1.2 Research objectives and scope	3
1.2.1 Research objectives	3
1.2.2 Research scope.	3
1.3 Research approach	4
1.4 Research outline	4
References	6
2 Literature review	9
2.1 Introduction of self-healing concretes	10
2.1.1 Autogenous self-healing and stimulated autogenous self-healing	10
2.1.2 Capsule based self-healing.	11
2.1.3 Vascular self-healing.	12
2.2 Components of vascular self-healing concrete	12
2.2.1 concrete mix design	13
2.2.2 Healing agent	13
2.2.3 Vascular materials	15
2.3 Design and fabrication of vascular networks	17
2.3.1 Vascular design based on fluid flow	17
2.3.2 Vascular design based on mechanical properties.	18
2.3.3 Machine learning for design and optimization	19
2.4 Assessment of healing performance.	19
2.4.1 Release of self-healing agent	19
2.4.2 Water tightness recovery	20
2.4.3 Regain in mechanical properties	23
2.5 Summary and concluding remarks	23
References	26

3 Self-healing cementitious materials embedded with 3D-printed ABS vascular networks	33
3.1 Introduction	34
3.2 Experiments	34
3.2.1 Fabrication of vascular networks.	34
3.2.2 Casting, curing and healing process	35
3.2.3 Four-point bending test	37
3.2.4 Water permeability test	38
3.2.5 CT Scanning	39
3.3 Fracture behavior of the composites	39
3.4 Potential influencing factors	40
3.4.1 Influence of the microstructure of vascular network	40
3.4.2 Influence of the macrostructure of vascular network.	41
3.5 Flexural strength recovery.	42
3.5.1 Effect of printing parameters on flexural strength recovery	42
3.5.2 Healing potential of the 4 vascular based self-healing concretes	46
3.6 Water tightness recovery	47
3.6.1 Effect of printing parameters on water tightness of cracked samples.	47
3.6.2 Effect of printing parameters on water tightness recovery	47
3.7 Conclusions.	48
References	50
4 Self-healing cementitious composites with a hollow vascular network created using 3D-printed sacrificial templates	53
4.1 Introduction	54
4.2 Experiments	54
4.2.1 Fabrication and pre-processing of PVA vascular tubes	54
4.2.2 Casting.	56
4.2.3 Removing PVA vascular and curing	57
4.2.4 Healing process	57
4.2.5 Characterization	58
4.3 Influence of printing configuration on dissolution of PVA.	59
4.3.1 Dissolution of one-dimensional PVA tubes.	59
4.3.2 Dissolution of the 3D-printed vascular network	62
4.4 Flexural strength	64
4.4.1 Initial flexural response of vascular self-healing cementitious materials.	64
4.4.2 Strength recovery of the vascular self-healing cementitious composite	65
4.5 Water tightness	67
4.5.1 Recovery of water tightness	67
4.5.2 Crack water permeability after healing	67
4.6 Conclusions.	69
References	70

5	Numerical simulation of self-healing cementitious materials embedded with vascular networks	73
5.1	Introduction	74
5.2	Concrete damaged plasticity model	74
5.3	Simulation of self-healing concrete embedded with ABS vascular networks	75
5.3.1	Calibration for the cementitious matrix	75
5.3.2	Calibration for ABS vascular network	76
5.3.3	Interaction between vascular network and the cementitious matrix	77
5.3.4	The simulation results of cementitious materials with ABS vascular networks	78
5.4	Simulation of self-healing concrete with hollow channels	81
5.4.1	3D Model for self-healing cementitious materials with hollow channels	82
5.4.2	Calibration for 2D model	82
5.4.3	The simulation results of cementitious materials with hollow channels with 2D model	85
5.5	Feasibility of using machine learning for optimization	87
5.6	Conclusions	87
	References	90
6	Optimization of vascular configuration of self-healing cementitious materials using generative deep neural network	93
6.1	Introduction	94
6.2	Data representation and machine learning method	95
6.2.1	Data Representation	95
6.2.2	Artificial neural network (ANN)	95
6.2.3	Inverse design with neural network	98
6.3	Statistical properties of the dataset	99
6.4	Optimization for maximum peak load	100
6.5	Optimization for maximum toughness	104
6.6	Conclusions	107
	References	109
7	Automatic enhancement of vascular configuration for self-healing cementitious materials through reinforcement learning approach	111
7.1	Introduction	112
7.2	Data representation	112
7.2.1	Structure representation	112
7.2.2	Target representation	113
7.3	Markov decision process and Q-learning	113
7.4	Deep Q-learning approach to optimize vascular structures	114
7.4.1	Set of state S and start state s_0	115
7.4.2	Action function and Transition function	116
7.4.3	Reward function	116
7.4.4	Horizon	117

7.4.5	RL Agent	117
7.5	3-pore concrete structure optimization for maximum peak load	118
7.5.1	The optimized structure and frequency	119
7.5.2	Number of visited structures during interaction	120
7.5.3	Change of average reward	121
7.5.4	Loss function of the two Q-networks	122
7.6	3-pore concrete structure optimization for maximum toughness	122
7.6.1	The optimized structure and frequency	122
7.6.2	Number of visited structures during interaction	123
7.6.3	Change of average reward	124
7.6.4	Loss function of the two Q-networks	125
7.7	Application to a new optimization problem	125
7.8	Conclusions	126
	References	128
8	Direct ink writing of vascularized self-healing cementitious materials	129
8.1	Introduction	130
8.2	Materials and setups	130
8.2.1	Mix design of a 3D printable mortar	130
8.2.2	Rheological property of the designed mixture	131
8.2.3	Design of the vascular network	131
8.2.4	Printing process	133
8.2.5	Curing and healing process	134
8.3	Characterization methods	135
8.3.1	CT scanning	135
8.3.2	4-point bending test	135
8.3.3	Water permeability test	136
8.4	Macrostructure of samples with different printing directions	136
8.4.1	Influence of printing direction on the hollow channels	136
8.4.2	Influence of printing direction on the pores	137
8.5	Fracture behavior	139
8.5.1	Initial flexural stress	139
8.5.2	Flexural strength of the healed samples	140
8.6	Water tightness	142
8.7	Conclusions	143
	References	145
9	Conclusions and recommendations	147
9.1	Summary	148
9.2	Conclusions	149
9.3	Recommendations	150
	References	152
	Acknowledgments	153
	Curriculum Vitæ	155
	List of Publications	157

LIST OF FIGURES

1.1	Performance and cost of construction material with time, adapted from [17]. (a) Performance of traditional structures (A: ordinary structures; B: high quality structures); (b) Cost of traditional structures; (c) Performance of structures made with (multiple) self-healing concretes; (d) Cost of structures made with self-healing concretes	2
1.2	Outline of the thesis.	6
2.1	Mechanisms of autogenous self-healing, adapted from [5].	10
2.2	Schematic of self-healing using superabsorbent polymer (SAP), adapted from [14].	11
2.3	Capsule based self-healing concretes, adapted from [22] (a) Paste cylinder; (b) Microcapsules in the cementitious matrix.	11
2.4	(a) Vasculatures in nature, adapted from [28]; (b) Cementitious specimens incorporated with a single tube as vascular network, adapted from [29].	12
2.5	Porous Network Concrete (PNC), adapted from [35].	16
2.6	Design of a 3D vascular network based on Murray's law, adapted from [50].	17
2.7	Tree-shape and grid-shape vascular on disc with one sink in the center, adapted from [57]. (N_R is number of elemental lengths in the radial direction)	18
2.8	Healing agents on cracked surface (a) the crack area covered by the healing agents, adapted from [32]; (b) crack pattern and crack surface, reprinted from [35]; (c) self-healing agent on the surface of crack, adapted from [53];(d) self-healing agent on the surface of crack, adapted from [30].	20
2.9	Release of healing agent from vascular (a) the mortar sample with broken tubes, adapted from [41]; (b) CT image of vascular based SHC, adapted from [50].	20
2.10	Crack closure of self-healing cementitious composites, adapted from [25].	21
2.11	Equipment for water permeability tests, adapted from [76] using (a) falling water level; (b) constant water level (without pressure adjuster); (c) low constant water level; (d) high constant water level (with pressure adjuster).	22
2.12	Crack closure of self-healing cementitious composites, adapted from [77].	22
2.13	Change of UPV as the increase of healing time (BC refers to "before cracking"), adapted from [31].	25
3.1	Schematic figures of vascular network; (a) Periodic unit-cell; (b)Vascular network.	35
3.2	Schematic showing the influence of printing direction on the vascular network.	36

3.3	Schematics of manual healing process.	37
3.4	Four-point bending test setup with horizontal LVDT.	37
3.5	Schematics of permeability test setup.	38
3.6	Flexural response comparison of specimens with different vascular networks (a) L1H; (b) L3H; (c) L1V; (d) L3V.	39
3.7	Printing quality of 3D-printed vascular (a) L1H; (b) L3H; (c) L1V; (d) L3V (the position of the scanned area in the vascular is indicated in the top right corner of each sub-figure).	41
3.8	3D-printed vascular networks, showing the influence of printing parameters on the printing quality of (large visible pores on the photographed surface are circled): (a) L1H (3 large pores); (b) L3H (12 large pores); (c) L1V (4 large pores); (d) L3V (5 large pores). Large pores are circled.	42
3.9	CT Scanning result of L1V.	43
3.10	Healing efficiency of 3D-printed vascular with different printing parameters; (a) flexural strength comparison before and after healing process; (b) healing efficiency (3 samples in each group).	43
3.11	Flexural stress-crack width curve comparison after the first healing process (a) L1H; (b) L3H; (c) L1V; (d) L3V.	44
3.12	Crack morphology after the second 4-point bending test (a) L1H; (b) L3H; (c) L1V; (d) L3V (side view of the specimens).	45
3.13	Flexural strength comparison of specimens (Controlled with constant vertical displacement)	46
3.14	Flow speed of leaked water of specimens with different vascular networks.	47
3.15	Final crack widths of specimens with different vascular networks.	48
4.1	Schematic of samples with PVA tubes fabricated with different configurations.	55
4.2	Schematic of samples embedded with 3D-printed PVA vascular network.	56
4.3	Schematic of manual healing process (3D vascular network).	58
4.4	Schematics of characterization setups (a) 4-point bending test; (b) Permeability test.	58
4.5	Test result from CT scanning, (a) Tubes with different printing direction and wax coating (thickness/radius of 0.2); (b) Tube with different thickness/radius (vertically printed, wax coating).	59
4.6	Fabrication of vascular network (a) schematic of the 2D-/3D- vasculature (orange-PLA, white-PVA); (b) Actual thickness of PVA tube.	62
4.7	CT scans of vascular based self-healing concrete. (a) PVA tube in the 2D vascular network; (b) PVA tube in the 3D vascular network.	63
4.8	Flexural response of specimens embedded with 2D/3D vascular networks.	65
4.9	Comparison of the healed specimens embedded with 2D-/3D- vascular network regarding (a) flexural response; (b) flexural strength.	66
4.10	Water permeability of the cracked specimens after 4-point bending tests; (a) The change of leaked water with time; (b) Water tightness comparison in different healing cycles.	68

5.1	Constitutive law of CDPM in (a) Tension; (b) Compression.	76
5.2	Micro Tension-Compression Testing device during testing of 3D printed ABS bars.	77
5.3	Post failure stress-strain curve of ABS (details depend on the printing parameters, see Table 5.3).	78
5.4	Schematics of numerical model in (a) main view; and (b) perspective view (green: vascular network; gray: the cementitious matrix; black: load cell).	79
5.5	Simulated results of specimens with different vascular networks (a) L1H; (b) L1V; (c) L3H; (d) L3V.	79
5.6	Toughness comparison of specimens with different vascular networks. . .	80
5.7	(a) Inner crack evolution from simulation; (b) crack morphology from simulation and experiment.	81
5.8	Schematics of 3D model for self-healing concrete with hollow tubes (a) Design space of vascular configuration; (b) One example of the simulated structure; (c) flexural response of different structures.	83
5.9	Schematic of 4-pore structure under 3-point bending.	84
5.10	Calibration result for CDPM. (a) Tension; (b) Compression.	84
5.11	Mesh size of the 4-pore structure under 3-point bending.	85
5.12	Mechanical response of different vascular structures of concrete (a) displacement-load curve; (b) some examples of displacement-load curve and the corresponding structure.	86
6.1	Data representation (a) input representation (b) output representation. .	96
6.2	General structure of an Artificial Neural Network (ANN).	97
6.3	Post-processing of ML-recommended input.	99
6.4	The schematic of the corrected GDNN.	100
6.5	(a) Histogram of peak load; (b) Histogram of toughness; (c) structure with the highest peak load; (d) structure with highest toughness (in the 10,000 examples).	101
6.6	Prediction accuracy of peak load.	102
6.7	Change of the average peak load with different correction frequencies (the numbers in the parentheses are learning rate and the correction frequency, respectively).	102
6.8	Histogram of ML-recommended structures (peak load).	103
6.9	ML-recommended structure with highest peak load.	104
6.10	Prediction accuracy of toughness.	105
6.11	Change of toughness with different correction frequencies.	106
6.12	Histogram of ML-recommended structures (toughness).	106
6.13	ML-recommended structure with highest toughness.	107
7.1	Agent-environment interaction in Markov Decision Process (MDP).	114
7.2	Post-processing of ML-recommended input.	115
7.3	Schematic illustration of DQN.	118

7.4	Optimization result of 3-pore structure towards high peak load. (a) Historical best structure during the interaction process; (b) Fraction of the best historical structures; (c) Structure with a peak load of 785.3N; (d) Structure with a peak load of 784.0N.	119
7.5	Number of visited structures. (a) Number of visited structures in different runs; (b) Number of visited examples in Run 8.	120
7.6	Average reward of structure optimization for high peak load.	121
7.7	Loss functions of two Q-networks of structure optimization for high peak load with (a) Updating strategy 1; (b) Updating strategy 2.	122
7.8	Optimization result of 3-pore structure for maximum toughness (a) historical best structure during the interaction process (b) Fraction of the best historical structures; (c) Structure with a toughness of 136.0N-mm; (d) Structure with a toughness of 134.6N-mm.	123
7.9	Number of visited structure (a) Number of visited structures in different runs; (b) Number of visited examples in Run 1.	124
7.10	Average reward of structure optimization for higher toughness over 20 runs.	124
7.11	Loss functions of two Q-networks of structure optimization for maximum toughness with (a) Updating strategy 1; (b) Updating strategy 2.	125
7.12	Optimization result of 4-pore structure towards higher toughness (a) Historical best structure during the interaction process; (b) Structure with highest toughness.	126
8.1	(a) Testing protocol of flow curve; (b) Flow curve; (c) Shear stress under constant shear rate.	132
8.2	Schematic of the 3D-printed mortar with hollow channels. (a) Vascular network; (b) Mortar with vascular networks.	133
8.3	The Stone Flower 3.1 Multi-material 3D printer and its components.	133
8.4	Schematic description of (a) Printing layers; and (b) Printing direction.	134
8.5	Printing process of mortar with hollow channels as vascular networks (longitudinal printing path).	135
8.6	Schematic of 4-point bending test.	136
8.7	Reconstructed CT scan results of 3D-printed mortar with hollow channels. (a) The scanned whole samples; (b) The reconstructed hollow channels; (c) Cross sections in the middle part.	137
8.8	Reconstructed CT scan results of 3D-printed mortar with hollow channels.	138
8.9	Sliced CT results of 3D-printed mortar with hollow channels. (a) Reconstructed hollow channels and pores (black: hollow channels; colorful: small pores); (b) Vertical sections (yellow: matrix; black: hollow channels or small pores).	138
8.10	Volume of small pores of specimens printed in different direction.	139
8.11	Flexural response comparison of specimens printed with different directions.	140

8.12 Flexural response comparison of the healed specimens (a) flexural stress-crack width curve; (b) Flexural strength comparison of healed samples printed in different directions; (c) Healing performance of sample printed in different directions..	141
8.13 Flow speed of leaked water of specimens printed in different directions.	142

LIST OF TABLES

2.1	Previous researches on vascular based SHCs.	24
3.1	Geometric parameters of the periodic unit-cell (mm)	35
3.2	Main printing parameters of four vascular networks	35
3.3	Mix design of the matrix (kg/m^3).	36
3.4	Printing time and weight of the four kinds of vascular networks	40
4.1	Printing time and weight of the four kinds of vascular networks.	55
4.2	The properties of PLA and PVA (provided by Ultimaker).	56
4.3	The technical data sheet of ultra-high molecular weight polyethylene fibre (UHMWPE).	57
4.4	Mix design of the cementitious matrix (kg/m^3).	57
4.5	Photos of the demolded samples (printing configurations: thickness/Radius, printing direction).	60
5.1	Input parameters for cementitious mortar in the CDPM model.	75
5.2	Dimension of the ABS bars tested for calibration (printing parameters refer to Table 3.2).	77
5.3	Input parameters for ABS vascular networks.	78
5.4	Input parameters for fiber reinforced mortar in the CDPM model.	84
5.5	Comparison of numerical model for vascular self-healing cementitious materials.	88
6.1	Statistical properties of the dataset.	100
8.1	Mix design of the 3D printable mortar (kg/m^3).	131

SUMMARY

Self-healing concrete has great potential to enhance the durability of concrete structures without significantly increasing the initial costs. Among the self-healing approaches, vascular self-healing cementitious composite is capable of supplying healing agents to the cracked region in a continuous way or multiple times. However, the use of brittle materials as vascular makes it difficult to create vascular networks with complicated geometry. The recent development of additive manufacturing (AM, also known as 3D printing) promotes the fabrication of complicated vascular system for vascular self-healing materials. However, the application of AM in vascular self-healing cementitious materials is relatively rare. Therefore, this study focuses on understanding the behavior of 3D-printed vascular self-healing concrete with different printing parameters or vascular configurations.

First, it is necessary to investigate the influence of printing parameters on the properties of self-healing cementitious materials with 3D-printed vascular networks. Herein, the vascular networks were additively manufactured using fused filament fabrication with thermoplastic filaments such as Acrylonitrile Butadiene Styrene (ABS) and polyvinyl alcohol (PVA). The properties and healing efficacy of vascular self-healing cementitious materials were compared when the vascular is fabricated with different printing parameters. According to the experimental study, it is noted that the initial properties and mechanical recovery of ABS vascular self-healing cementitious materials are significantly influenced by printing parameters when using epoxy resin as the healing agent. Furthermore, it was feasible to remove the 3D-printed PVA vascular networks embedded in a cementitious matrix when the vascular is coated with paraffin wax with a low melting temperature to prevent its expansive reaction with the cementitious matrix. To realize the full potential of additive manufacturing in vascular self-healing cementitious materials, optimization of vascular configuration is carried out through machine learning (ML) approaches. After comparing three numerical approaches, a 2D model with pores in the middle span is adopted to generate the training dataset for the model. A case study is performed to design the vascular configuration towards higher flexural strength or toughness under the constraint of 3/4 pores are placed in some of the 40 positions in the design space. Based on the obtained results, it is found that vascular configuration has great influences on the mechanical response of vascular self-healing cementitious materials, making the design of vascular configuration necessary. Two ML approaches, i.e., generative deep neural network (GDNN) and deep reinforcement learning (DRL), have proven capable of optimize the vascular configuration. Compared with GDNN, DRL enables automatic enhancement of vascular configuration through the interaction between reinforcement learning (RL) agent and numerical environment.

Finally, instead of printing vascular networks with thermoplastic materials, direct ink writing of vascularized self-healing cementitious materials was performed with a 3D-

printable fiber reinforced mortar. The hardened printed samples were examined with X-Ray tomography (CT scanning) to investigate the influence of printing direction on the structure of hollow channels. Furthermore, the initial properties as well as the healing performance were studied when epoxy resin was employed as the healing agent. It was found that the actual volumes of hollow channels are much smaller than the designed volume due to the squeezing by the upper layers during the printing process. The rough surface of the hollow channels makes it difficult to perform multiple healing events.

This study gives an in-depth investigation on the influence of printing parameter and vascular configuration on the properties of 3D-printed vascular self-healing cementitious materials. Based on the obtained results, additive manufacturing shows great potential to improve the behavior of vascular self-healing cementitious materials by tuning printing parameters and optimizing vascular configurations. Particularly, direct ink writing of vascularized self-healing cementitious materials would be promising to be used in the large-scale concrete infrastructures due to the easy operation.

SAMENVATTING

Zelfherstellend beton heeft een groot potentieel om de duurzaamheid van betonnen constructies te verbeteren zonder dat de initiële kosten aanzienlijk worden verhoogd. Onder de zelfherstellende benaderingen is het vasculaire zelfherstellende cementachtige composiet in staat om herstellende middelen op een continue manier of meerdere keren naar het gescheurde gebied te leveren. Het gebruik van brosse materialen als vasculair element maakt het echter moeilijk om vasculaire netwerken met gecompliceerde geometrie te creëren. De recente ontwikkeling van additive manufacturing (AM, ook bekend als 3D-printen) bevordert de fabricage van gecompliceerde vasculaire stelsels voor vasculaire zelfherstellende materialen. Toch is het gebruik van AM in vasculaire zelfherstellende cementachtige materialen relatief zeldzaam. Daarom richt dit onderzoek zich op het begrijpen van het gedrag van 3D-geprinte vasculaire zelfherstellend beton met verschillende printparameters of vasculaire configuraties.

Ten eerste is het noodzakelijk om de invloed van printparameters op de eigenschappen van zelfherstellende cementachtige materialen met 3D-geprinte vasculaire netwerken te onderzoeken. Hierbij werden de vasculaire netwerken additief vervaardigd met behulp van fusie filamentfabricage met thermoplastische filamenten zoals Acrylonitrile Butadiene Styrene (ABS) en polyvinylalcohol (PVA). De eigenschappen en zelfherstellende effectiviteit van vaatvormige zelfherstellende cementachtige materialen werden vergeleken wanneer het vasculaire stelsel wordt vervaardigd met verschillende printparameters. Uit het experimentele onderzoek is gevonden dat de initiële eigenschappen en mechanische herstel van ABS-vasculaire zelfherstellende cementachtige materialen aanzienlijk worden beïnvloed door printparameters bij gebruik van epoxyhars als herstellend middel. Bovendien was het mogelijk om de 3D-geprinte PVA-vasculaire netwerken in een cementachtige matrix te verwijderen wanneer het vasculaire stelsel is bedekt met paraffinewas met een lage smelttemperatuur om de uitzettingsreactie met de cementachtige matrix te voorkomen.

Om het volledige potentieel van additive manufacturing in vasculaire zelfherstellende cementachtige materialen te realiseren, wordt optimalisatie van de vasculaire configuratie uitgevoerd via machine learning (ML) benaderingen. Na het vergelijken van drie numerieke benaderingen wordt een 2D-model met poriën in het middengebiet aangenomen om de training dataset voor het model te genereren. Een case studie wordt uitgevoerd om de vasculaire configuratie te ontwerpen voor hogere buigsterkte of taaierheid onder de beperking dat 3/4 poriën in sommige van de 40 posities in de ontwerpruimte worden geplaatst. Op basis van de verkregen resultaten is gebleken dat de vasculaire configuratie een grote invloed heeft op de mechanische respons van vasculaire zelfherstellende cementachtige materialen, waardoor het ontwerp van de vasculaire configuratie noodzakelijk is. Twee ML-benaderingen,

namelijk generative deep neural network (GDNN) en deep reinforcement learning (DRL), hebben bewezen in staat te zijn om de vasculaire configuratie te optimaliseren. In vergelijking met GDNN maakt DRL automatische verbetering van de vaatconfiguratie mogelijk door de interactie tussen het reinforcement learning (RL)-agent en de numerieke omgeving.

Tot slot, in plaats van vasculaire netwerken met thermoplastische materialen te printen, werd direct ink writing van vasculaire zelfherstellende cementachtige materialen uitgevoerd met een 3D-printbare vezelversterkte mortel. De uitgeharde geprinte monsters werden onderzocht met X-ray tomografie (CT-scanning) om de invloed van de printrichting op de structuur van holle kanalen te onderzoeken. Bovendien werden de initiële eigenschappen en de zelfherstellende prestaties bestudeerd wanneer epoxyhars als herstellend middel werd gebruikt. Hieruit is gebleken dat de werkelijke volumes van holle kanalen veel kleiner zijn dan het ontworpen volume vanwege het samendrukken door de bovenste lagen tijdens het printproces. Het ruwe oppervlak van de holle kanalen maakt het moeilijk om meerdere herstellende sessies uit te voeren.

Deze studie biedt een diepgaand onderzoek naar de invloed van printparameters en vasculaire configuratie op de eigenschappen van 3D-geprinte vasculaire zelfherstellende cementachtige materialen. Op basis van de verkregen resultaten toont additive manufacturing een groot potentieel om het gedrag van vasculaire zelfherstellende cementachtige materialen te verbeteren door het afstemmen van printparameters en het optimaliseren van vasculaire configuraties. Met name direct ink writing van vasculaire zelfherstellende cementachtige materialen lijkt veelbelovend voor gebruik in grootschalige betonnen infrastructuur vanwege de eenvoudige fabricage.

1

INTRODUCTION

A general introduction regarding the research background is first given in this part. The research goal and scope are then described. Afterwards, the research approaches to the research objectives are briefly addressed. Finally, the technical route of this thesis is presented.

1.1. RESEARCH BACKGROUND

1.1.1. SELF-HEALING MATERIALS

THE self-healing phenomena in nature inspired researchers and engineers to incorporate this property in man-made materials such as polymers [1, 2], metals [3, 4] and construction materials [5–9]. Although self-healing of plants and animals is mainly driven by the vessels or vascular systems, three approaches for self-healing have been developed in the engineering materials: intrinsic healing, capsule based healing and vascular healing [10]. Among others, intrinsic self-healing is mainly attributed to the reaction with the cementitious matrix such as continuing hydration and carbonation. Capsule based self-healing and vascular self-healing are also known as autonomous self-healing since extra components (capsules or vascular systems) are incorporated into the cementitious materials.

Since concrete is the most widely used construction material, a lot of researches has been devoted to promoting its self-healing [11–13]. Compared with traditional concrete structures, structures made with self-healing concrete may be more financially positive over time (Figure 1.1). Except for reducing maintenance costs [14], self-healing concrete could also be applied to inaccessible structures such as underground structures or structures for storage of radioactive waste [15, 16].

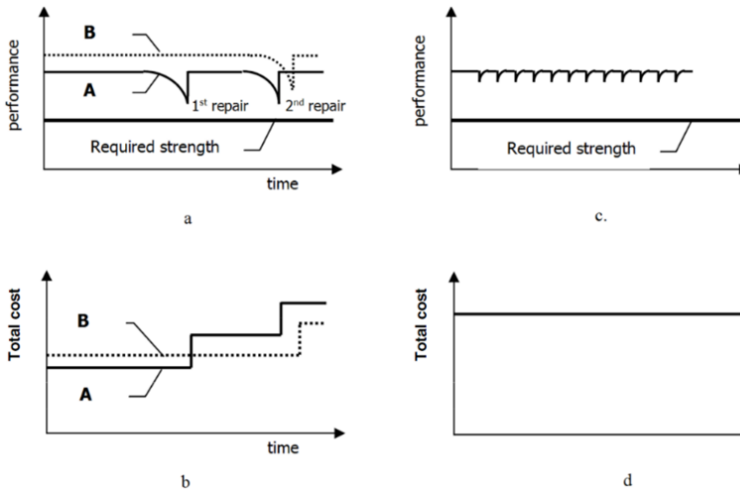


Figure 1.1: Performance and cost of construction material with time, adapted from [17]. (a) Performance of traditional structures (A: ordinary structures; B: high quality structures); (b) Cost of traditional structures; (c) Performance of structures made with (multiple) self-healing concretes; (d) Cost of structures made with self-healing concretes

Considering that the maximum healable crack width of intrinsic self-healing in cementitious materials is less than $300\mu m$, autonomous self-healing has been incorporated in the cementitious matrix by means of encapsulation or vascularization of healing agents. Compared with capsule based self-healing concrete, embedding vascular networks in concrete facilitates a continuous delivery of healing agents from an outside source [18].

1.1.2. VASCULAR SELF-HEALING CONCRETE

For vascular self-healing concrete, first studies focused on embedding one-dimensional (1D) tubes or tabular capsules [19, 20] for transporting healing agents to the cracked regions. To timely trigger the healing process, brittle materials such as borosilicate glass or cementitious hollow tubes are preferred vascular materials [21, 22]. However, their brittleness could also result in rupture during concrete placement. Another option is to use hollow channels or pores in concrete as the transportation pathway for the delivery of healing agents [23]. However, the shape of vascular network (or hollow channels) in those tends to be either simple or impossible to control.

In the past decades, additive manufacturing (AM, also known as 3D printing) has been used in self-healing polymers for creating vascular networks with complicated geometry [24, 25]. These studies have shown that multiple healing cycles can be performed for the self-healing materials with microvascular networks [26]. However, there is currently limited knowledge on application of 3D printing in vascular self-healing cementitious materials. Considering that the printing parameters influence the properties of 3D-printed objects [27–30], it is of great importance to investigate and determine the optimal printing parameters for fabrication of 3D-printed vascular networks in self-healing cementitious materials.

1.2. RESEARCH OBJECTIVES AND SCOPE

1.2.1. RESEARCH OBJECTIVES

THE main objective of this research is to understand the behavior of 3D-printed vascular self-healing cementitious materials with different printing parameters or vascular configurations. To achieve the objective, the following research questions are addressed:

- What is the influence of printing parameters on the properties of self-healing cementitious materials embedded with 3D-printed vascular network?
- How to obtain the mechanical response of self-healing cementitious materials with different vascular configurations using a numerical approach?
- How to optimize the vascular configurations of self-healing cementitious materials under certain constraints?
- What are the possible problems when directly printing the self-healing cementitious materials with hollow channels as the vascular networks?

1.2.2. RESEARCH SCOPE

In this study, the vascular networks are fabricated with a commercial 3D printer (Ultimaker 2+, Utrecht, the Netherlands). Acrylonitrile butadiene styrene (ABS), polylactic acid (PLA) and Polyvinyl alcohol (PVA) filaments are employed as printing materials, which are widely used commercial printing materials. Mortar or fiber reinforced mortar are used as the cementitious matrix considering the size of 3D-printed vascular networks. For 3D-printed cementitious materials with hollow channels, a different commercial 3D printer is employed (Stone Flower 3.1

Multi-material 3D printer). The healing agent used in this study is a two-component epoxy resin which needs to be externally injected. Therefore, the healing agent is manually injected to seal the cracks induced by mechanical tests. The focus of this research is on flexural strength recovery and watertightness recovery of the vascular system, while the long-term durability properties are not discussed.

1.3. RESEARCH APPROACH

To accomplish the research objective, three steps are carried out as follows:

Step 1: Experimental study on self-healing cementitious materials embedded with 3D-printed vascular networks.

Two kinds of commercial printing filaments, i.e., ABS and PVA, are adopted to create the vascular systems for self-healing cementitious materials.

- Investigate the fracture behaviour of self-healing cementitious materials embedded with 3D-printed ABS vascular with different printing parameters.
- Design the optimal printing configurations contributing to the best dissolution of PVA tube incorporated in the cementitious matrix.

Step 2: Numerical simulations and optimization of vascular configurations with machine learning (ML).

Numerical modelling is carried out and the simulated results are compared with the experimental result. Afterwards, ML approaches are developed to optimize the vascular configurations.

- Simulate the 4-point bending tests of self-healing cementitious materials with 3D-printed vasculature using 3D modelling; and simulate 3-point bending test of the notched self-healing cementitious materials with different vascular configurations using 2D modelling.
- Develop machine learning approaches to optimize the vascular configurations of self-healing cementitious materials under the certain constraint.

Step 3: Fabrication of 3D-printed cementitious materials with hollow channels as vascular networks.

- Evaluate the fracture behaviour as well as the healing performance of 3D-printed cementitious materials with hollow channels under different printing parameters.

1.4. RESEARCH OUTLINE

This thesis is divided into five parts (Figure 1.2):

Part I: General introduction and literature review

Chapter 1. The research background, research objectives and scopes, and thesis outline.

Chapter 2. Literature review of vascular self-healing cementitious materials and the challenges of using 3D printing in vascular self-healing cementitious materials.

Part II: Experimental investigation of self-healing cementitious materials embedded with 3D-printed vascular networks

Chapter 3. The fracture behaviour of self-healing cementitious materials incorporating 3D-printed ABS vascular networks created with different printing configurations.

Chapter 4. The influence of printing parameters on the dissolution of 3D-printed PVA tube embedded in the cementitious matrix.

Part III: Simulation and optimization of the self-healing cementitious materials embedded with 3D-printed vascular networks

Chapter 5. Numerical investigation of self-healing cementitious materials with vascular networks.

Chapter 6. Optimization of vascular configuration using generative deep neural network (GDNN).

Chapter 7. Optimization of vascular configuration using deep reinforcement learning (DRL).

Part VI: Development of 3D-printed cementitious materials with hollow channels as vascular network

Chapter 8. A feasibility study of using 3D printing to directly create self-healing cementitious materials incorporated hollow channels to transport healing agents to the cracked region.

Part V: Conclusions and outlook

Chapter 9. The main findings of this research and recommendations for the future work.

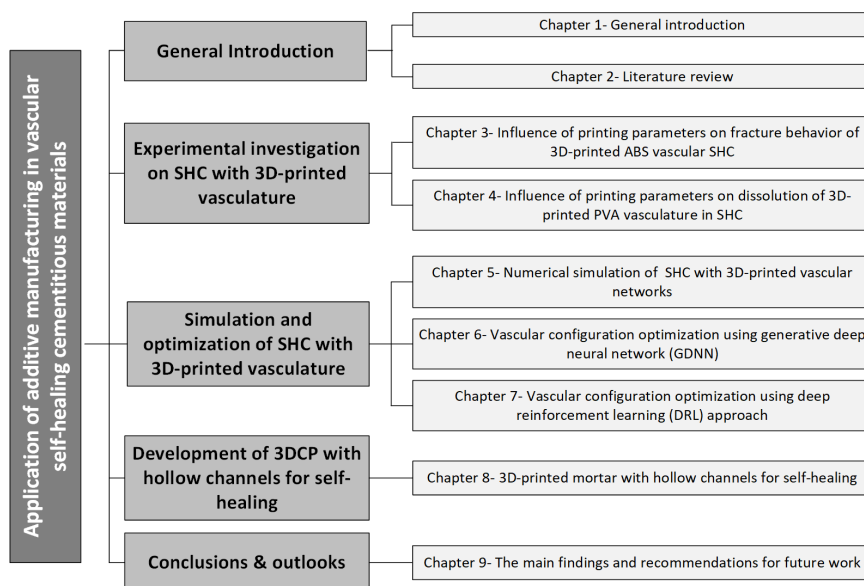


Figure 1.2: Outline of the thesis.

REFERENCES

- [1] M. D. Hager, P. Greil, C. Leyens, S. van der Zwaag, and U. S. Schubert, *Self-healing materials*, *Advanced Materials* **22**, 5424 (2010).
- [2] N. Kuhl, S. Bode, R. K. Bose, J. Vitz, A. Seifert, S. Hoeppener, S. J. Garcia, S. Spange, S. Van Der Zwaag, M. D. Hager, *et al.*, *Acylyhydrazones as reversible covalent crosslinkers for self-healing polymers*, *Advanced Functional Materials* **25**, 3295 (2015).
- [3] N. van Dijk and S. van der Zwaag, *Self-healing phenomena in metals*, *Advanced Materials Interfaces* **5**, 1800226 (2018).
- [4] S. Zhang, N. van Dijk, and S. van der Zwaag, *A review of self-healing metals: Fundamentals, design principles and performance*, *Acta Metallurgica Sinica (English Letters)* **33**, 1167 (2020).
- [5] A. Tabaković and E. Schlangen, *Self-healing technology for asphalt pavements*, *Self-healing materials*, 285 (2016).
- [6] S. Xu, A. García, J. Su, Q. Liu, A. Tabaković, and E. Schlangen, *Self-healing asphalt review: From idea to practice*, *Advanced Materials Interfaces* **5**, 1800536 (2018).
- [7] P. Zhang, Y. Dai, X. Ding, C. Zhou, X. Xue, and T. Zhao, *Self-healing behaviour of multiple microcracks of strain hardening cementitious composites (shcc)*, *Construction and building materials* **169**, 705 (2018).

- [8] P. Zhang, Y. Dai, W. Wang, J. Yang, L. Mo, W. Guo, and J. Bao, *Effects of magnesia expansive agents on the self-healing performance of microcracks in strain-hardening cement-based composites (shcc)*, *Materials Today Communications* **25**, 101421 (2020).
- [9] N. De Belie, E. Gruyaert, A. Al-Tabbaa, P. Antonaci, C. Baera, D. Bajare, A. Darquennes, R. Davies, L. Ferrara, T. Jefferson, *et al.*, *A review of self-healing concrete for damage management of structures*, *Advanced materials interfaces* **5**, 1800074 (2018).
- [10] K. Van Tittelboom and N. De Belie, *Self-healing in cementitious materials—a review*, *Materials* **6**, 2182 (2013).
- [11] E. Tziviloglou, V. Wiktor, H. Jonkers, and E. Schlangen, *Bacteria-based self-healing concrete to increase liquid tightness of cracks*, *Construction and Building Materials* **122**, 118 (2016).
- [12] B. Šavija, J. Feiteira, M. Araújo, S. Chatrabhuti, J.-M. Raquez, K. Van Tittelboom, E. Gruyaert, N. De Belie, and E. Schlangen, *Simulation-aided design of tubular polymeric capsules for self-healing concrete*, *Materials* **10**, 10 (2016).
- [13] B. Dong, G. Fang, Y. Wang, Y. Liu, S. Hong, J. Zhang, S. Lin, and F. Xing, *Performance recovery concerning the permeability of concrete by means of a microcapsule based self-healing system*, *Cement and Concrete Composites* **78**, 84 (2017).
- [14] V. Cappellesso, D. di Summa, P. Pourhaji, N. Prabhu Kannikachalam, K. Dabral, L. Ferrara, M. Cruz Alonso, E. Camacho, E. Gruyaert, and N. De Belie, *A review of the efficiency of self-healing concrete technologies for durable and sustainable concrete under realistic conditions*, *International Materials Reviews* **68**, 556 (2023).
- [15] H. Huang, G. Ye, C. Qian, and E. Schlangen, *Self-healing in cementitious materials: Materials, methods and service conditions*, *Materials & Design* **92**, 499 (2016).
- [16] M. De Rooij, K. Van Tittelboom, N. De Belie, and E. Schlangen, *Self-healing phenomena in cement-Based materials: state-of-the-art report of RILEM technical committee 221-SHC: self-Healing phenomena in cement-Based materials*, Vol. 11 (Springer, 2013).
- [17] K. Van Breugel, *Is there a market for self-healing cement-based materials*, in *Proceedings of the first international conference on self-healing materials* (2007) pp. 1–9.
- [18] P. Minnebo, G. Thierens, G. De Valck, K. Van Tittelboom, N. De Belie, D. Van Hemelrijck, and E. Tsangouri, *A novel design of autonomously healed concrete: Towards a vascular healing network*, *Materials* **10**, 49 (2017).
- [19] H. Huang, G. Ye, and Z. Shui, *Feasibility of self-healing in cementitious materials—by using capsules or a vascular system?* *Construction and Building materials* **63**, 108 (2014).

- [20] A. Formia, S. Terranova, P. Antonaci, N. M. Pugno, and J. M. Tulliani, *Setup of extruded cementitious hollow tubes as containing/releasing devices in self-healing systems*, *Materials* **8**, 1897 (2015).
- [21] M. W. Lee, S. An, S. S. Yoon, and A. L. Yarin, *Advances in self-healing materials based on vascular networks with mechanical self-repair characteristics*, *Advances in Colloid and Interface Science* **252**, 21 (2018).
- [22] A. Formia, S. Irico, F. Bertola, F. Canonico, P. Antonaci, N. M. Pugno, and J.-M. Tulliani, *Experimental analysis of self-healing cement-based materials incorporating extruded cementitious hollow tubes*, *Journal of Intelligent Material Systems and Structures* **27**, 2633 (2016).
- [23] S. Sangadji and E. Schlangen, *Self healing of concrete structures-novel approach using porous network concrete*, *Journal of Advanced Concrete Technology* **10**, 185 (2012).
- [24] A. R. Hamilton, N. R. Sottos, and S. R. White, *Self-healing of internal damage in synthetic vascular materials*, *Advanced Materials* **22**, 5159 (2010).
- [25] J. F. Patrick, K. R. Hart, B. P. Krull, C. E. Diesendruck, J. S. Moore, S. R. White, and N. R. Sottos, *Continuous self-healing life cycle in vascularized structural composites*, *Advanced materials* **26**, 4302 (2014).
- [26] K. S. Toohey, N. R. Sottos, J. A. Lewis, J. S. Moore, and S. R. White, *Self-healing materials with microvascular networks*, *Nature materials* **6**, 581 (2007).
- [27] Y. Xu, H. Zhang, B. Šavija, S. C. Figueiredo, and E. Schlangen, *Deformation and fracture of 3d printed disordered lattice materials: Experiments and modeling*, *Materials & Design* **162**, 143 (2019).
- [28] Y. Xu, H. Zhang, Y. Gan, and B. Šavija, *Cementitious composites reinforced with 3d printed functionally graded polymeric lattice structures: Experiments and modelling*, *Additive Manufacturing* **39**, 101887 (2021).
- [29] E. Tsangouri, C. Van Loo, Y. Shields, N. De Belie, K. Van Tittelboom, and D. G. Aggelis, *Reservoir-vascular tubes network for self-healing concrete: performance analysis by acoustic emission, digital image correlation and ultrasound velocity*, *Applied Sciences* **12**, 4821 (2022).
- [30] Z. Li, L. R. de Souza, C. Litina, A. E. Markaki, and A. Al-Tabbaa, *A novel biomimetic design of a 3d vascular structure for self-healing in cementitious materials using murray's law*, *Materials & Design* **190**, 108572 (2020).

2

LITERATURE REVIEW

The formation of cracks is a major factor in the progressive deterioration of concrete structures. Self-healing concrete (SHC) shows great potential in dealing with the cracks and prolonging the service life of concrete structures. Compared with other healing mechanisms, vascular self-healing enables addressing different scale of cracks as well as performing repetitive healing processes. In this chapter, different approaches to promote self-healing in cementitious materials are first introduced. Afterwards, the focus is on the components of vascular SHCs, i.e., healing agents and vascular materials. Then, the design and fabrication of vascular systems, including traditional vascular creation techniques as well as additive manufacturing (AM), are discussed. In addition, the assessments of healing performance of vascular SHC are presented. Finally, the challenges for further applying AM in vascular SHCs are discussed.

2.1. INTRODUCTION OF SELF-HEALING CONCRETES

IN nature, the survival of living organisms is facilitated by their ability to rapidly heal damages such as wounds or fractures. The self-healing capacity of organisms inspired the development of self-healing systems in polymer-based composites and more recently in cementitious materials [1, 2]. In the case of cement-based infrastructure and construction materials, self-healing could effectively lower the maintenance and repair costs. However, early approaches to the self-healing of concrete mainly involved the stimulation of autogenous healing.

2.1.1. AUTOGENOUS SELF-HEALING AND STIMULATED AUTOGENOUS SELF-HEALING

In 1836, the French Academy of Science was the first to take notice of the autogenous self-healing phenomenon present in cement-based composites [3]. Not much progress has been made until last century when the mechanisms of autogenous self-healing were systematically investigated. Figure 2.1 shows the possible causes of autogenous self-healing of cementitious materials in water. Compared with the physical and mechanical causes, chemical causes are more significant and easier to control. However, the crack sealing capacity induced by the autogenous self-healing is low: healable cracks range is in the size range of 10-100 μm [4].

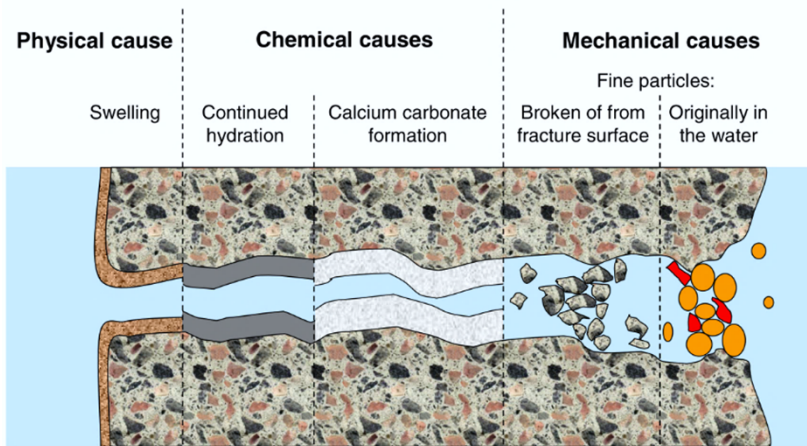


Figure 2.1: Mechanisms of autogenous self-healing, adapted from [5].

To promote the continuing hydration or carbonation of dissolved $\text{Ca}(\text{OH})_2$, a concrete mix can be designed or modified by directly incorporating mineral or crystalline admixtures to stimulate autogenous self-healing [6–11]. Furthermore, the presence of water is another significant stimulator for autogenous self-healing. Superabsorbent polymers (SAP) have been used to induce the self-healing of cementitious materials [4, 12]. The swelling of SAP initially rapidly seals the crack while later providing water for continued hydration which may permanently seal the crack [13]. A schematic of self-healing mechanism using SAP is shown in Figure 2.2 [14].

However, the maximum healable crack width by the simulated autogenous healing is usually less than $300\mu\text{m}$ [15, 16].

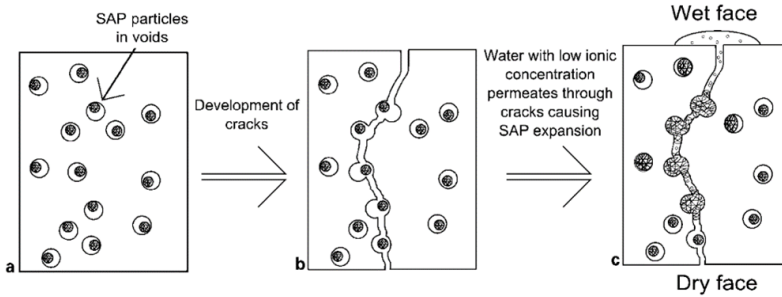


Figure 2.2: Schematic of self-healing using superabsorbent polymer (SAP), adapted from [14].

2.1.2. CAPSULE BASED SELF-HEALING

Compared with embedding engineering additions in the cementitious matrix, encapsulation is a more desired approach due to the higher healing effectiveness. Self-healing concrete incorporated with capsules is termed capsule based self-healing concrete (SHC) in the subsequent discussion. This self-healing process is activated by capsule breakage, caused by e.g., damage. The released healing agents flow to the cracked area and thereby seal the cracks. There are a wide variety of healing agents which could be encapsulated for self-healing. Except for mineral or crystalline admixtures, polymeric healing agents can also be encapsulated [17–21]. An example of capsule based SHC is shown in Figure 2.3 .

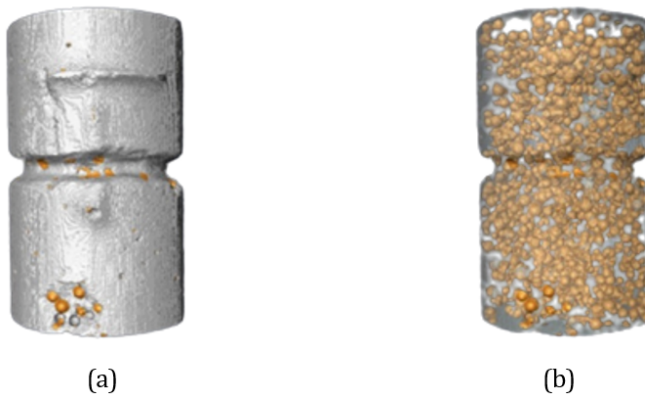


Figure 2.3: Capsule based self-healing concretes, adapted from [22] (a) Paste cylinder; (b) Microcapsules in the cementitious matrix.

Furthermore, microorganisms can be encapsulated to form self-healing bio-concrete in which calcium carbonate is a product of the biological processes which

can seal cracks. The encapsulated bacteria are designed to be dormant until cracks form in the concrete. Due to the high alkaline environment of the cementitious matrix, the selection of bacteria and capsule materials are of great importance [23–25]. Several factors (i.e., curing environment and crack width) affect the precipitation efficiency and the healing effectiveness. For capsule based self-healing concretes, there are two main limitations: (1) the limited supply of healing agent is inappropriate for multiple healing processes [26]; (2) the random and not controlled distribution of capsules resulting from the concrete mixing process.

2.1.3. VASCULAR SELF-HEALING

Inspired by the vascular systems in mammals or leaves of plants (Figure 2.4(a)), incorporating vascular networks in the cementitious matrix enables transporting healing agents to the cracked region (Figure 2.4(b)). Self-healing concrete embedded with vascular networks (or hollow channels) is called vascular self-healing concrete (SHC) in the subsequent discussion. Compared with capsule based SHCs, one of the main advantages of vascular SHC is the ongoing supply of healing agents, facilitating healing of wider cracks and repetitive healing process [27]. However, most vascular systems proposed so far are brittle, which makes the casting of concrete difficult.

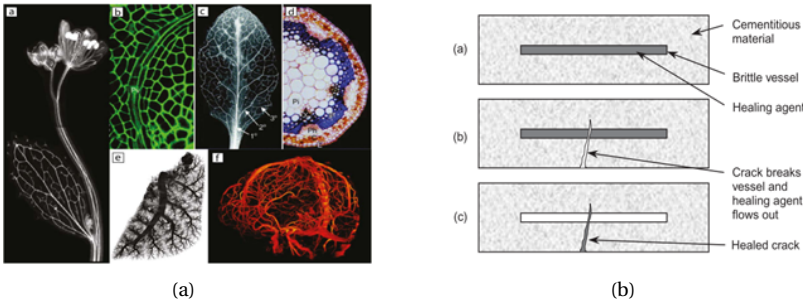


Figure 2.4: (a) Vasculatures in nature, adapted from [28]; (b) Cementitious specimens incorporated with a single tube as vascular network, adapted from [29].

In this chapter, the development of vascular self-healing cementitious composites is reviewed. The main components of vascular cementitious composites, i.e., healing agents and vascular materials, are first introduced. The design and fabrication of vascular systems are then summarized and discussed. In addition, the assessment of healing performance of vascular self-healing cementitious composites is presented. Based on the presented review, the challenges for further applying 3D printing in vascular self-healing concrete are identified.

2.2. COMPONENTS OF VASCULAR SELF-HEALING CONCRETE

FOR vascular self-healing concrete, there are mainly three components, i.e., concrete mix design, healing agents and vascular materials.

2.2.1. CONCRETE MIX DESIGN

Compared with other self-healing approaches in cementitious materials (i.e., capsule based SHC), the regular concrete mix design (for casting) of vascular self-healing concrete can be very similar. It is noting that ductility is needed for the self-healing concrete with pores (or hollow channels) as vascular system. In particular, when paste or mortar is used as the cementitious matrix, fibers could be included to inhibit crack propagation (after unloading) or avoid the vascular self-healing concrete breaking into two halves during the mechanical tests.

Except for cast concrete embedded with 3D-printed vascular network, another option is 3D-printed concrete with vascular system. For 3D concrete printing (3DCP), the printability of cementitious ink should be also addressed. However, due to the limited researches, the concrete mix design for vascular SHC is not discussed in this chapter. Herein, other two major components of vascular SHC, i.e., healing agents and vascular materials are introduced.

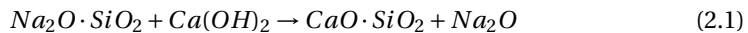
2.2.2. HEALING AGENT

The healing agent in self-healing concrete should have [8]: (1) moderate viscosity; (2) good sealing ability; (3) good mechanical properties (of reactants or hardened healing agents); and (4) long shelf life.

The healing agents for vascular SHC are usually liquid in order to flow to the cracked area through the vascular system. Compared with capsule based SHC, sealing ability and shelf life are less important for most of vascular SHC since the liquid healing agents could be provided from the outside. Four main types of healing agents have been used for vascular SHCs [30]:

- Mineral compounds: saturated calcium hydroxide (CH) solution, sodium silicate (SS) solution and potassium silicate solution.
- Adhesives: cyanoacrylate (CA), methyl methacrylate (MMA), epoxy resin (ER) and others.
- Foam-inducing agents: polyurethane (PU) and PU-based healing agents.
- Water repellent compounds such as silane (SiH_4).

As shown Figure 2.1, an important self-healing mechanism in cementitious composites is continued hydration. Mineral solutions can be provided through a vascular system as healing agents to generate calcium silicate hydrate (C-S-H) by reacting with the cementitious matrix. The chemical reaction when using sodium silicate as the healing agent is illustrated in Equation 2.1.



The main advantages of mineral healing agents are the long-term compatibility with the cementitious matrix, the relatively low viscosity, and ease of handling. Saturated CH solution is used as mineral healing agents due to its environmental benefit and good compatibility with the cementitious matrix. By comparing concretes

embedded with capsules and vascular networks, Huang et al. [31] concluded that the healing efficiency of vascular SHC outperforms the capsule-based counterpart as a result of the ongoing supply of saturated CH solution. Except for CH solution, silicate solution (i.e., another reactant of cement hydration) has also been used as the healing agent to chemically react with CH to seal the cracks. Sodium silicate solution is one of the most widely used healing agents for vascular SHCs for its favourable viscosity and good compatibility with the cementitious matrix. More importantly, it shows a better mechanical recovery compared with other silicates. Silicate solutions have also been modified to improve their performance as healing agents. One example is the potassium silicate solution mixed with amorphous silica nano-powder [32]. Compared with sodium silicate solution, the modified potassium silicate solution exhibits a better affinity with cementitious materials and a lower viscosity. However, silicate solutions have several shortcomings as healing agents. The reaction of silicate healing agents with CH in the cement matrix is slow and significantly influenced by the environment, which hinders its application when fast repair is needed. In addition, its efficiency in terms of mechanical recovery is low [33].

Alternatively, adhesives have been employed as healing agents due to their rapid repair capacity and high efficiency in terms of strength recovery. Instead of reacting with the cementitious matrix, the self-healing event is realized by polymerization of the adhesive, which is less influenced by the environment. Methyl methacrylate (MMA) can be used as a healing agent for SHCs embedded with a vascular system or tubular capsules. For example, MMA has been encapsulated in the brittle fibres to heal the cracks when a damage occurs [17]. Cyanoacrylate (CA, also known as superglue) has been widely used because of its ability to penetrate microcracks due to its exceptionally low viscosity [34]. Joseph et al. [29] found that the peak load of the samples healed with CA is even higher than that of the initial samples. Furthermore, reloading resulted in a formation of a new crack rather than in reopening of the original one which has been healed by CA. Davies et al. [33] compared the healing performance of beam specimens embedded with a 2D vascular network when either CA and SS are used as healing agents. They concluded that the strength recovery of SHC healed with CA is much higher than that of SHC healed with SS solution. However, cyanoacrylate has a short shelf life because of quick hardening when interacting with air.

Two-component epoxy resins (ER) have a longer shelf time, but can also harden rapidly after mixing two components. By comparing the healing performance of different commercial healing agents, Shields et al. [30] found that the specimens healed with epoxy resin show the best recovery of mechanical properties amongst the tested healing agents. Sangadji and Schlangen [35] investigated the self-healing of porous network concrete (PNC) when using epoxy resin as the self-healing agent. In this case, the healed specimens showed a higher tensile strength compared to the virgin specimens.

Except for minerals and adhesives, polyurethane (PU) and water repelling agents (WRA) have also been used as healing agents [34, 36]. Although WRA can effectively prevent water ingress, WRA does not result in recovery of the mechanical properties and only provides a surface coating. On the other hand, PU helps improve the mechanical properties due to its expansive nature. Tsangouri et al. [37] studied the

healing performance of a one-component PU and found that it helps regain more than 70% of the ultimate load and toughness.

2.2.3. VASCULAR MATERIALS

Except for healing agents, the material from which the vascular network is made of also plays an important role in the healing performance of vascular self-healing cementitious composites. The vascular material must be strong enough to survive concrete casting process (especially vibration), and brittle enough to fracture when cracks in concrete occur [38]. Three main types of materials have been used for vascular networks in self-healing concrete:

- Traditional brittle materials: Borosilicate glass, polymethyl methacrylate (PMMA), cementitious hollow tubes and Polyvinyl chloride (PVC).
- Brittle 3D printed materials such as Polylactic acid (PLA) and acrylonitrile butadiene styrene (ABS).
- Sacrificial materials: Heat shrinking tubing or polyurethane tubing, Polyvinyl Alcohol (PVA) and polyolefin.

Borosilicate glass has been widely used as a preferred material for encapsulation because of its brittle behaviour [17, 39]. Glass fibres with liquid healing agents have been incorporated in the cementitious matrix to seal micro-cracks. Sun et al. [40] found that the flexural strength (under 4-point bending) of concrete embedded with glass fibres shows a partial recovery after the healing process. Glass tubes have also been used to transport the healing agents. Joseph et al. [29] investigated concrete specimens with borosilicate capillary tubes of different diameters. Similarly, Van Tittelboom et al. [41] compared the mechanical recovery of samples with glass tubes and ceramic tubes. However, glass is susceptible to alkali-silica reaction, which significantly affects the service life of vascular networks. Alternatively, brittle materials such as polymethyl methacrylate (PMMA), ceramics (alumina) and Polyvinyl chloride (PVC) [42] have been used for creating vascular networks. To improve the compatibility of vascular networks with the cementitious matrix, two shapes of cementitious hollow tubes (i.e., bucatini and maccheroni) have been extruded and included in self-healing concretes [32, 43]. Note that, due to the brittleness of the abovementioned materials, the geometry of the vascular networks tends to be simple (1D).

The development of additive manufacturing (AM) allowed fabricating complicated vascular structures to improve the healing efficiency without significantly lowering the mechanical properties of concrete [27, 30, 44–46]. The selection of printing materials is still vital considering the bonding between the 3D-printed vascular network and the cementitious matrix [47, 48]. Polylactic acid (PLA) is a brittle commercial printing filament and has been employed to create vascular networks for self-healing concrete. De Nardi et al. [49] fabricated mini-vascular networks (MVNs), in which healing agents were stored using PLA. Li et al. [50] compared the cementitious composite embedded with 3D printed PLA vascular networks of three different geometries (1D/2D/3D). A reservoir-vascular network consisting of PLA tubes and a PET reservoir has been

created by Tsangouri et al [37]. ABS filaments have also been used extensively in additive manufacturing due to their exceptional impact resistance. Minnebo et al. [42]. created an integrated vascular system using ABS filaments. They reported that the initial mechanical properties as well as the healing performance are greatly influenced by the printing parameters.

In vascular SHCs, timely rupture of the vascular networks is the precondition for the self-healing event. However, the vascular network should keep its integrity over a long period of time, whereas the alkali-silicate reaction between glass tubes and the cementitious matrix may damage the vascular system. Another option is to create hollow channels inside the host matrix to transport healing agents. This has been first used in self-healing polymers and composites, where sacrificial materials have been used to create the vascular networks of hollow channels [45, 46, 51]. The idea was also tested in vascular SHCs, where solid bars have been placed inside of freshly cast concrete and removed after setting to form hollow channels [52]. A different approach was attempted by Sangadji and Schlangen [35]: inspired by the structure of bones, they placed pre-manufactured porous concrete cylinders inside the centre, allowing the pores to act as the flow pathways for transport of the healing agent (Figure 2.5).

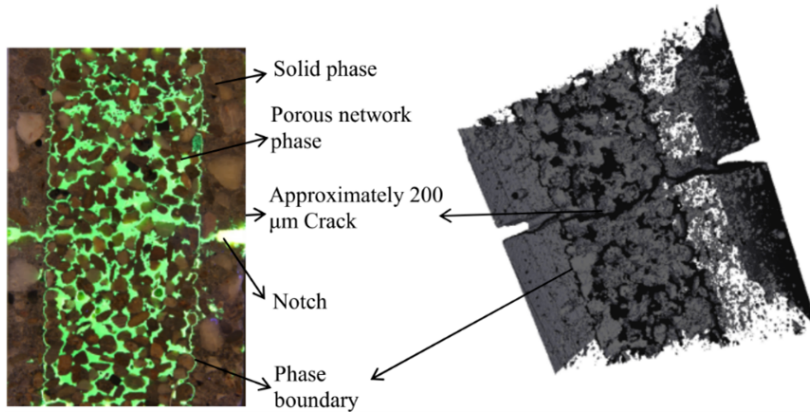


Figure 2.5: Porous Network Concrete (PNC), adapted from [35].

Heat shrinking tubing or polyurethane tubing has also been used to create 2D vascular networks in cementitious materials. Davies et al. [33, 53] fabricated a 2D network with polyolefin tubing in the concrete matrix. Due to the shrinkage of polyolefin tubes at high temperature, the tube can be removed from the specimens with hot water (85°C). Flexible polyurethane terephthalate (PET) tubes were embedded in the cementitious matrix and then removed after the cast specimens were curing for 24h [54]. However, these materials could only be used for creating relatively simple vascular networks. Additive manufacturing has also been used to create hollow tubes using removable printing filaments. Li et al. [55] created vascular systems with Polyvinyl Alcohol (PVA), which is a water soluble printing filament. In the work, they investigated the factors influencing the dissolution of extruded PVA in the highly alkaline environment of the cement paste from the chemical aspect. However, using hollow

channels as the vascular networks decreases the element strength since hollow channels act as imperfections. Therefore, the design of vascular network is of great importance.

2.3. DESIGN AND FABRICATION OF VASCULAR NETWORKS

As the pathway for transporting the healing agents, several aspects need to be considered when designing a vascular system. In some scenarios, the designed vascular system aims at the fast transport of healing agents to the cracked region. But for sometimes, the healing agents could be pumped to the vascular networks, where the fluid flow of healing agents is less important. Since the healing agents used for vascular based self-healing materials are usually liquid, rapid infiltration of healing agents has been prioritized in the design of the vascular configuration.

2.3.1. VASCULAR DESIGN BASED ON FLUID FLOW

After investigating the vascular system in humans, Murray deduced the vascular configuration which needs the least work to transport blood, which is known as Murray's law [56]. When a parent vessel splits into daughter vessels, the relationship could be found in Equation 2.2 :

$$\sum r_p^3 = \sum r_d^3 \quad (2.2)$$

where r_p and r_d are the radii of the parent vessel and the daughter vessel, respectively.

In accordance with this principle, some researchers [37, 50] designed vascular systems for SHCs to reduce the turbulent flow at junctions and enhance the distribution of healing agents. A 3D vascular network based on Murray's law is shown in Figure 2.6.

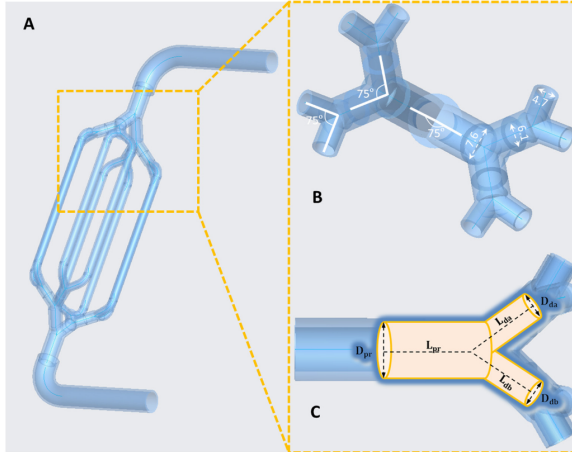


Figure 2.6: Design of a 3D vascular network based on Murray's law, adapted from [50].

Except for minimizing the energy needed for transporting the healing agents, other studies focused on vascular designs for rapid transport of healing agents. Grid

structures consisting of two channel sizes with optimal diameter ratio show significant advantages over other structures since the transportation time of healing agents to all cracked regions is shortened by half [57]. However, for stressed bodies with predetermined crack positions, the tree-shape vascular configuration is a promising alternative due to the decreasing global flow resistance [58]. The two shapes of vascular networks on a disc are shown in Figure 2.7.

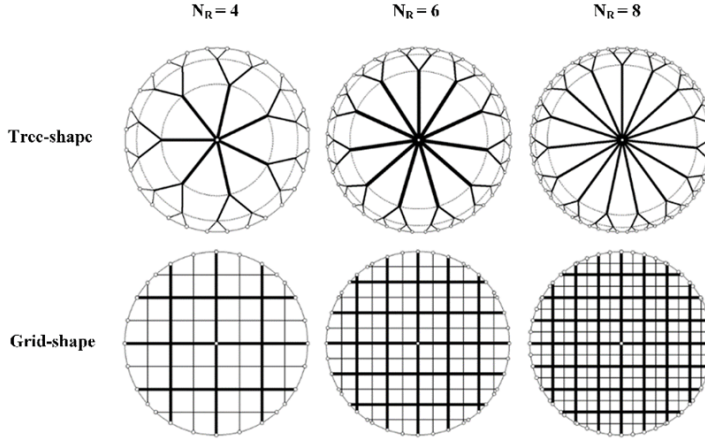


Figure 2.7: Tree-shape and grid-shape vascular on disc with one sink in the center, adapted from [57]. (N_R is number of elemental lengths in the radial direction)

In addition, vascular design in self-cooling systems is also based on fluid flow, and could be used as inspiration for vascular self-healing systems. For example, Yenigun et al. [59] focused on the thermal performance of a channel design with different volume fractions when three types of vascular channels (i.e., parallel channels, tree-shaped and their hybrid) are used. The results indicated that changing the design from parallel channels to tree-shape designs decreases the order of pressure drop. Cetkin et al. [60] demonstrated that vascular structure with radial channels significantly lowers the peak temperature as well as flow resistance for the slab under uniform heat and load.

2.3.2. VASCULAR DESIGN BASED ON MECHANICAL PROPERTIES

In some scenarios, the healing agent is pressurized to facilitate its delivery. According to the Selvarajoo et al. [54], applying pressure to the healing agent results in the increased penetration within a network of cracks and enhanced healing. Therefore, sometimes the vascular configuration is designed to mitigate the adverse influence of vascular networks on the mechanical properties or to improve the healing efficiency. Minnebo et al. [42] developed a piping system consisting of four cementitious tubes in the middle span and 3D-printed ABS pieces in the end. After the bending tests, multiple healing processes were achieved with polyurethane as the healing agent. Considering that the addition of vascular network complicates the casting process, De Nardi et al. [49] designed tetrahedral Mini-Vascular Networks (MVNs) to promote the triggering of healing. Li et al. [50] compared embedded vascular networks with different geometries

(1D/2D/3D) in terms of initial flexural strength and strength recovery, showing that a 3D vascular network outperforms the others due to more connected daughter tubes. The existence of vascular networks, however, may cause stress concentrations in the host matrix. Soghrati et al. [61, 62] concluded that a large volume of voids compromises the mechanical properties of the material after investigating the influence of different volume of voids introduced by a hollow network. Hamilton et al. [27] concluded that a narrower spacing between the vascular channels results in a higher strain in the vicinity of the channels. Therefore, the vascular network should be designed so that there is a balance between the healing efficiency (i.e., vessel coverage) and the mechanical performance (i.e., initial strength) of the composite.

2.3.3. MACHINE LEARNING FOR DESIGN AND OPTIMIZATION

Except for trial-and-error approaches, methods such as evolutionary algorithms and machine learning (ML) could also be employed to design the vascular structures under certain configurations. For example, Argon et al. [63] optimized the vascular arrangement in self-cooling polymeric materials with used a genetic algorithm (GA) which considered factors like network redundancy.

More recently, advances in deep learning and computational resources have enabled the application of machine learning (ML) in material analysis and optimization [64–66]. Instead of using explicit equations to establish the relationship between material structures and properties in a traditional way, some ML algorithms use elements (trees, neurons) to implicitly approximate complex functions [67]. Based on the well-trained ML model, researchers can make relatively precise predictions of properties when similar new structures are given [68, 69]. When the design space is small, the ML-based models perform well for material design by brute force because computation is significantly faster than traditional computational methods such as e.g. finite elements [70].

However, the design space in some applications could be extremely vast, making material design by exhaustive search using ML prediction models very time-consuming or even impossible. Among others, generative inverse design network could help design or optimize material structures [71]. Besides, reinforcement learning (RL) has also shown significant success in solving complex real-world problems in material optimization [72–74]. Compared with other ML algorithms, reinforcement learning can select the actions that maximize the future rewards by iteratively interacting with their operation environment [75]. Besides, the algorithm does not rely on prior knowledge nor the large amount of initialization samples.

2.4. ASSESSMENT OF HEALING PERFORMANCE

2.4.1. RELEASE OF SELF-HEALING AGENT

THE release of healing agents is the precondition for self-healing. Intuitively, a large coverage of healing agent on the cracked surface is likely to contribute to a better healing effectiveness. Consequently, visual observations of the absorbed healing agents on the cracked surface have been used as indicators of healing efficiency (see Figure 2.8) [50, 55].

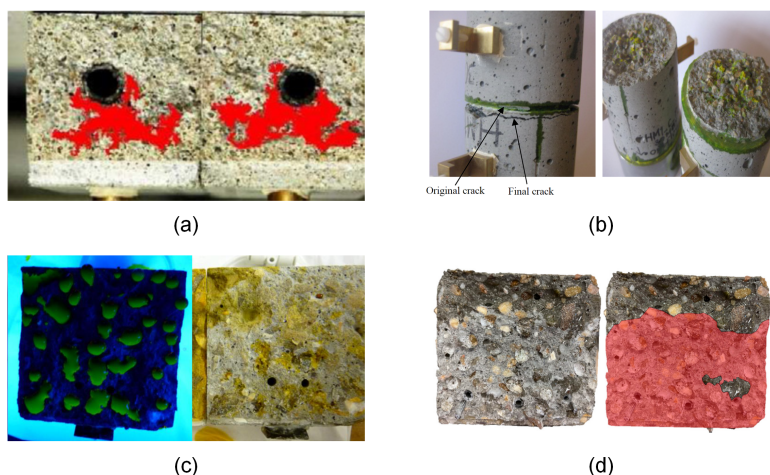


Figure 2.8: Healing agents on cracked surface (a) the crack area covered by the healing agents, adapted from [32]; (b) crack pattern and crack surface, reprinted from [35]; (c) self-healing agent on the surface of crack, adapted from [53]; (d) self-healing agent on the surface of crack, adapted from [30].

However, this method can only be used for evaluating a single healing process: the sample must be broken to observe the crack surface. Therefore, visual observation cannot be applied in cases when multiple healing processes are studied. Other techniques such as X-Ray computed tomography (CT scanning) could instead be employed to assess the release of healing agent from the vascular network [51]. An example is shown in Figure 2.9.

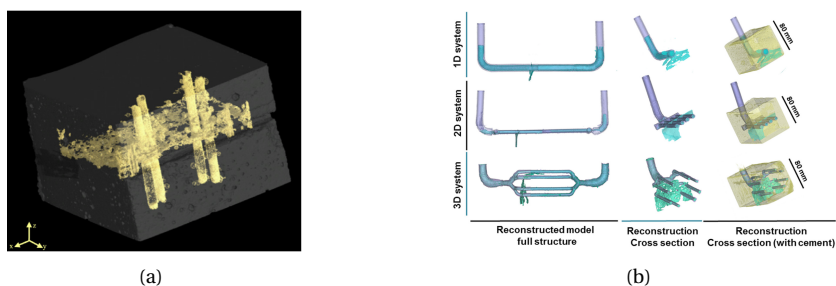


Figure 2.9: Release of healing agent from vascular (a) the mortar sample with broken tubes, adapted from [41]; (b) CT image of vascular based SHC, adapted from [50].

2.4.2. WATER TIGHTNESS RECOVERY

The main purpose of self-healing of cementitious materials is to prolong the service life of concrete structures by retrieving the water/gas tightness [8]. Improved water tightness could prevent the harmful liquids or gasses penetrating the matrix and causing durability problems, e.g., reinforcement corrosion. When using mineral

compounds as healing agents, self-healing of concrete is realized by continued hydration. Crack closure can be observed to qualitatively evaluate the water tightness of the healed samples. An example could be seen in Figure 2.10.

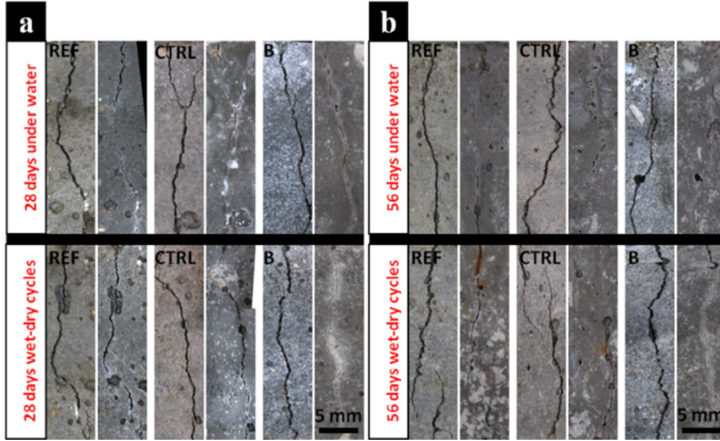


Figure 2.10: Crack closure of self-healing cementitious composites, adapted from [25].

Recovery of water tightness upon self-healing can also be measured quantitatively. The water permeability test can be performed on cracked specimens to calculate the flow rate when the water leaks from the crack with a constant speed [76]. The equipment for water permeability test is shown in Figure 2.11. Water permeability test (with constant head test) has also been used on vascular based SHC [37, 45]. The permeability coefficient can be calculated based on Darcy's law:

$$k = \frac{\alpha T}{At} \ln\left(\frac{h_0}{h_f}\right) \quad (2.3)$$

where α is the cross-sectional area of tube; A is the contact area of water and beam; T and t are beam height and the measurement time respectively; h_0 and h_f are the initial and final water heads, respectively [36].

Except for water permeability tests, water absorption tests based on ASTM C 1587 have also been used to evaluate the water tightness of cracked samples [30, 51]. A specimen for water absorption test and water absorption properties of a cracked specimen are shown in Figure 2.12 [77].

Except for mineral materials, adhesives and foam-inducing agents have also been used as healing agents for vascular based SHC. Instead of generating hydration products, cracks are sealed by the hardened polymers. As a result, the recovery of water tightness tends to be very high in such systems. For example, Shields et al. [30] demonstrated that a high healing efficiency in terms of water tightness is obtained when using epoxy resin and polyurethane as healing agents.

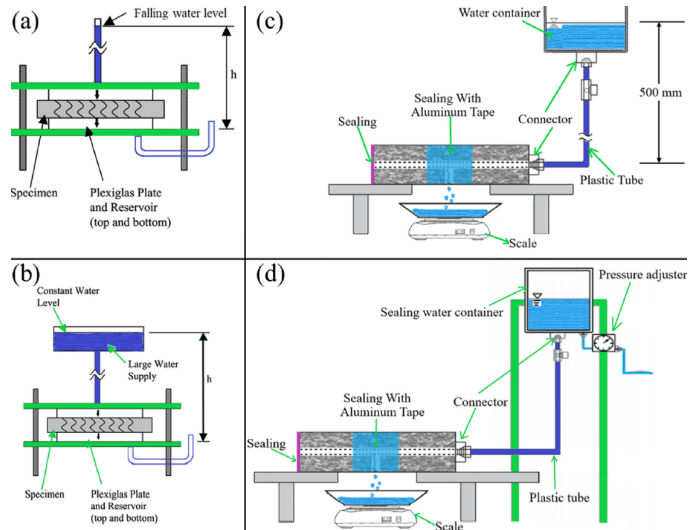


Figure 2.11: Equipment for water permeability tests, adapted from [76] using (a) falling water level; (b) constant water level (without pressure adjuster); (c) low constant water level; (d) high constant water level (with pressure adjuster).

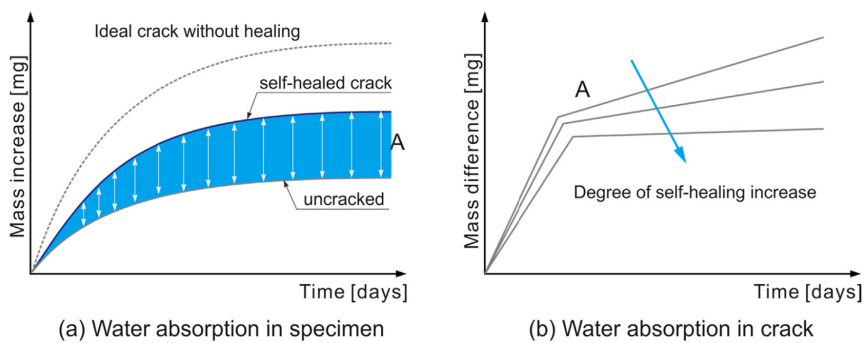


Figure 2.12: Crack closure of self-healing cementitious composites, adapted from [77].

2.4.3. REGAIN IN MECHANICAL PROPERTIES

Mechanical tests such as 3-point bending [29, 32, 33, 35, 43, 44, 50] or 4-point bending tests [43, 45, 51, 52] have often been used to assess the recovery of flexural strength after self-healing. Considering that the hardening time or reaction time of different healing agents varies, the mechanical tests on the healed samples are carried out in different time intervals after the healing process. For adhesives, the waiting time is relatively short considering relatively rapid hardening of polymeric healing agents. For mineral or bacterial healing agents, the regain in mechanical properties is relatively slow. The recovery of mechanical properties is often defined as Equation 2.4 or Equation 2.5.

$$\eta = \frac{p^{healed}}{p^{original}} \times 100\% \quad (2.4)$$

where η is the healing efficiency; $p^{original}$ and p^{healed} are the strength of the virgin and healed specimens, respectively.

$$LRI(\%) = \frac{p_r - p_u}{p_p - p_u} \times 100\% \quad (2.5)$$

where LRI represents the load recovery index; p_p and p_r are the maximum load of the virgin and healed samples, respectively; p_u is the residual load of the virgin samples after unloading.

Except for mechanical tests, non-destructive methods (NDMs) such as ultrasound pulse velocity (UPV) have been used to evaluate the healing efficiency of vascular based SHCs. The recovery of UPV due to self-healing could reflect the healing efficiency. Huang et al. [31] found that the UPV recovers by 15% after the specimens are healed by saturated $Ca(OH)_2$ solution transported by the embedded glass tube (Figure 2.13). Shield et al. [30] concluded that UPV recovery helps demonstrate the strength and toughness recovery after the healing process.

2.5. SUMMARY AND CONCLUDING REMARKS

A summary of different vascular self-healing cementitious composites is given in Table 2.1.

Compared with autogenous self-healing and capsule based self-healing concrete, the main advantage of vascular based self-healing concrete is the continuous supply of healing agents which enables healing wide cracks and even repetitive healing. In this chapter, current developments in the field of vascular based self-healing concrete are reported. From the literature survey, it is noteworthy that additive manufacturing (AM) extends the possibility of fabricating vascular networks with complicated geometry for self-healing. However, to fully utilize the potential of creating vascular structures with AM, some improvements are needed:

- The influence of printing parameters (printing direction, printing layer-height and others) on the properties of vascular self-healing cementitious materials has not been fully understood.
- A limited number of studies focused on the design of vascular network towards higher self-healing capacity.

Table 2.1: Previous researches on vascular based SHCs.

Healing agent	Test methods	Strength recovery	Stiffness recovery	Vascular type	References
Sodium silicate (SS) solution	3-point bending (3PBT)	<0	-	Glass tubes	Shield [30]
SS solution	ultrasound pulse velocity (UPV)	15%	-	Glass tubes	Huang [31]
SS solution	3PBT	20%	75~80%	Mini-vascular networks (MVN)	De Nardi [49]
SS solution	3PBT	17.2%	60.5%	1D channel	Davies [33]
SS solution	4-point bmeding test (4PBT)	30 34%	-	3D-printed PLA tube	Li [50]
SS solution	3PBT	50%	<33%	Cementitious hollow tubes	Formia [43]
SS solution	3PBT	<70.9%	<53.6%	Cementitious hollow tubes	Formia [32]
potassium silicate solution	3PBT	<10.2%	<10.6%	Cementitious hollow tubes	Formia [32]
Cyanoacrylate (CA)	4PBT	>100%	>100%	Borosilicate capillary tube	Joseph [29]
Modified CA	4PBT	<20.2%	-	Glass fibre	Sun [40]
CA	4PBT	<78.6%	69.7%	1D channel	Davies [33]
Polyurethane (PU)	4PBT	>50.0%	>50.0%	Tubular capsules	Titelboom [41]
PU	4PBT	80.0%	71.0%	3D-printed PLA tubes	Tsangouri [37]
PU	3PBT	80.0%	100.0%	piping network	Minnebo [42]
Epoxy resin (ER)	Tension test	>100.0%	>100.0%	Porous network concrete (PNC)	Schlangen [35]

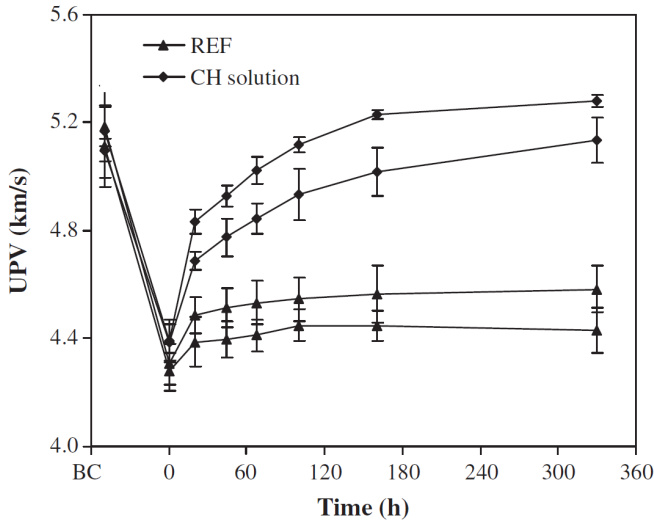


Figure 2.13: Change of UPV as the increase of healing time (BC refers to “before cracking”), adapted from [31].

- Direct ink writing of self-healing cementitious materials with hollow channels as the vascular networks has not been widely investigated.

In the following chapters, these challenges will be addressed.

REFERENCES

- [1] P. Zhang and G. Li, *Advances in healing-on-demand polymers and polymer composites*, Progress in Polymer Science **57**, 32 (2016).
- [2] M. D. Hager, P. Greil, C. Leyens, S. van der Zwaag, and U. S. Schubert, *Self-healing materials*, Advanced Materials **22**, 5424 (2010).
- [3] K. R. Lauer *et al.*, *Autogenous healing of cement paste*, in *Journal Proceedings*, Vol. 52 (1956) pp. 1083–1098.
- [4] N. De Belie, E. Gruyaert, A. Al-Tabbaa, P. Antonaci, C. Baera, D. Bajare, A. Darquennes, R. Davies, L. Ferrara, T. Jefferson, *et al.*, *A review of self-healing concrete for damage management of structures*, Advanced materials interfaces **5**, 1800074 (2018).
- [5] M. De Rooij, K. Van Tittelboom, N. De Belie, and E. Schlangen, *Self-healing phenomena in cement-Based materials: state-of-the-art report of RILEM technical committee 221-SHC: self-Healing phenomena in cement-Based materials*, Vol. 11 (Springer, 2013).
- [6] H. Huang, G. Ye, and D. Damidot, *Effect of blast furnace slag on self-healing of microcracks in cementitious materials*, Cement and concrete research **60**, 68 (2014).
- [7] H. Huang, G. Ye, C. Qian, and E. Schlangen, *Self-healing in cementitious materials: Materials, methods and service conditions*, Materials & Design **92**, 499 (2016).
- [8] K. Van Tittelboom and N. De Belie, *Self-healing in cementitious materials—a review*, Materials **6**, 2182 (2013).
- [9] W. Li, B. Dong, Z. Yang, J. Xu, Q. Chen, H. Li, F. Xing, and Z. Jiang, *Recent advances in intrinsic self-healing cementitious materials*, Advanced Materials **30**, 1705679 (2018).
- [10] L. Ferrara, V. Krelani, and F. Moretti, *On the use of crystalline admixtures in cement based construction materials: from porosity reducers to promoters of self healing*, Smart materials and structures **25**, 084002 (2016).
- [11] L. Ferrara, V. Krelani, and M. Carsana, *A “fracture testing” based approach to assess crack healing of concrete with and without crystalline admixtures*, Construction and Building Materials **68**, 535 (2014).
- [12] C. R. Rodríguez, S. C. Figueiredo, M. Deprez, D. Snoeck, E. Schlangen, and B. Šavija, *Numerical investigation of crack self-sealing in cement-based composites with superabsorbent polymers*, Cement and Concrete Composites **104**, 103395 (2019).
- [13] A. Mignon, D. Snoeck, P. Dubruel, S. Van Vlierberghe, and N. De Belie, *Crack mitigation in concrete: superabsorbent polymers as key to success?* Materials **10**, 237 (2017).

- [14] H. Lee, H. Wong, and N. Buenfeld, *Potential of superabsorbent polymer for self-sealing cracks in concrete*, *Advances in Applied Ceramics* **109**, 296 (2010).
- [15] D. Snoeck, K. Van Tittelboom, S. Steuperaert, P. Dubruel, and N. De Belie, *Self-healing cementitious materials by the combination of microfibres and superabsorbent polymers*, *Journal of Intelligent Material Systems and Structures* **25**, 13 (2014).
- [16] L. Ferrara, T. Van Mullem, M. C. Alonso, P. Antonaci, R. P. Borg, E. Cuenca, A. Jefferson, P.-L. Ng, A. Peled, M. Roig-Flores, *et al.*, *Experimental characterization of the self-healing capacity of cement based materials and its effects on the material performance: A state of the art report by cost action sarcos wg2*, *Construction and Building Materials* **167**, 115 (2018).
- [17] C. Dry, *Three designs for the internal release of sealants, adhesives, and waterproofing chemicals into concrete to reduce permeability*, *Cement and Concrete Research* **30**, 1969 (2000).
- [18] A. Kanellopoulos, P. Giannaros, D. Palmer, A. Kerr, and A. Al-Tabbaa, *Polymeric microcapsules with switchable mechanical properties for self-healing concrete: synthesis, characterisation and proof of concept*, *Smart Materials and Structures* **26**, 045025 (2017).
- [19] C. Xue, W. Li, J. Li, V. W. Tam, and G. Ye, *A review study on encapsulation-based self-healing for cementitious materials*, *Structural Concrete* **20**, 198 (2019).
- [20] Z.-X. Hu, X.-M. Hu, W.-M. Cheng, Y.-Y. Zhao, and M.-Y. Wu, *Performance optimization of one-component polyurethane healing agent for self-healing concrete*, *Construction and Building Materials* **179**, 151 (2018).
- [21] B. Dong, G. Fang, Y. Wang, Y. Liu, S. Hong, J. Zhang, S. Lin, and F. Xing, *Performance recovery concerning the permeability of concrete by means of a microcapsule based self-healing system*, *Cement and Concrete Composites* **78**, 84 (2017).
- [22] L.-Y. Lv, H. Zhang, E. Schlangen, Z. Yang, and F. Xing, *Experimental and numerical study of crack behaviour for capsule-based self-healing cementitious materials*, *Construction and Building Materials* **156**, 219 (2017).
- [23] J.-Y. Wang, N. De Belie, and W. Verstraete, *Diatomaceous earth as a protective vehicle for bacteria applied for self-healing concrete*, *Journal of industrial microbiology and biotechnology* **39**, 567 (2012).
- [24] E. Tziviloglou, Z. Pan, H. M. Jonkers, and E. Schlangen, *Bio-based self-healing mortar: An experimental and numerical study*, *Journal of Advanced Concrete Technology* **15**, 536 (2017).
- [25] E. Tziviloglou, V. Wiktor, H. Jonkers, and E. Schlangen, *Bacteria-based self-healing concrete to increase liquid tightness of cracks*, *Construction and Building Materials* **122**, 118 (2016).

- [26] M. W. Lee, S. An, S. S. Yoon, and A. L. Yarin, *Advances in self-healing materials based on vascular networks with mechanical self-repair characteristics*, *Advances in Colloid and Interface Science* **252**, 21 (2018).
- [27] A. R. Hamilton, N. R. Sottos, and S. R. White, *Self-healing of internal damage in synthetic vascular materials*, *Advanced Materials* **22**, 5159 (2010).
- [28] I. P. Qamar, N. R. Sottos, and R. S. Trask, *Grand challenges in the design and manufacture of vascular self-healing*, *Multifunctional Materials* **3**, 013001 (2020).
- [29] C. Joseph, A. D. Jefferson, B. Isaacs, R. Lark, and D. Gardner, *Experimental investigation of adhesive-based self-healing of cementitious materials*, *Magazine of Concrete Research* **62**, 831 (2010).
- [30] Y. Shields, T. Van Mullem, N. De Belie, and K. Van Tittelboom, *An investigation of suitable healing agents for vascular-based self-healing in cementitious materials*, *Sustainability* **13**, 12948 (2021).
- [31] H. Huang, G. Ye, and Z. Shui, *Feasibility of self-healing in cementitious materials—by using capsules or a vascular system?* *Construction and Building materials* **63**, 108 (2014).
- [32] A. Formia, S. Irico, F. Bertola, F. Canonico, P. Antonaci, N. M. Pugno, and J.-M. Tulliani, *Experimental analysis of self-healing cement-based materials incorporating extruded cementitious hollow tubes*, *Journal of Intelligent Material Systems and Structures* **27**, 2633 (2016).
- [33] R. Davies, T. Jefferson, and D. Gardner, *Development and testing of vascular networks for self-healing cementitious materials*, *Journal of Materials in Civil Engineering* **33**, 04021164 (2021).
- [34] T. Selvarajoo, R. Davies, D. Gardner, B. Freeman, and A. Jefferson, *Characterisation of a vascular self-healing cementitious material system: Flow and curing properties*, *Construction and Building Materials* **245**, 118332 (2020).
- [35] S. Sangadji and E. Schlangen, *Self healing of concrete structures-novel approach using porous network concrete*, *Journal of Advanced Concrete Technology* **10**, 185 (2012).
- [36] K. Van Tittelboom, J. Wang, M. Araújo, D. Snoeck, E. Gruyaert, B. Debbaut, H. Derluyt, V. Cnudde, E. Tsangouri, D. Van Hemelrijck, *et al.*, *Comparison of different approaches for self-healing concrete in a large-scale lab test*, *Construction and building materials* **107**, 125 (2016).
- [37] E. Tsangouri, C. Van Loo, Y. Shields, N. De Belie, K. Van Tittelboom, and D. G. Aggelis, *Reservoir-vascular tubes network for self-healing concrete: performance analysis by acoustic emission, digital image correlation and ultrasound velocity*, *Applied Sciences* **12**, 4821 (2022).

- [38] W. Zhang, Q. Zheng, A. Ashour, and B. Han, *Self-healing cement concrete composites for resilient infrastructures: A review*, Composites Part B: Engineering **189**, 107892 (2020).
- [39] V. C. Li, Y. M. Lim, and Y.-W. Chan, *Feasibility study of a passive smart self-healing cementitious composite*, Composites Part B: Engineering **29**, 819 (1998).
- [40] L. Sun, W. Y. Yu, and Q. Ge, *Experimental research on the self-healing performance of micro-cracks in concrete bridge*, Advanced Materials Research **250**, 28 (2011).
- [41] K. Van Tittelboom, N. De Belie, D. Van Loo, and P. Jacobs, *Self-healing efficiency of cementitious materials containing tubular capsules filled with healing agent*, Cement and Concrete Composites **33**, 497 (2011).
- [42] P. Minnebo, G. Thierens, G. De Valck, K. Van Tittelboom, N. De Belie, D. Van Hemelrijck, and E. Tsangouri, *A novel design of autonomously healed concrete: Towards a vascular healing network*, Materials **10**, 49 (2017).
- [43] A. Formia, S. Terranova, P. Antonaci, N. M. Pugno, and J. M. Tulliani, *Setup of extruded cementitious hollow tubes as containing/releasing devices in self-healing systems*, Materials **8**, 1897 (2015).
- [44] Z. Wan, Y. Xu, Y. Zhang, S. He, and B. Šavija, *Mechanical properties and healing efficiency of 3d-printed abs vascular based self-healing cementitious composite: Experiments and modelling*, Engineering Fracture Mechanics **267**, 108471 (2022).
- [45] K. S. Toohey, N. R. Sottos, J. A. Lewis, J. S. Moore, and S. R. White, *Self-healing materials with microvascular networks*, Nature materials **6**, 581 (2007).
- [46] C. J. Hansen, W. Wu, K. S. Toohey, N. R. Sottos, S. R. White, and J. A. Lewis, *Self-healing materials with interpenetrating microvascular networks*, Advanced Materials **21**, 4143 (2009).
- [47] Y. Xu, H. Zhang, Y. Gan, and B. Šavija, *Cementitious composites reinforced with 3d printed functionally graded polymeric lattice structures: Experiments and modelling*, Additive Manufacturing **39**, 101887 (2021).
- [48] Y. Xu and B. Šavija, *Development of strain hardening cementitious composite (shcc) reinforced with 3d printed polymeric reinforcement: Mechanical properties*, Composites Part B: Engineering **174**, 107011 (2019).
- [49] C. De Nardi, D. Gardner, and A. D. Jefferson, *Development of 3d printed networks in self-healing concrete*, Materials **13**, 1328 (2020).
- [50] Z. Li, L. R. de Souza, C. Litina, A. E. Markaki, and A. Al-Tabbaa, *A novel biomimetic design of a 3d vascular structure for self-healing in cementitious materials using murray's law*, Materials & Design **190**, 108572 (2020).
- [51] C. J. Hansen, S. R. White, N. R. Sottos, and J. A. Lewis, *Accelerated self-healing via ternary interpenetrating microvascular networks*, Advanced Functional Materials **21**, 4320 (2011).

- [52] S. Pareek and A. Oohira, *A fundamental study on regain of flexural strength of mortars by using a self-repair network system*, in *Proceedings of the 3rd International Conference on Self Healing Materials, Bath, UK*, Vol. 2729 (2011).
- [53] R. E. Davies, A. Jefferson, R. Lark, and D. Gardner, *A novel 2d vascular network in cementitious materials*, (2015).
- [54] T. Selvarajoo, R. Davies, B. Freeman, and A. Jefferson, *Mechanical response of a vascular self-healing cementitious material system under varying loading conditions*, *Construction and Building Materials* **254**, 119245 (2020).
- [55] Z. Li, L. R. d. Souza, C. Litina, A. E. Markaki, and A. Al-Tabbaa, *Feasibility of using 3d printed polyvinyl alcohol (pva) for creating self-healing vascular tunnels in cement system*, *Materials* **12**, 3872 (2019).
- [56] C. D. Murray, *The physiological principle of minimum work applied to the angle of branching of arteries*, *The Journal of general physiology* **9**, 835 (1926).
- [57] A. Bejan, S. Lorente, and K.-M. Wang, *Networks of channels for self-healing composite materials*, *Journal of Applied Physics* **100** (2006).
- [58] K. Wang, S. Lorente, and A. Bejan, *Vascularization with grids of channels: multiple scales, loops and body shapes*, *Journal of Physics D: Applied Physics* **40**, 4740 (2007).
- [59] O. Yenigun and E. Çetkin, *Experimental and numerical investigation of constructal vascular channels for self-cooling: Parallel channels, tree-shaped and hybrid designs*, *International Journal of Heat and Mass Transfer* **103**, 1155 (2016).
- [60] E. Cetkin, S. Lorente, and A. Bejan, *Hybrid grid and tree structures for cooling and mechanical strength*, *Journal of Applied Physics* **110** (2011).
- [61] S. Soghrati, P. R. Thakre, S. R. White, N. R. Sottos, and P. H. Geubelle, *Computational modeling and design of actively-cooled microvascular materials*, *International Journal of Heat and Mass Transfer* **55**, 5309 (2012).
- [62] A. M. Aragón, R. Saksena, B. D. Kozola, P. H. Geubelle, K. T. Christensen, and S. R. White, *Multi-physics optimization of three-dimensional microvascular polymeric components*, *Journal of Computational Physics* **233**, 132 (2013).
- [63] A. M. Aragón, J. K. Wayer, P. H. Geubelle, D. E. Goldberg, and S. R. White, *Design of microvascular flow networks using multi-objective genetic algorithms*, *Computer Methods in Applied Mechanics and Engineering* **197**, 4399 (2008).
- [64] F. Pedregosa, G. Varoquaux, A. Gramfort, V. Michel, B. Thirion, O. Grisel, M. Blondel, P. Prettenhofer, R. Weiss, V. Dubourg, *et al.*, *Scikit-learn: Machine learning in python*, *the Journal of machine Learning research* **12**, 2825 (2011).
- [65] Z. Li, J. Yoon, R. Zhang, F. Rajabipour, W. V. Srubar III, I. Dabo, and A. Radlińska, *Machine learning in concrete science: applications, challenges, and best practices*, *npj Computational Materials* **8**, 127 (2022).

- [66] Q. Yu, P. Spiesz, and H. Brouwers, *Ultra-lightweight concrete: Conceptual design and performance evaluation*, Cement and Concrete Composites **61**, 18 (2015).
- [67] D.-W. Kim, J. H. Lim, and S. Lee, *Prediction and validation of the transverse mechanical behavior of unidirectional composites considering interfacial debonding through convolutional neural networks*, Composites Part B: Engineering **225**, 109314 (2021).
- [68] I.-C. Yeh, *Modeling of strength of high-performance concrete using artificial neural networks*, Cement and Concrete research **28**, 1797 (1998).
- [69] C. Yang, Y. Kim, S. Ryu, and G. X. Gu, *Prediction of composite microstructure stress-strain curves using convolutional neural networks*, Materials & Design **189**, 108509 (2020).
- [70] G. X. Gu, C.-T. Chen, D. J. Richmond, and M. J. Buehler, *Bioinspired hierarchical composite design using machine learning: simulation, additive manufacturing, and experiment*, Materials Horizons **5**, 939 (2018).
- [71] C.-T. Chen and G. X. Gu, *Generative deep neural networks for inverse materials design using backpropagation and active learning*, Advanced Science **7**, 1902607 (2020).
- [72] N. K. Brown, A. P. Garland, G. M. Fadel, and G. Li, *Deep reinforcement learning for engineering design through topology optimization of elementally discretized design domains*, Materials & Design **218**, 110672 (2022).
- [73] F. Sui, R. Guo, Z. Zhang, G. X. Gu, and L. Lin, *Deep reinforcement learning for digital materials design*, ACS Materials Letters **3**, 1433 (2021).
- [74] C. Qiu, S. Du, and J. Yang, *A deep learning approach for efficient topology optimization based on the element removal strategy*, Materials & Design **212**, 110179 (2021).
- [75] R. S. Sutton and A. G. Barto, *Reinforcement learning: An introduction* (MIT press, 2018).
- [76] S. Hou, K. Li, Z. Wu, F. Li, and C. Shi, *Quantitative evaluation on self-healing capacity of cracked concrete by water permeability test—a review*, Cement and Concrete Composites **127**, 104404 (2022).
- [77] B. Park and Y. C. Choi, *Quantitative evaluation of crack self-healing in cement-based materials by absorption test*, Construction and Building Materials **184**, 1 (2018).

3

SELF-HEALING CEMENTITIOUS MATERIALS EMBEDDED WITH 3D-PRINTED ABS VASCULAR NETWORKS

In this chapter, 3D vascular structures with complex geometry were designed and printed with different printing parameters (printing direction: horizontal, vertical; printing layer-height: 0.1mm, 0.3mm). First, the influence of the four, nominally identical, vascular networks on the initial flexural strength of self-healing concretes was experimentally investigated. After the 4-point bending tests, epoxy resin was injected into the vascular networks to seal the cracks. Then, flexural strength regain and water tightness recovery were measured. The results show that vascular self-healing cementitious materials have lower initial flexural strengths than the reference sample, as expected. The magnitude of the strength drop depends on the printing parameters. In terms of water tightness recovery, all tested vascular self-healing samples showed a full (100%) recovery, which means that the printing direction and printing layer-height do not influence the water tightness recovery. Overall, the designed 3D-printed vascular self-healing cementitious materials show remarkable strength regain and water tightness recovery.

3.1. INTRODUCTION

COMPARED with other fabrication techniques, additive manufacturing (AM) enables creation of complex vascular networks in self-healing cementitious composites [2, 3]. Similar to the vessel system in animals, vascular networks with different hierarchy in self-healing cementitious materials are expected to be more functional without significantly reducing the initial properties (mechanical strengths or permeability). According to a recent study [4], 3D vascular networks in self-healing cementitious materials show a better healing efficiency and strength recovery compared with 1D or 2D vascular networks. In previous studies, most researchers attached importance on the influence of printing materials or healing agents on the healing efficiency, while disregarding the effect of printing parameters [5–7]. Common 3D printing techniques, such as fused deposition modelling (FDM), are layer-by-layer processes, and result in anisotropy of the material properties and imperfections (voids, pores) on different length scales, depending on the printing parameters [8]. This may have an impact on the healing efficiency as well as the mechanical properties of the cementitious materials with vascular networks. The adverse influence of the embedded vascular networks on the initial properties of self-healing cementitious materials should be minimized. In this chapter, the influence of printing parameters on the strength regain and water tightness recovery of vascular self-healing cementitious materials was studied. Based on a previous research [9], an octet-structural vascular network was designed and printed using different printing parameters. The strength regain and water tightness recovery of the four vascular self-healing cementitious materials was compared to evaluate the influence of printing parameters. Furthermore, the strength recovery potential of the four vascular self-healing cementitious materials was investigated by analyzing the flexural strength before and after two healing processes.

3.2. EXPERIMENTS

3.2.1. FABRICATION OF VASCULAR NETWORKS

TO improve the healing efficiency and enable multiple healing process, an octet-structure lattice is designed as the vascular network for self-healing cementitious materials. In the designed vascular system, there are 4 or 8 connecting paths for each node. The added redundancy allows healing agents to reach the cracked region through different routes even if some channels are blocked during casting process. Furthermore, the multiple channels between two nodes also enable multiple healing processes even if some channels are blocked during the previous healing process. In addition, the designed vascular network helps increase the ductility of concrete by increasing crack tortuosity. The schematic figure of a periodic unit-cell is shown in Figure 3.1(a). Herein, D , d and t refer to the outer diameter, the inner diameter, and the thickness of the vascular, respectively. The geometric parameters are listed in Table 3.1. The vascular network consists of four-unit cells (Figure 3.1(b)).

To investigate the influence of two main printing parameters, i.e., printing layer-height and printing direction (Figure 3.2), four sets of vascular networks are printed with Acrylonitrile Butadiene Styrene (ABS) filament using a commercial 3D printer Ultimaker 2+ (Ultimaker, Utrecht, The Netherlands). ABS filament is widely

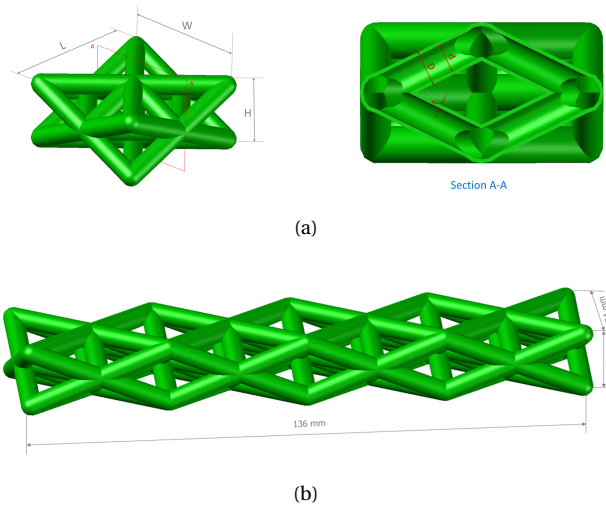


Figure 3.1: Schematic figures of vascular network; (a) Periodic unit-cell; (b) Vascular network.

Table 3.1: Geometric parameters of the periodic unit-cell (mm)

Parameters	L	W	H	D	d	t
Value	34	34	14	5	4	0.5

used in 3D printing for its good interlayer adhesion and high chemical resistance [10]. The printing parameters of the four ABS vascular are listed in Table 3.2.

3.2.2. CASTING, CURING AND HEALING PROCESS

The matrix mixture uses ordinary Portland cement (CEM I) blended with fly ash, which results in good workability needed to fill the spaces between the tubes of the vascular. In addition, fly ash may also help increase the healing capacity of the matrix due to the continuous hydration in the late-age stage [11–13]. The mix proportions are taken from [9] and are listed in Table 3.3. It should be noted that no additional reinforcement was added in the matrix except the ABS vascular networks. Except the four vascular self-healing concretes, a plain cementitious mortar (i.e., without the vascular network) is employed as the reference in the study.

Table 3.2: Main printing parameters of four vascular networks

Sample number	L1H	L1V	L3H	L3V
Layer-height (mm)	0.1	0.1	0.3	0.3
Printing direction	horizontal	vertical	horizontal	vertical
Temperature (°C)		250		
Nozzle size (mm)		0.4		
Printing speed (mm/s)		30		

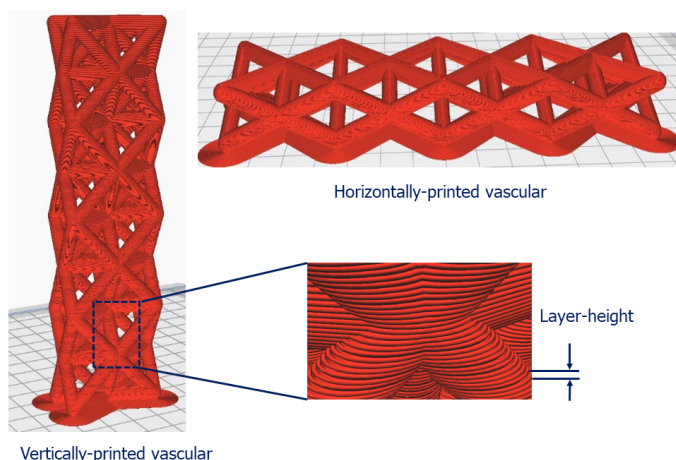


Figure 3.2: Schematic showing the influence of printing direction on the vascular network.

Table 3.3: Mix design of the matrix (kg/m^3).

CEM I 42.5 N	Fly ash	Sand (0.125-0.25mm)	Superplasticizer (Glenium 51)	Water
550	650	550	2	395

The casting process was as follows: (1) the vascular network was positioned in the foam molds; (2) cement, fly ash and sand were dry-mixed for 4 minutes in a Hobart blender. (3) superplasticizer and water were added to the dry components and mixed for 4 minutes; (4) The mixed materials were poured in the foam molds with a dimension of $160mm \times 40mm \times 25mm$ ($L \times W \times H$) and vibrated for 30 seconds; (5) The specimens were covered by a plastic film to prevent water evaporation and kept in room temperature for 24 hours; (6) The specimens were demolded and cured in a curing chamber ($96\% \pm 2\%RH$, $20 \pm 2^\circ C$) for 27 days before the first round of mechanical tests.

When specimens cracked after the 4-point bending tests, epoxy resin was used as the healing agent for its favorable healing performance [14–16]. Specifically, Epoxy resin (Conpox Resin BY 158, Condor Kemi A/S) and hardener (Conpox Hardener BY 2996, Condor Kemi A/S) were first weighted and mixed with a mass ratio of 3:1 and stirred for 1 minute. Then, epoxy resin was manually injected into the vascular networks from one inlet using a syringe. Note that the healing agent is not pressurized into the sample. In other words, the epoxy resin flows into the cracks only under gravity and capillary pressure. The amount of epoxy resin is taken as $5ml$ since this ensures enough epoxy resin to reach the crack regions in the experiments. The schematics of the manual healing process is shown in Figure 3.3. The treated samples were kept in room temperature for 24 hours until the injected epoxy resin was fully hardened. Three samples were tested in each group.

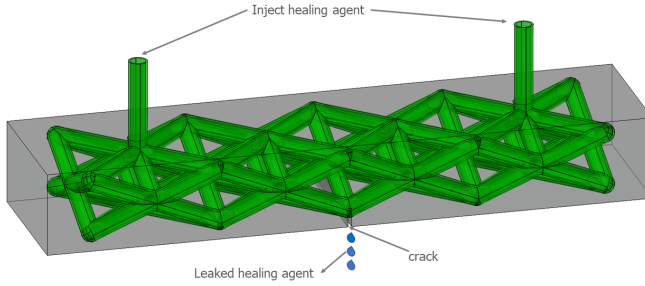


Figure 3.3: Schematics of manual healing process.

3.2.3. FOUR-POINT BENDING TEST

Four-point bending tests were carried out by a servo hydraulic press (INSTRON 8872) to evaluate the initial flexural strength and strength regain of the ABS-printed vascular self-healing cementitious materials. Considering that the samples with same octet structures (but solid structures) have only one crack during the 4-point bending tests in [9], one crack is expected in this study. The specimens were loaded with crack opening displacement (COD) control to a predefined maximum crack width. The crack opening speed is set to $1\mu\text{m/s}$, similar to previous studies [17]. The original specimens were loaded until crack width reached $500\mu\text{m}$. The measurement of crack opening displacement continues to be recorded until the load roller of the hydraulic press ceases contact with the tested samples. The crack widths of the specimens after unloading were recorded as the final crack widths. After the healing process, the specimens were loaded again until the crack width reached $300\mu\text{m}$. The setup of 4-point bending test with two horizontal Linear Variable Differential Transformers (LVDTs) is shown in Figure 3.4.

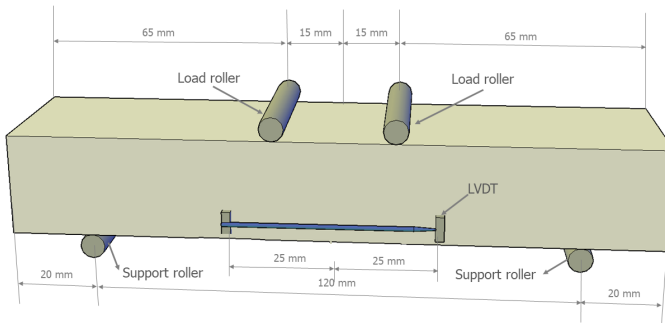


Figure 3.4: Four-point bending test setup with horizontal LVDT.

Considering that the deflection of the samples becomes very large, and the

measurement of the crack width becomes inaccurate when the accumulated crack width reaches $800\mu\text{m}$, the 4-point bending test was controlled by a constant crack opening speed only for a single healing process.

To investigate the strength recovery potential for multiple healing process, an additional series of 4-point bending test controlled by a constant vertical displacement speed of 0.01mm/s was carried out where the specimens were injected epoxy resin for two healing rounds. In each 4-point bending test, the specimens were loaded until the bearing load is less than 0.1kN . The maximum flexural strength in each test was recorded and compared.

3.2.4. WATER PERMEABILITY TEST

Another problem caused by cracks in concrete is leakage, which may induce corrosion of the reinforcement and shorten the service life. Therefore, water permeability was also employed as a metric to evaluate the healing efficiency of the 3D-printed vascular self-healing cementitious materials.

The permeability testing method proposed in [18, 19] was used in this study. Particularly, one inlet of the vascular network on the upper surface of samples was sealed by silicone glue while the other was connected to one end of a tube. The other end of the tube was connected to a water container with a water head of 0.5m from the upper surface of the tested specimens. The schematics of the experimental setup for permeability evaluation is shown in Figure 3.5. The steady flow speed of leaked water was automatically recorded and compared to analyze the influence of vascular on the water tightness properties of concrete. The permeability test was carried out before and after injecting the epoxy resin. Note that if the injected epoxy resin does not fill (or reach) the crack (i.e., there is no leaked water), it should be concluded that only the tube (or vascular) is blocked and the crack is not sealed.

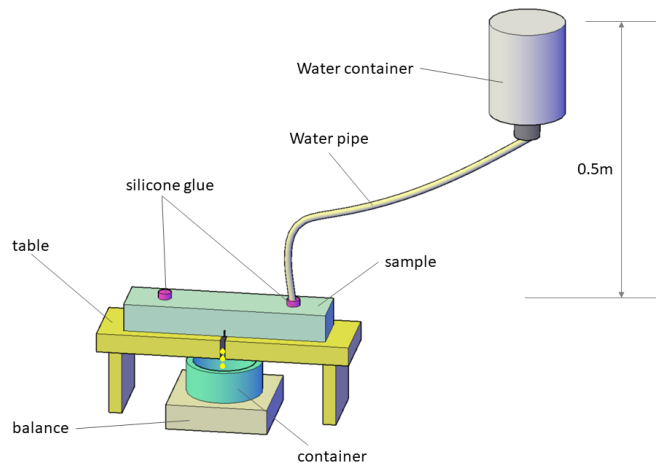


Figure 3.5: Schematics of permeability test setup.

3.2.5. CT SCANNING

A micro-CT scanner (Phoenix Nanotom) was used to observe the influence of printing parameters on the printing quality of vascular network [20]. First, the microstructures of hollow bars with 4 different printing parameters (2 printing directions: horizontal and vertical; 2 printing layer-heights: 0.1mm and 0.3mm) were observed. The microstructures were reconstructed by using the dedicated Phoenix Dotos software. The resolution of the obtained slice for hollow tubes is $3\mu\text{m}$. In addition, the hardened samples embedded with 4 vascular networks were scanned to observe the inner structure of vascular network with the resolution of $27.5\mu\text{m}$.

3.3. FRACTURE BEHAVIOR OF THE COMPOSITES

FRACTURE behavior is crucial for self-healing materials. The stress-crack width (CMOD) curves of 4 different specimens are compared with the references (specimens without vascular networks). The experimental results of specimens under 4-point bending test are shown in Figure 3.6. For all 4 different designs, after the first cracking, a hardening branch can be observed. The extent of this hardening branch is dependent on the printing parameters, although all vascular designs are nominally identical.

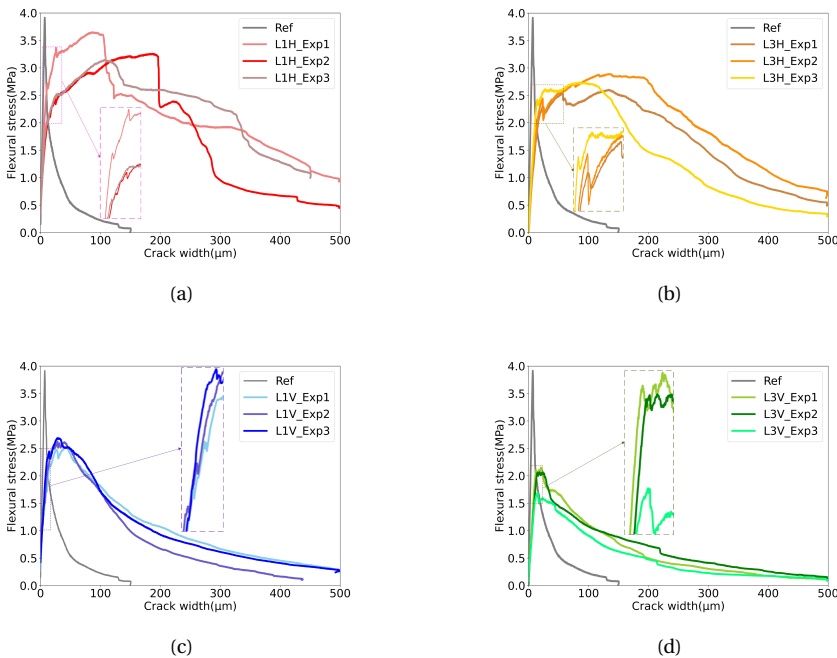


Figure 3.6: Flexural response comparison of specimens with different vascular networks (a) L1H; (b) L3H; (c) L1V; (d) L3V.

Flexural strengths of vascular self-healing cementitious materials are lower than

Table 3.4: Printing time and weight of the four kinds of vascular networks

No.	L1H	L1V	L3H	L3V
Printing time (h)	5	6.5	3	2
Weight (g)	14.75±0.05	13.5±0.2	314.7±0.1	13.5±0.1

that of the reference, showing that the embedded vascular networks reduce the flexural strength. For the specimens with the ABS vascular network, flexural strength of horizontally printed vascular self-healing cementitious materials is higher than that of vertically printed counterparts when the printing layer-height is equal. A possible reason is that the tensile strength of the interlayer between printing layers is poor [21]. When the loading direction is perpendicular to the printing direction of vascular networks, the maximum bearing load of the specimens is lower compared with the scenario when the loading direction and the printing direction are same. As to the influence of printing layer-height, flexural strength of the specimens with smaller printing layer-height (0.1mm) is higher than that of the larger ones (0.3mm), which agrees with what was expected. In other words, vascular networks with smaller printing layer-height have higher interlayer strength than the those with larger printing layer-height, which would contribute to higher flexural strength. The curves show different trends after reaching the maximum stress. When the printing direction is horizontal, the stresses remain high level (over 2.0MPa) till the crack width is over 300 μ m. L1H experiences a sudden drop from the second peak to 2.5MPa when crack width reaches 150 μ m, after which the stress stabilizes until dropping again when the width is over 300 μ m. However, the curve of L3H steadily drops after the second peak and the stress is larger than 2MPa when the crack width is smaller than 250 μ m. When the printing direction is vertical, the curves both show a steady drop after the second peak. The curve of L3V drops more quickly compared with L1V.

3.4. POTENTIAL INFLUENCING FACTORS

PRINTING parameters influence the fracture behavior of the specimens by the printing quality of the vascular networks. Therefore, the influence of printing parameters on the vascular network and the complete self-healing specimens is investigated in this section.

3.4.1. INFLUENCE OF THE MICROSTRUCTURE OF VASCULAR NETWORK

During the printing process, the printing time, and the weights of the four vascular networks (3 samples in each group) were measured. The results are given in Table 3.4.

From Table 3.4, it is noted that printing time of vascular with a smaller printing layer-height (0.1mm, L1H and L1V) is much longer than that of a larger printing layer height (0.3mm, L3H and L3V) because of a larger number of printing layers. The printing direction has a significant influence on the weight of the vascular network, while the influence of printing layer-height is negligible. To investigate the influence of printing parameters on the surface of the vascular, individual hollow ABS bars (D=5mm, d=3mm) printed using the four different sets of printing parameters were printed. CT

scanning was carried out to observe the microstructure of the vascular (Figure 3.7).

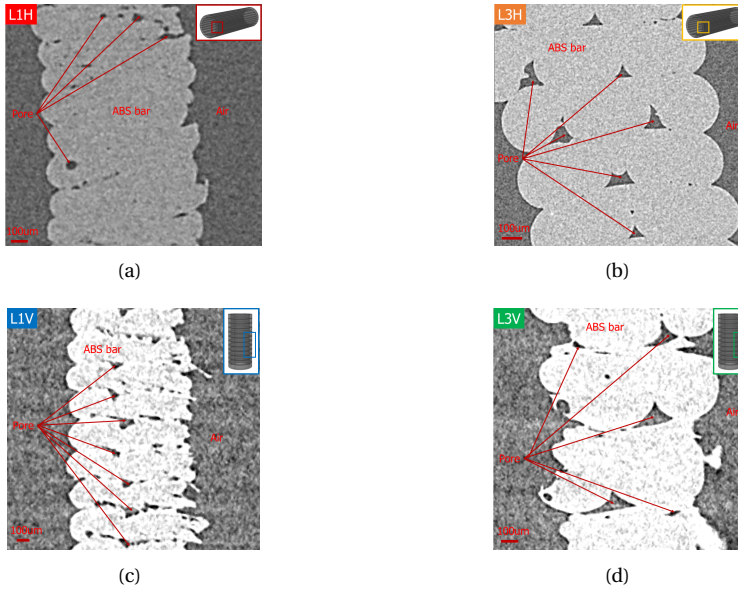


Figure 3.7: Printing quality of 3D-printed vascular (a) L1H; (b) L3H; (c) L1V; (d) L3V (the position of the scanned area in the vascular is indicated in the top right corner of each sub-figure).

Figure 3.7 reveals that the interlayer of the vascular printed with a smaller layer-height is much denser than the larger one when the printing direction is the same. The dense interlayer may contribute not only to higher mechanical strength but also prevent the cementitious matrix from entering the vascular network during casting and causing blockage. When the printing layer height is the same, there are more pores in vertically printed ABS bars. As a result, the flexural strength of the specimens embedded with vertically printed vascular is lower than the horizontally printed counterparts. More importantly, the mechanical interlocking between the cementitious matrix and vascular network are different due to the different roughness of the vascular. From the result of CT scanning, the surface of the vascular with larger printing layer-height is much rougher than that of the smaller one.

3.4.2. INFLUENCE OF THE MACROSTRUCTURE OF VASCULAR NETWORK

Except for the difference of mechanical interlocking, the overall printing quality of the vascular networks is significantly influenced by the printing direction. The printed vascular is shown in Figure 3.8.

Vertically printed vascular networks have better quality than the horizontally printed ones, as there are some pores in the joint regions for L1H and L3H. Based on the visible defects of the printing vascular networks, the printing quality of L1V is the best among the four kinds of vascular networks. When the printing direction is horizontal, the printing quality of L3H has much more defects than that of L1H. The defects in the

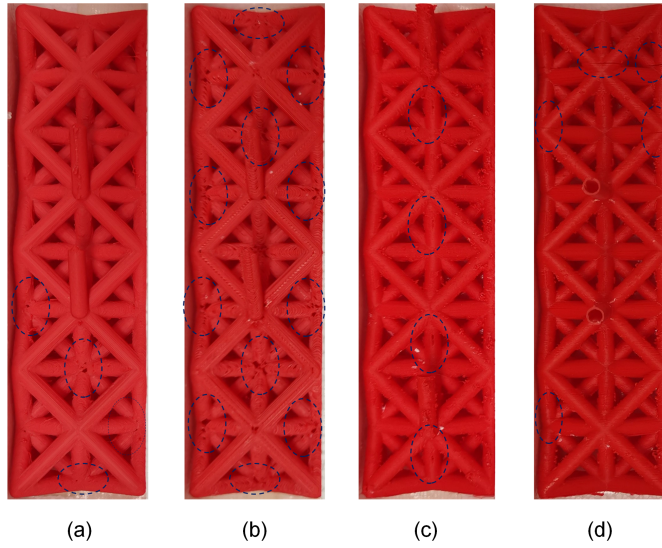


Figure 3.8: 3D-printed vascular networks, showing the influence of printing parameters on the printing quality of (large visible pores on the photographed surface are circled): (a) L1H (3 large pores); (b) L3H (12 large pores); (c) L1V (4 large pores); (d) L3V (5 large pores). Large pores are circled.

joint regions may cause leakage of cementitious slurry into the vascular system before the cementitious matrix is totally hardened. To verify this inference, CT scanning was carried out to observe the inside of the vascular self-healing cementitious materials. The resolution of CT scanning is $27.5\mu\text{m}$. If the slurry goes into the L1V vascular network, which has the best quality as described above, other vascular networks in self-healing concretes are likely to be partly filled with hardened matrix. The scanning results of L1V is shown in Figure 3.9. From Figure 3.9, it is obvious that parts of the vascular networks in all cases may be filled with the cementitious matrix.

3.5. FLEXURAL STRENGTH RECOVERY

3.5.1. EFFECT OF PRINTING PARAMETERS ON FLEXURAL STRENGTH RECOVERY

AFTER the specimens were injected with epoxy resin through the ABS vascular, 4-point bending tests were carried out again to investigate the mechanical recovery. The flexural strengths of the 4 vascular self-healing cementitious materials before and after the healing process are compared and the results are shown in Figure 3.10(a).

To better evaluate the healing capacity of the vascular self-healing cementitious materials, healing efficiency is employed as a metric. According to Hansen et al [16], healing efficiency of mechanical strength is defined with Equation 3.1.

$$\eta = \frac{p^{healed}}{p^{original}} \times 100\% \quad (3.1)$$

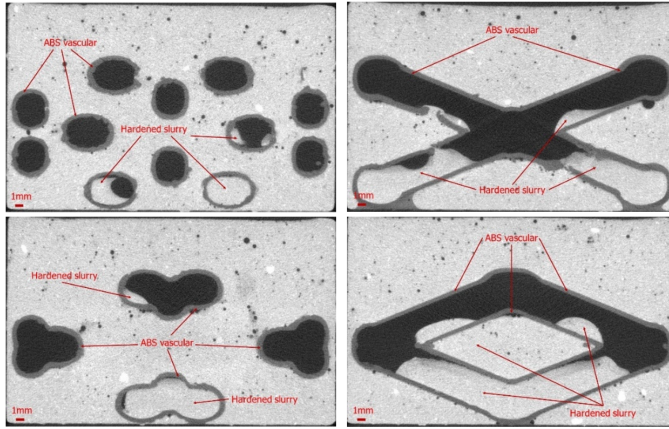


Figure 3.9: CT Scanning result of L1V.

where η is the healing efficiency; $p^{original}$ and p^{healed} are the strength of the virgin and healed specimens, respectively.

Based on Eq. 3.1, the healing efficiency of the vascular self-healing cementitious materials was calculated, and the result is shown in Figure 3.10(b).

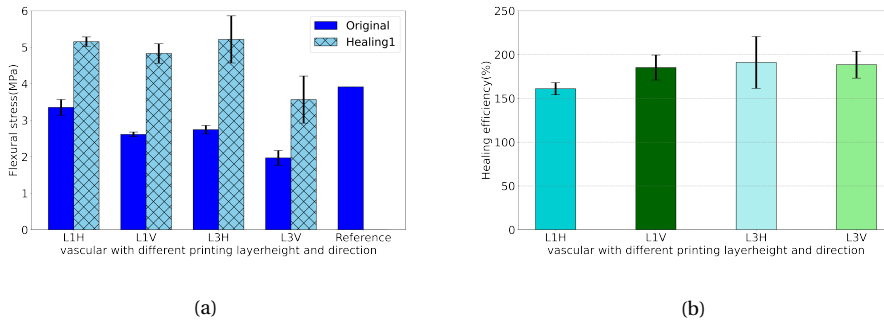


Figure 3.10: Healing efficiency of 3D-printed vascular with different printing parameters; (a) flexural strength comparison before and after healing process; (b) healing efficiency (3 samples in each group).

From Figure 3.10, it is noted that the healing efficiencies of the four ABS-printed vascular self-healing cementitious materials are all higher than 150%. In other words, the healing efficiency of vascular self-healing cementitious materials is remarkable when using epoxy resin as the healing agent. The average healing efficiency of L3H is the highest among the four scenarios, even though the variation is high. As to the influence of printing direction on strength regain, the flexural strength of the horizontally printed vascular specimens is higher than the vertically printed counterparts after the healing process. The horizontally printed vascular networks have more defects than the vertically printed ones. As a result, more slurry may enter the

vascular and fill part of the vascular network. During the healing process, more healing agent remained in the vascular due to the blockage of vascular and it contributes to a higher strength for horizontally printed vascular self-healing cementitious materials after the healing process. The typical mechanical responses of the four vascular self-healing cementitious materials loaded with a constant crack opening displacement speed before and after the healing process are shown in Figure 3.11.

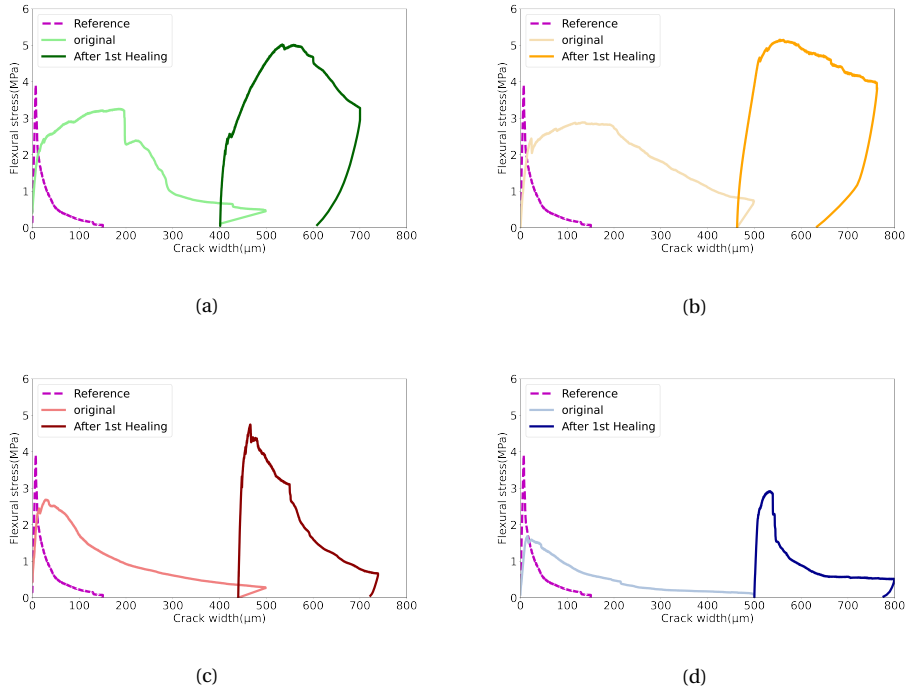


Figure 3.11: Flexural stress-crack width curve comparison after the first healing process (a) L1H; (b) L3H; (c) L1V; (d) L3V.

When the crack width of the healed specimen reaches $300\mu\text{m}$, the bearing stress of L1H and L3H are still over 3MPa while the bearing stress of L1V and L3V are less than 1MPa , which means that the ductility of horizontally printed vascular is much better than the vertically printed ones. Note that the healed fracture strength of L3V is much lower than the other 3 scenarios (even lower than the strength of the reference). Therefore, vascular network printed with the parameters of L3V has a significant adverse influence on the healing of the specimen. In addition, the areas below the curve for horizontally printed vascular self-healing cementitious materials are much larger than the vertically printed ones, which means that the specimens with horizontally printed vascular networks absorb more energy during deformation and fracture for the same crack width. For crack closure after one healing process, the cumulative crack width of horizontally printed vascular self-healing cementitious materials ($<650\mu\text{m}$) is much smaller than the vertically printed ones ($>700\mu\text{m}$).

Considering that the healing agent may leak out if the crack width is very large, the horizontally printed sample seems to have better healing efficiency if an additional round of healing is carried out. According to the experimental results, the crack occurring in the first round of 4-point bending test did not reopen upon reloading. Instead, a different crack developed after the healing process (Figure 3.12). Therefore, it can be inferred that the crack in the first 4-point bending test was completely healed during the healing process with epoxy resin as healing agent.

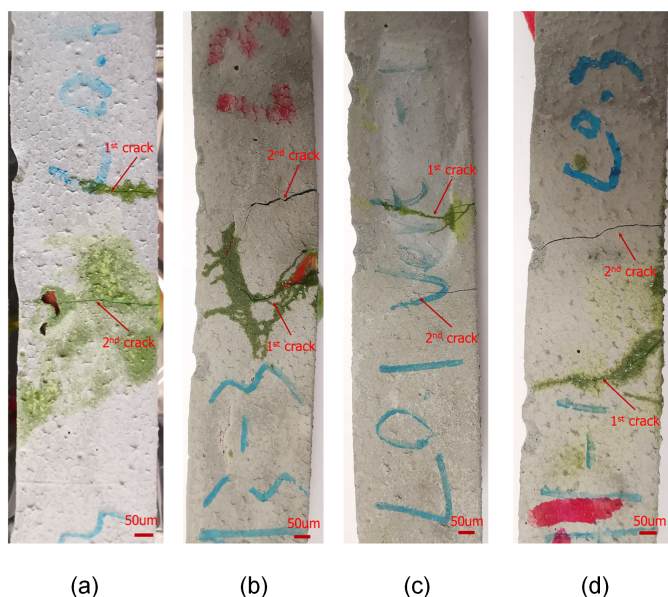


Figure 3.12: Crack morphology after the second 4-point bending test (a) L1H; (b) L3H; (c) L1V; (d) L3V (side view of the specimens).

The influence of printing layer height shows different trends when the printing direction is different. When the printing direction is horizontal, the flexural strength of vascular self-healing cementitious materials does not experience a dramatic change when the printing layer height increases from 0.1mm to 0.3mm. However, the area under the flexural stress-crack width curve of L3H is different from that of L1H, which means that L3H absorbs more energy than L1H during deformation and fracture after one healing process when the crack width reaches $300\mu\text{m}$ after the healing process. As for crack closure, unlike the trend after the first 4-point bending test, the crack width of L3H is smaller than that of L1H after the second 4-point bending test. Considering that the first crack is completely healed during the healing process, the actual crack widths of L1H and L3H after the second 4-point bending test are $150\mu\text{m}$ and $200\mu\text{m}$, respectively. When printing direction is vertical, the flexural strength of vascular self-healing concretes significantly decreases with the increase of printing layer height, even though the healed fracture stress of L1V and L3V are both higher than the original fracture stress. Compared with L1V, the stress of L3V sharply decreases after it reaches the maximum flexural strength, which means that the absorbed energy is much less

than L1V. As to the crack closure, there seems to be no obvious difference of the final crack width between L1V and L3V.

3.5.2. HEALING POTENTIAL OF THE 4 VASCULAR BASED SELF-HEALING CONCRETES

As mentioned above, the measurement of crack width becomes inaccurate when the deflection reaches $800\mu\text{m}$ after the first healing process. In order to investigate the healing potential of these ABS-printed vascular self-healing cementitious materials, 12 vascular self-healing concretes were cast and tested in another series of 4-point bending tests. These tests were carried out with a constant vertical displacement speed of 0.01mm/s . The flexural strengths of the specimens after 2 healing processes are compared and the results are shown in Figure 3.13.

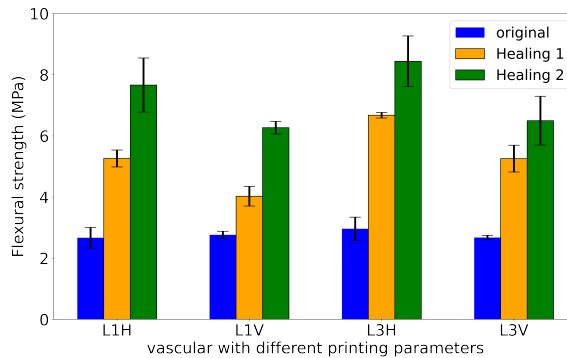


Figure 3.13: Flexural strength comparison of specimens (Controlled with constant vertical displacement) .

From Figure 3.13, it can be seen that the flexural strengths of horizontally printed vascular self-healing cementitious materials are higher than those of their vertically-printed counterparts. The influence of printing direction on the mechanical strength recovery remains obvious after the second healing process. In addition, it is worth mentioning that the average flexural strength (out of 3 samples) of L3H is the highest after the first/second healing process.

Whether the printing direction is horizontal or vertical, specimens with larger printing layer height (0.3mm, L3H and L3V) have higher flexural strength than those with smaller printing layer height (0.1mm, L1H and L1V) after injecting epoxy resin. However, the difference between them decreases after the second healing process. In other words, the influence of printing layer height diminishes when 2 healing processes are carried out because an increasing percentage of the vascular being filled with epoxy resin.

3.6. WATER TIGHTNESS RECOVERY

3.6.1. EFFECT OF PRINTING PARAMETERS ON WATER TIGHTNESS OF CRACKED SAMPLES

THE crack water permeability test was carried out on cracked specimens before the self-healing procedure to evaluate the influence of printing direction and printing layer-height on the initial permeability of the concretes. Three samples in each group were tested. The result is shown in Figure 3.14.

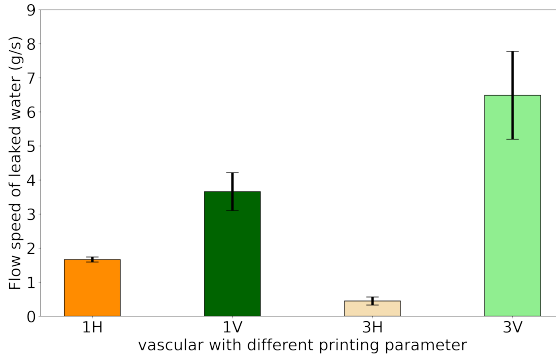


Figure 3.14: Flow speed of leaked water of specimens with different vascular networks.

As presented in Figure 3.14, specimens embedded with vertically printed ABS vascular have poorer water tightness than those with the horizontally printed ones. Considering that the permeability is proportional to the third power of the crack width, the final crack widths of 4 vascular self-healing cementitious materials are recorded during the 4-point bending test. The result is shown in Figure 3.15. Note that the final crack width of horizontally printed vascular is smaller than that of the vertically printed ones when printing layer height is same.

When analyzing the influence of printing layer height, the results of horizontally printed vascular and vertically printed vascular self-healing concrete show different trends. If considering only the influence of crack closure, vascular networks with larger printing layer height are expected to have higher permeability than that of vascular with smaller printing layer height. However, L3H has a lower permeability than L1H, whose final crack width ($418\mu\text{m}$) is smaller than L3H ($486\mu\text{m}$). A possible reason is that the printing quality of L3H is poorer than that of other vascular, especially in the joint areas. Consequently, some cementitious slurry may flow into the vascular during the casting process and block parts of the vascular network. This inference was verified by the printing quality assessment of 3D-printed vascular provided in Section 3.4.2.

3.6.2. EFFECT OF PRINTING PARAMETERS ON WATER TIGHTNESS RECOVERY

After healing the cracks with epoxy resin, permeability tests were carried out to evaluate the water tightness recovery. The recovery of water tightness is defined as Equation 3.2

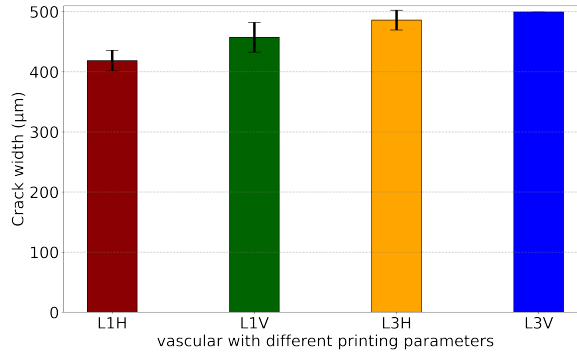


Figure 3.15: Final crack widths of specimens with different vascular networks.

([17]):

$$RWT = \frac{W_{n-h}(t) - W_h(t)}{W_h(t)} \times 100\% \quad (3.2)$$

where $W_{n-h}(t)$ and $W_h(t)$ are the average amount of water that has passed through the unhealed and healed cracks of the specimens per second (units in g/s), respectively. The amounts of leaked water through the healed cracks of all 4 types of vascular-self-healing cementitious materials are 0. In other words, the water tightness of all investigated vascular self-healing concretes is fully recovered (i.e., $RWT=100\%$). The possible reason is that the permeability setup used only has a water head of 0.5m and it is hard to measure the flow speed of water. Therefore, in this work, the printing direction and printing layer-height seem to have no obvious influence on the water tightness recovery when using epoxy resin as the healing agent. However, this needs to be further verified.

3.7. CONCLUSIONS

IN this chapter, the influence of printing parameters on the initial properties and the healing efficiency of vascular self-healing cementitious materials was investigated. Vascular networks with the (nominally) same geometry were printed with 2 different printing directions and 2 different printing layer heights. Four-point bending tests were performed to evaluate the influence on the initial flexural strength and strength recovery. In addition, the permeability of the 4 vascular self-healing cementitious materials before and after the healing process were compared. Based on the presented results, the following conclusions can be drawn:

- Compared with the reference mortar, the vascular self-healing cementitious composites have lower initial flexural strength. The specimens with horizontally printed vascular have higher flexural strength than the vertically printed counterpart. Vascular networks with smaller printing layer height have less

influence on the initial flexural strength of vascular-based self-healing concrete.

- The composites show good self-healing properties: when using epoxy resin as the healing agent, healing efficiencies in terms of strength regain for the 4 vascular self-healing cementitious materials are all over 150%, indicating that the flexural strength of the specimens after the healing process is much larger than their original flexural strength. The healing efficiency of L3H is the highest among the 4 vascular based self-healing concretes.
- When the specimens were loaded with a constant vertical displacement speed after 2 healing processes, horizontally printed vascular self-healing cementitious materials had higher flexural strength than the vertically printed counterparts after two healing processes. However, the influence of printing layer height decreases as the number of the healing actions increases due to the hardened healing agents in the vascular system.
- Similar to the fracture behaviour, the printing quality may also affect the water tightness: the horizontally printed vascular self-healing cementitious materials have lower initial permeability than that of the vertically printed ones. However, the influence of printing layer-height is different when the printing direction is different. Among the 4 specimens, L3H has the best water tightness, and a possible reason is that the poor printing quality of L3H vascular induces partial block of the vascular network.
- The water tightness recoveries of 4 vascular self-healing cementitious materials are 100%, which means that the printing direction and printing layer-height do not have obvious effect on the water tightness recovery when using epoxy resin as healing agent.

REFERENCES

- [1] Z. Wan, Y. Xu, Y. Zhang, S. He, and B. Šavija, *Mechanical properties and healing efficiency of 3d-printed abs vascular based self-healing cementitious composite: Experiments and modelling*, Engineering Fracture Mechanics **267**, 108471 (2022).
- [2] E. Tsangouri, C. Van Loo, Y. Shields, N. De Belie, K. Van Tittelboom, and D. G. Aggelis, *Reservoir-vascular tubes network for self-healing concrete: performance analysis by acoustic emission, digital image correlation and ultrasound velocity*, Applied Sciences **12**, 4821 (2022).
- [3] Y. Shields, N. De Belie, A. Jefferson, and K. Van Tittelboom, *A review of vascular networks for self-healing applications*, Smart Materials and Structures **30**, 063001 (2021).
- [4] Z. Li, L. R. de Souza, C. Litina, A. E. Markaki, and A. Al-Tabbaa, *A novel biomimetic design of a 3d vascular structure for self-healing in cementitious materials using murray's law*, Materials & Design **190**, 108572 (2020).
- [5] P. Minnebo, G. Thierens, G. De Valck, K. Van Tittelboom, N. De Belie, D. Van Hemelrijck, and E. Tsangouri, *A novel design of autonomously healed concrete: Towards a vascular healing network*, Materials **10**, 49 (2017).
- [6] Y. Shields, T. Van Mullem, N. De Belie, and K. Van Tittelboom, *An investigation of suitable healing agents for vascular-based self-healing in cementitious materials*, Sustainability **13**, 12948 (2021).
- [7] C. Abeykoon, P. Sri-Amphorn, and A. Fernando, *Optimization of fused deposition modeling parameters for improved pla and abs 3d printed structures*, International Journal of Lightweight Materials and Manufacture **3**, 284 (2020).
- [8] S. Dwiayati, A. Kholil, R. Riyadi, and S. Putra, *Influence of layer thickness and 3d printing direction on tensile properties of abs material*, in *Journal of Physics: Conference Series*, Vol. 1402 (IOP Publishing, 2019) p. 066014.
- [9] Y. Xu, H. Zhang, Y. Gan, and B. Šavija, *Cementitious composites reinforced with 3d printed functionally graded polymeric lattice structures: Experiments and modelling*, Additive Manufacturing **39**, 101887 (2021).
- [10] S. Selvamani, M. Samykano, S. Subramaniam, W. Ngui, K. Kadirgama, G. Kanagaraj, and M. Idris, *3d printing: Overview of abs evolvement*, in *AIP Conference Proceedings*, Vol. 2059 (AIP Publishing, 2019).
- [11] Z. H. Zhou, Z. Q. Li, D. Y. Xu, and J. H. Yu, *Influence of slag and fly ash on the self-healing ability of concrete*, Advanced materials research **306**, 1020 (2011).
- [12] P. Chindasiriphan, H. Yokota, and P. Pimpakan, *Effect of fly ash and superabsorbent polymer on concrete self-healing ability*, Construction and Building Materials **233**, 116975 (2020).

- [13] P. Termkhajornkit, T. Nawa, Y. Yamashiro, and T. Saito, *Self-healing ability of fly ash–cement systems*, *Cement and concrete composites* **31**, 195 (2009).
- [14] C. J. Hansen, S. R. White, N. R. Sottos, and J. A. Lewis, *Accelerated self-healing via ternary interpenetrating microvascular networks*, *Advanced Functional Materials* **21**, 4320 (2011).
- [15] C. Norris, I. Bond, and R. Trask, *The role of embedded bioinspired vasculature on damage formation in self-healing carbon fibre reinforced composites*, *Composites Part A: Applied Science and Manufacturing* **42**, 639 (2011).
- [16] C. J. Hansen, W. Wu, K. S. Toohey, N. R. Sottos, S. R. White, and J. A. Lewis, *Self-healing materials with interpenetrating microvascular networks*, *Advanced Materials* **21**, 4143 (2009).
- [17] E. Tziviloglou, V. Wiktor, H. Jonkers, and E. Schlangen, *Bacteria-based self-healing concrete to increase liquid tightness of cracks*, *Construction and Building Materials* **122**, 118 (2016).
- [18] E. Tziviloglou, Z. Pan, H. M. Jonkers, and E. Schlangen, *Bio-based self-healing mortar: An experimental and numerical study*, *Journal of Advanced Concrete Technology* **15**, 536 (2017).
- [19] E. Gruyaert, B. Debbaut, D. Snoeck, P. Díaz, A. Arizo, E. Tziviloglou, E. Schlangen, and N. De Belie, *Self-healing mortar with ph-sensitive superabsorbent polymers: testing of the sealing efficiency by water flow tests*, *Smart Materials and Structures* **25**, 084007 (2016).
- [20] Y. Chen, O. Çopuroğlu, C. R. Rodriguez, F. F. de Mendonca Filho, and E. Schlangen, *Characterization of air-void systems in 3d printed cementitious materials using optical image scanning and x-ray computed tomography*, *Materials Characterization* **173**, 110948 (2021).
- [21] Y. Xu, H. Zhang, B. Šavija, S. C. Figueiredo, and E. Schlangen, *Deformation and fracture of 3d printed disordered lattice materials: Experiments and modeling*, *Materials & Design* **162**, 143 (2019).

4

SELF-HEALING CEMENTITIOUS COMPOSITES WITH A HOLLOW VASCULAR NETWORK CREATED USING 3D-PRINTED SACRIFICIAL TEMPLATES

The existence of a vascular tube wall may impede with the healing efficiency if it does not rupture timely to release the healing agent. To overcome this, dissolvable Polyvinyl Alcohol (PVA) filament was adopted to fabricate the vascular networks. Different printing directions were expected to affect the dissolvability of printed structures and were therefore fabricated and tested. Different shapes (i.e., 2D and 3D) of vascular networks were printed and embedded in the cementitious mortar. Four-point bending tests and permeability tests were performed to investigate the healing efficiency. Multiple healing cycles were applied in the cracked specimens. The results show that the vertically printed PVA tubes with wax coating dissolve well. As expected, the existence of vascular networks decreases the initial flexural strength of the specimens. In terms of healing efficiency, excellent mechanical regain and recovery of water tightness were achieved when using epoxy resin as the healing agent. The mechanical recovery after the first healing process is higher than the following healing process. The water permeability of the cracked samples keeps decreasing with the increasing number of healing cycles. Specimens embedded with 3D vascular networks have higher healing potential than those utilizing 2D vascular networks.

Parts of this chapter were published in Engineering Structures (2023) [1].

4.1. INTRODUCTION

FOR self-healing cementitious materials embedded with vascular networks, the vascular tubes need remain intact during a long period to ensure their functionality for self-healing. For example, the high alkaline environment can decrease the integrity of vascular materials such as borosilicate glass [2] or PLA [3]. To overcome this problem, hollow channels can be reserved inside the host matrix to serve as paths for transporting healing agents [4–6]. For creating three-dimensional vascular networks in self-healing cementitious materials with additive manufacturing, sacrificial printing materials such as fugitive ink (60wt% petroleum jelly and 40wt% microcrystalline wax) [7] and water-soluble Polyvinyl Alcohol (PVA) [8] have been used. It has been shown that the dissolution of the extruded PVA embedded in the cementitious matrix is not affected by the high alkalinity, and the main functional groups of extruded PVA remain unchanged with the un-extruded PVA [8]. However, the possible reaction of PVA with the cementitious matrix (especially with $Ca(OH)_2$) may induce cracks and generate insoluble products. When it comes to printed PVA, a possible influence of its printing direction on the dissolution when embedded in a cementitious matrix has not been previously studied. Furthermore, self-healing cementitious materials with different shapes of hollow channels as vascular networks has rarely been studied.

In this chapter, we investigate the self-healing cementitious composite embedded with a sacrificial 3D-printed vascular network. The dissolution of 3D-printed PVA hollow tubes under different configurations, i.e., printing directions (horizontal/vertical), tube wall thickness/radius ratios, and coating conditions (with/without wax coating) is studied first. The influence of vascular shape (i.e., 2D and 3D) on the mechanical properties under 4-point bending is investigated. Subsequently, epoxy resin is injected as the healing agent to seal the cracks for multiple times. The healing efficiency in terms of flexural strength and recovery of water tightness of the vascular self-healing mortar is discussed.

4.2. EXPERIMENTS

4.2.1. FABRICATION AND PRE-PROCESSING OF PVA VASCULAR TUBES

ONE-DIMENSIONAL hollow tubes were fabricated first to study the influence of fabrication configuration on the dissolution of PVA tubes embedded in cementitious mortar. The designed tubes were sliced with Cura (Ultimaker, Utrecht, Netherlands) and then were printed with a commercial 3D printer Ultimaker 2+. The printing parameters are shown in Table 4.1.

Fused deposition modelling (FDM) builds objects layer-by-layer and thereby inducing variations in material properties and the presence of imperfections (such as voids and pores), depending on the different printing direction [9]. These imperfections may influence the dissolution of PVA. Except for printing direction (vertical/horizontal), thickness/radius and wax coating (as explained below) are also taken into consideration. Instead of solid tubes, hollow tubes were printed to minimize the outward expansion of the tubes caused by water uptake during the dissolution of PVA. The printing quality of such hollow tubes tends to be poor if the tube thickness is small, since the diameter of the heated nozzle used herein is 0.25mm. On the other hand,

Table 4.1: Printing time and weight of the four kinds of vascular networks.

Printing parameters	Value
Nozzle temperature (PVA, °)	225
Nozzle temperature (PLA, °)	210
Nozzle size (mm)	0.25
Bed plate temperature (°)	60
Fan speed (%)	100
Printing speed (mm/s)	30
Layer height (mm)	0.06

thick tubes are difficult to dissolve due to their volume expansion. In addition, the volume expansion of the PVA tube wall may introduce cracks to the cementitious matrix, especially in the early age [8]. To determine the optimal thickness of the PVA tubes, PVA tubes with different thicknesses/radius (t/R) were fabricated and investigated.

It is known that PVA polymers react with $Ca(OH)_2$ and calcite ($CaCO_3$) in the cementitious matrix, and the reactant is not dissolvable. Therefore, this reaction has an adverse influence on the dissolution of PVA tubes. To isolate the PVA tubes from the cementitious matrix, the hollow PVA tubes were coated with wax. Wax coating was performed by spraying with paraffin wax with a low melting temperature. The dissolution of the coated PVA tubes and uncoated PVA tubes are compared. The samples embedded with PVA tubes were cured in water under room temperature for 7 days before being observed with X-ray computed tomography (CT scanning). The schematic of samples fabricated with different configurations is shown in Figure 4.1. In the figure, t and R refer to the thickness and radius of the tubes, respectively.

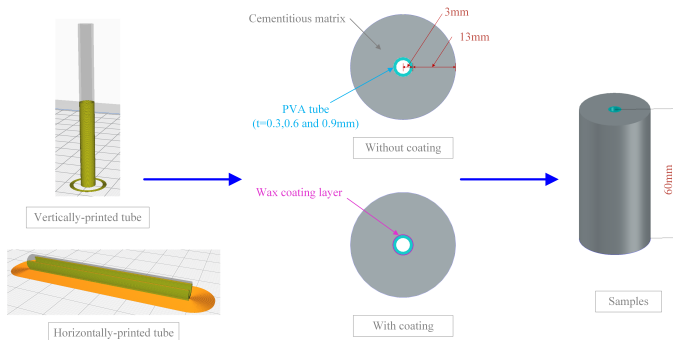


Figure 4.1: Schematic of samples with PVA tubes fabricated with different configurations.

After understanding the effect of printing direction, vascular tube thickness and coating condition, two-dimensional (2D) and three-dimensional (3D) vascular networks were fabricated. The diameters of the vascular network were designed based on Murray's law (Equation 2.2) to minimise turbulent flow at junctions [10]. To avoid possible blockage caused by volume expansion during the dissolution of PVA tubes, the amount of PVA in the vascular network was minimized. In particular, the vascular

Table 4.2: The properties of PLA and PVA (provided by Ultimaker).

Property	PLA	PVA
Chemical formula	$(C_3H_4O_2)_x$	$(C_2H_4O)_x$
Glass transition ($^{\circ}$)	60	58.4
Melting temperature ($^{\circ}$)	145-160	175.4
Specific gravity (g/cm^3)	1.24	1.23

network in the possible crack region (under 4-point bending load) was printed with PVA filament, with the remainder printed with PLA filament. The properties of PLA and PVA are shown in Table 4.2.

The 3D-printed vascular network was assembled and then embedded in the cementitious matrix. The schematics of the 3D-printed vascular networks in the cementitious matrix are shown in Figure 4.2. For comparison, the parent tubes (first generation) of the vascular network (PLA part) are kept in the middle of height in the samples for 2D and 3D vascular network.

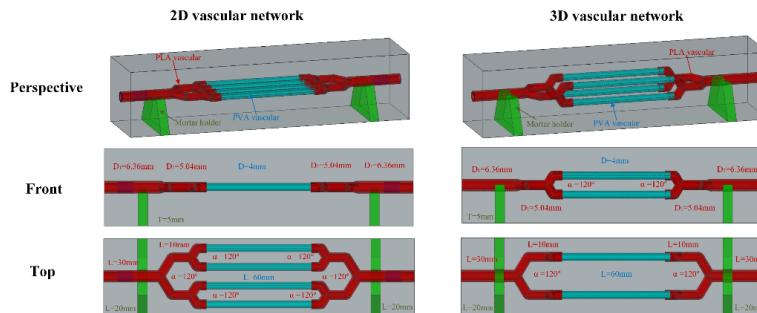


Figure 4.2: Schematic of samples embedded with 3D-printed PVA vascular network.

4.2.2. CASTING

After the vascular networks were assembled and coated with wax, they were positioned in the foam moulds using precast cement paste holders (see Figure 4.2). Fibre reinforced mortar was used with 0.1 wt% ultra-high molecular weight polyethylene fibre (UHMWPE) to prevent the samples from suddenly breaking into two halves during the 4-point bending test. The technical data sheet of UHMWPE and the mix proportion of the cementitious mortar are listed in Table 4.3 and 4.4, respectively. Except for the vascular self-healing specimens, plain cementitious mortar (i.e., without vascular network) was tested as a reference. Three samples were tested in each group.

The casting process, was as follows [11]: cement and sand were dry-mixed for 4min in a Hobart planetary mixer. Water was then added to the dry components and mixed for 2min. Afterwards, fibres were added and mixed for another 2min. The mixed materials were poured in Styrofoam moulds with a dimension of $160mm \times 40mm \times 40mm$ ($L \times W \times H$) and vibrated for 30s. The specimens were covered with a plastic film to prevent water loss. The specimens were kept in room temperature

Table 4.3: The technical data sheet of ultra-high molecular weight polyethylene fibre (UHMWPE).

Property	Value
Density (g/cm^3)	0.97-0.98
Length (mm)	6
Filament cross section	Nearly round
Filament diameter (μm)	19-43
Melting range ($^{\circ}C$)	144-452
Breaking Strength (GPa)	3.0
Breaking Modulus (GPa)	110
Elongation (%)	2-3

Table 4.4: Mix design of the cementitious matrix (kg/m^3).

CEM III/B 42.5 N	Sand (0.125-0.25mm)	water	UHMWPE
1085.0	497.3	434.0	0.9

for 24h and then demolded.

4.2.3. REMOVING PVA VASCULAR AND CURING

Considering that the dissolution of one-dimensional PVA tube is relatively easy since the dissolved PVA could easily flow out of the tube, these samples were directly submerged in water with room temperature for 7 days to remove the PVA tube walls after demolding. The curing water was daily changed considering a possible reaction between the dissolved PVA in water and the cementitious matrix.

For the samples embedded with the 2D/3D PVA vascular network, additional measures were taken to help remove the PVA tubes before the curing process. Considering that the elevated temperature accelerates dissolution of PVA tubes, these samples were submerged in warm water with a temperature of $70^{\circ}C$ in the first 2h after demolding (from 24-26h). During the same time period, pressurized air was injected into the vascular networks to flush the dissolved PVA out of the network every 30min (i.e., 4 times in 2h) to avoid the blockage in the joints of the vascular networks. Afterwards, the samples were cured in water with room temperature for 27 days before the first round of the 4-point bending test. Curing water was changed every week.

4.2.4. HEALING PROCESS

The samples were subjected to 4-point bending to measure the initial flexural strength as well as to induce cracks for the following healing process. A two-component epoxy resin was used as the healing agent because of its low viscosity and high regain in strength [12]. Epoxy resin (Conpox Resin BY 158, Condor Kemi A/S) and hardener (Conpox Hardener BY 2996, Condor Kemi A/S) were first weighted and mixed with a mass ratio of 3:1 and stirred for 1min. Then, epoxy resin was manually injected into the vascular networks from one end through a syringe while blocking the other end with a clip. In total, 10ml of epoxy resin was used to ensure sufficient healing agent to reach the crack through the vascular system. The injection speed was controlled as 10ml/min. The clip at the outlet of the vasculature was removed after 5min, and then pressurized air was injected after

30min to remove the excess epoxy resin from the hollow channels. The schematics of the manual healing process is shown in Figure 4.3. The treated samples were kept at room temperature for 24h until the injected epoxy resin was fully hardened. The healed samples were tested under 4-point bending (three samples in each group).

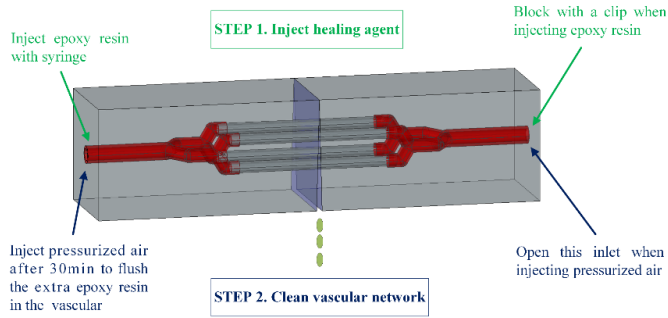


Figure 4.3: Schematic of manual healing process (3D vascular network).

4.2.5. CHARACTERIZATION

Similar to what has been done in chapter 3, the specimens were characterized with 4-point bending test, water permeability test and CT scanning. The hardened samples embedded with vascular networks were scanned to observe the dissolution of PVA tubes in the vascular network and the resolution is $27.5\mu\text{m}$. The schematics of 4-point bending test and permeability test are shown in Figure 4.4(a) and 4.4(b) respectively. More details could be found in chapter 3.

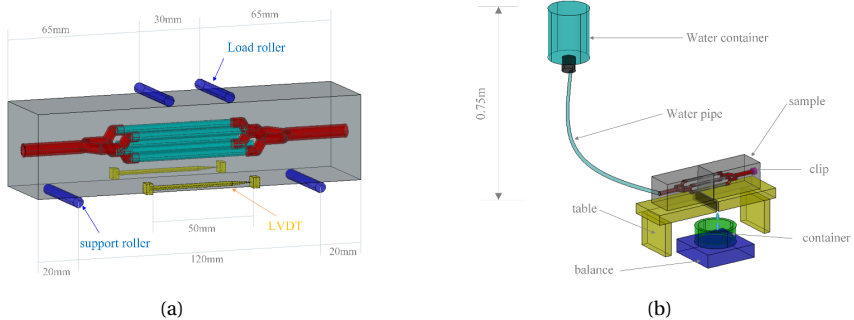


Figure 4.4: Schematics of characterization setups (a) 4-point bending test; (b) Permeability test.

4.3. INFLUENCE OF PRINTING CONFIGURATION ON DISSOLUTION OF PVA

4.3.1. DISSOLUTION OF ONE-DIMENSIONAL PVA TUBES

PROPERTIES of the 3D-printed structures are significantly influenced by the printing parameters such as printing direction and printing layer-height [13]. Herein, the influence of printing direction on the dissolution of PVA vascular system is first studied using one-dimensional hollow bars. Besides, thickness and wax coating are also considered. The surface of the demolded samples is directly observed and the result is shown in Table 4.5.

From the table, it is noted that the horizontally printed tubes without wax coating did not dissolve. Therefore, the inner parts of those samples were not investigated with a micro-CT scanner. The tomographs of tested samples are shown in Figure 4.5. The black part in the figures represents the air, manifesting that nothing exists there.

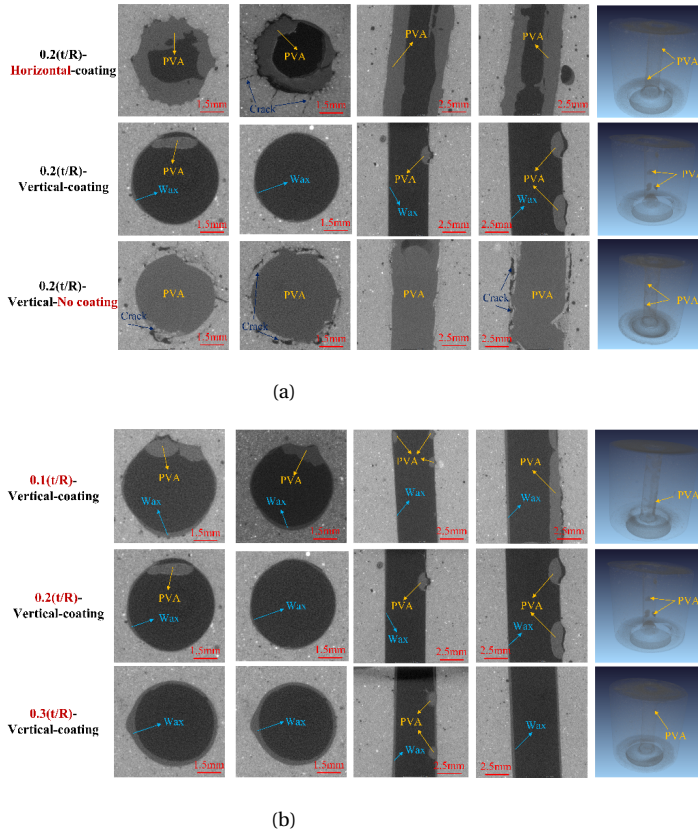
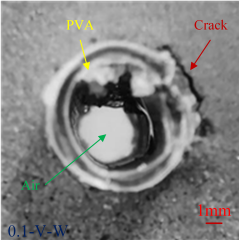
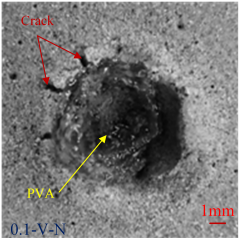
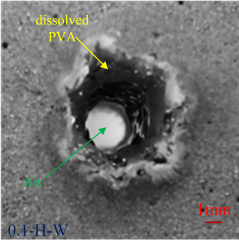
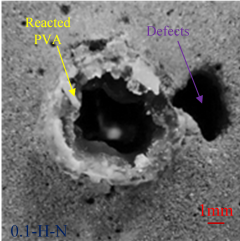
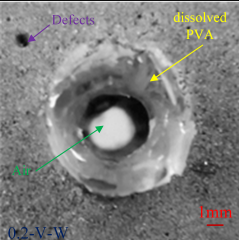
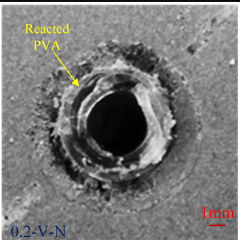
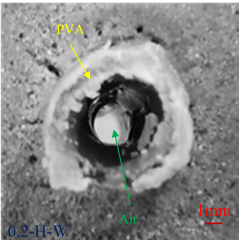
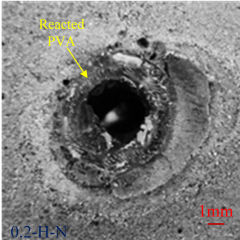
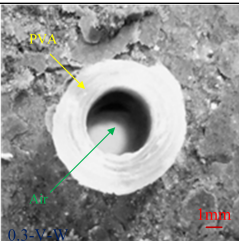
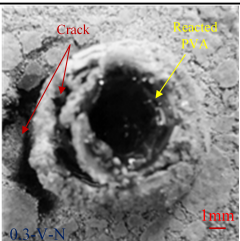
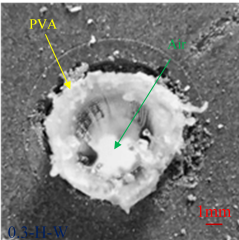
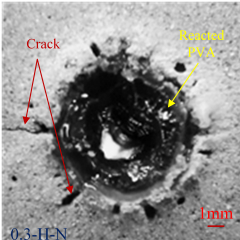


Figure 4.5: Test result from CT scanning, (a) Tubes with different printing direction and wax coating (thickness/radius of 0.2); (b) Tube with different thickness/radius (vertically printed, wax coating).

As shown in Fig.4.5(a), the dissolution of PVA tubes is significantly influenced by

Table 4.5: Photos of the demolded samples (printing configurations: thickness/Radius, printing direction).

Printing configurations	Wax coating	No wax coating
0.1-Vertical		
		
0.2-Vertical		
		
0.3-Vertical		
		

printing direction and coating condition. When the thickness/radius is 0.2 and the tubes are wax coated, the vertically printed tube dissolved better than the horizontally printed one. For the horizontally printed PVA tube, the tube wall has not fully dissolved, and several cracks presented in the cementitious matrix around the tubes. A possible reason is the poor printing quality of the horizontally printed tube, resulting in more defects. Consequently, a part of the PVA tube was not insulated from the cementitious matrix even though the PVA tube was coated with paraffin wax. The rough interface between the PVA tube and the matrix (0.2-horizontal-wax coating) shows that the PVA tube reacts with the cementitious matrix, causing it to expand. As a result, cracks occur in the matrix surrounding the tube. In vertically printed tubes (0.2-vertical-wax coating), PVA dissolved almost completely, and no cracks occur around the tube. The interface between the cementitious matrix and the tube is smoother compared to that of the horizontally printed one. Therefore, the PVA tube should be printed in a vertical direction to compose the vascular networks.

Except for printing direction, wax coating also significantly influences the dissolution of PVA tubes (Fig.4.5(a)). Compared with the coated PVA tubes (0.2-vertical-coating), the uncoated tube (0.2-vertical-No coating) did not dissolve at all. The reaction between the cementitious matrix and the PVA causes problems for both the cementitious matrix and PVA tube. On the one hand, the reacted mortar around the tubes delaminates and thereby causing cracks in the matrix, while the reacted PVA fails to dissolve. On the other hand, the inner PVA wall expands inwards and fills the inner space due to the water uptake. This makes it impossible for water to enter the tube which then stops dissolving.

The influence of tube wall thickness/radius ratio (0.1-0.3) is also investigated. As shown in Fig.4.5(b), the dissolution of PVA tube with thickness/radius ratio of 0.1 is the poorest, although a part of the tube has been removed. Compared with the thicker tube, less perimeter lines are used for the thin wall (thickness=0.2mm, $t/R=0.1$) and thereby causing unstable printing, which increases the possibility of more defects. As a result, wax coating was not uniform and the reaction between PVA and the cementitious mortar occurred locally in the areas of defects. For thickness/radius ratios of 0.2 and 0.3, the PVA tubes are totally dissolved. Considering that the thicker PVA tube not only consumes more printing material, but also takes more time to dissolve, the thickness/radius ratio of 0.2 was selected for further investigation in this study.

Therefore, the PVA parts of the vascular networks were printed in the vertical direction, which showed better printing quality compared with the horizontally printed counterparts. Furthermore, wax coating proved to be necessary for the dissolution of PVA tubes by isolating the PVA tubes from the cementitious matrix and thereby preventing the occurrence of their expansive reaction. Based on the thickness/radius ratio, the thickness of PVA tube was set as 0.4mm (radius is 2mm) for creating the middle part of the vascular networks. The outer part of the vascular network was created with PLA. To decrease the cantilever during the printing process, the PLA parts of the 2D/3D vascular networks are printed in horizontal and vertical respectively. Those two parts (i.e., PVA tubes and PLA connectors) were assembled and sealed with liquid rubber (Bison rubber repair) to avoid leakage. Wax coating for the PVA tubes was applied after assembling. The 3D-printed vascular networks are shown in Figure 4.6(a).

The actual thickness of the 3D-printed PVA tubes is measured by microscope (Keyence VHX Digital Microscope) and shown in Figure 4.6(b). From the result, it could be concluded that there are inaccuracies during the printing process.

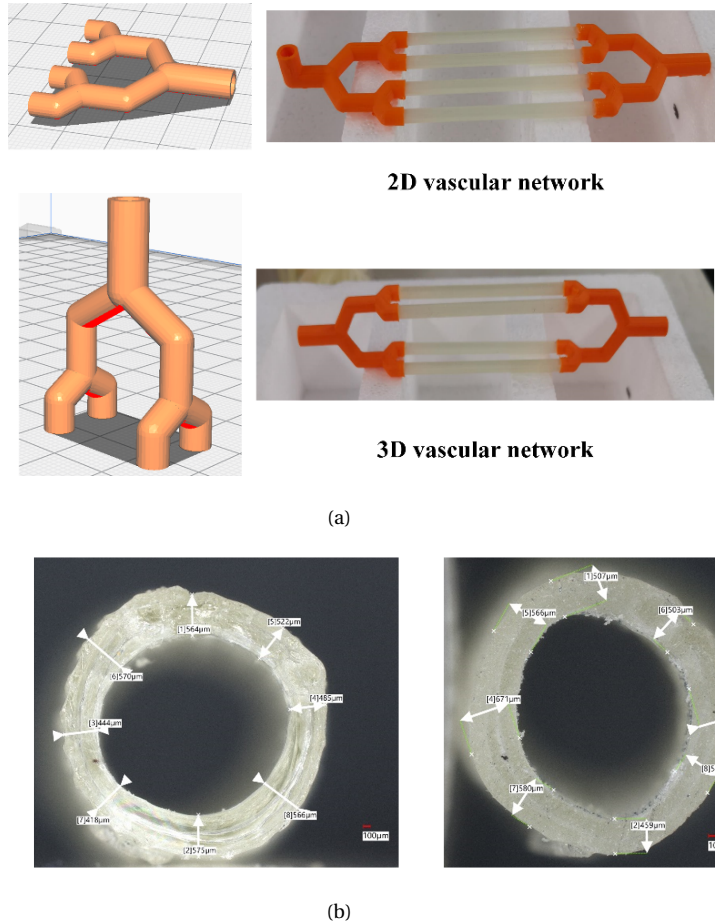
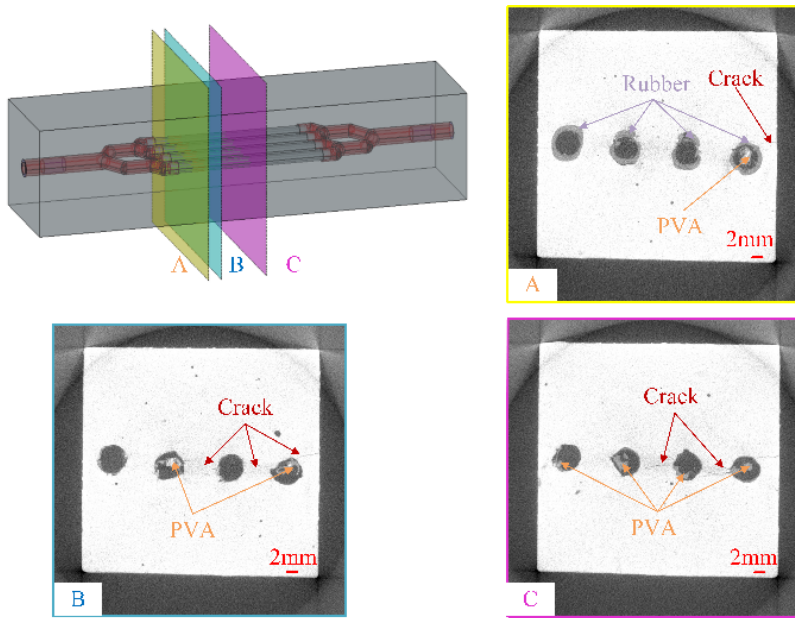


Figure 4.6: Fabrication of vascular network (a) schematic of the 2D-/3D- vasculature (orange-PLA, white-PVA); (b) Actual thickness of PVA tube.

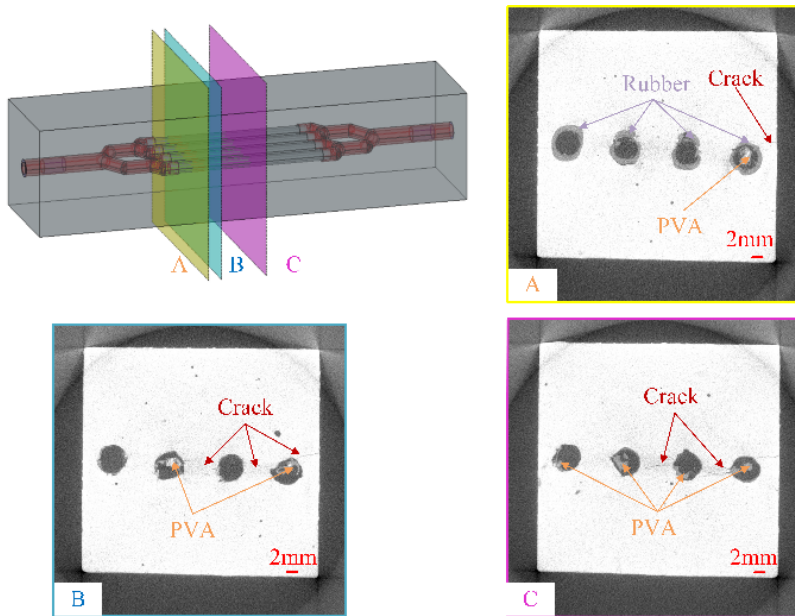
4.3.2. DISSOLUTION OF THE 3D-PRINTED VASCULAR NETWORK

Based on the results in section 4.3.1, vascular networks were created and embedded in the cementitious mortar. To observe the dissolution of the PVA part of the network, CT scanning was performed before the mechanical tests. The results are shown in Figure 4.7.

From Fig.4.7, it is obvious that most of the PVA tubes in the 2D and 3D vascular system have dissolved. Furthermore, there were no issues in connecting the PLA and PVA tubes using liquid rubber, which was confirmed because the cementitious slurry



(a)



(b)

Figure 4.7: CT scans of vascular based self-healing concrete. (a) PVA tube in the 2D vascular network; (b) PVA tube in the 3D vascular network.

did not enter the vascular network through these connection points. However, compared with the one-dimensional tubes studied in Section 4.3.1, the overall dissolution of PVA was less efficient. The PVA tubes are in the middle part of the vascular network, making it difficult for the dissolved PVA to flow out of the vascular networks. As a result, some PVA remained in hollow vascular network for both geometries (i.e., 2D and 3D).

The PVA tubes in the 2D vascular network had poorer dissolution compared with those in the 3D vascular network. As shown in the Fig. 4.7(a), part of the PVA tubes fails to dissolve in the middle part of 2D vascular network, while no PVA remained in the middle of the 3D vascular network. Furthermore, cracks between the hollow channels occurred in the 2D vascular network, and to a lesser extent in 3D vascular network. Clearly, the dissolution of the PVA tubes in the 3D vascular network is better than that of the 2D vascular network.

Although the PVA tube wall in the vascular network was well removed, some problems did occur during casting and pre-processing. Compared with the designed vascular network orientation, the position of the vascular networks is slightly changed for both 2D and 3D vascular network, which may be an issue when accurate orientation of vascular network is required. Besides, some cracks occur around the channels for both 2D and 3D vascular network. These could have been caused to an extent by the pressurized air used to remove the dissolved PVA. It is noteworthy that the wax/PVA dissolvable network system is scalable. For large-scale structural elements, the fabrication of the network system (larger diameters) and wax coating (larger thickness) are relatively easy. In addition, the feasibility of injecting warm water in large vascular system has already been proven [14]. However, the pressure would have to be increased for the large-scale structures.

4.4. FLEXURAL STRENGTH

4.4.1. INITIAL FLEXURAL RESPONSE OF VASCULAR SELF-HEALING CEMENTITIOUS MATERIALS

DURING the 4-point bending tests, cracks occurred in the middle span between the two load rollers in all specimens. In other words, cracks did not cross the PLA connectors of the vascular network. The stress-crack width (CMOD) curves of the cementitious mortars embedded with 2D and 3D vascular networks are shown in Figure 4.8.

From Fig. 4.8, it is found that the flexural strength of the specimens with hollow vascular networks is lower than the references, proving that the existence of vascular network adversely affects the flexural strength, as expected [15]. Note that, although the small amount fibres (0.1% by volume) give the specimens some residual load-bearing capacity, a single crack occurred in all samples. The vascular self-healing mortar have lower residual load-bearing capacity than the reference specimens.

As to the influence of vasculature shape, there is no significant difference between samples with 2D and 3D hollow vascular networks: the mean flexural strength of 2D vascular self-healing cementitious mortar was slightly higher but showed less standard deviation compared to the 3D counterpart. For both 2D and 3D vascular self-healing

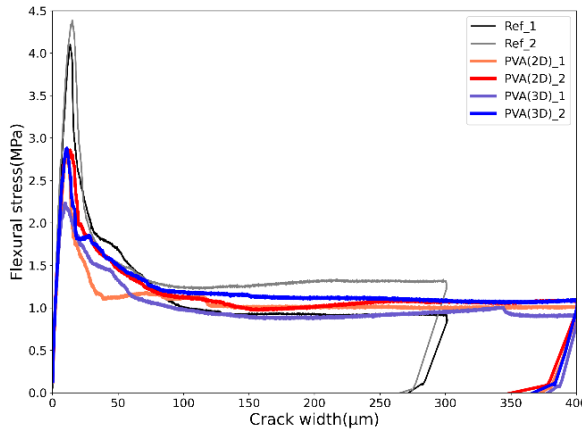


Figure 4.8: Flexural response of specimens embedded with 2D/3D vascular networks.

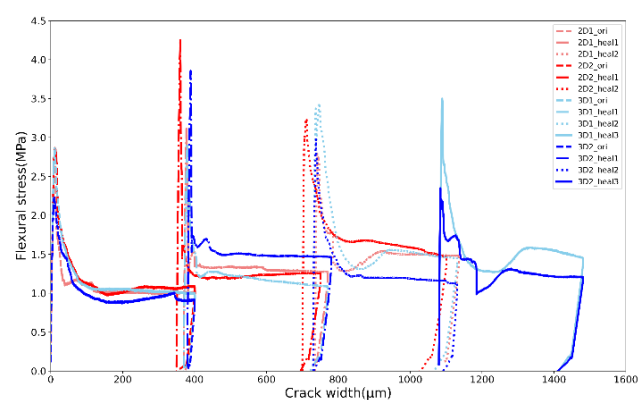
specimens, some crack closure occurs, and the final crack widths of samples are less than $400\mu\text{m}$.

4.4.2. STRENGTH RECOVERY OF THE VASCULAR SELF-HEALING CEMENTITIOUS COMPOSITE

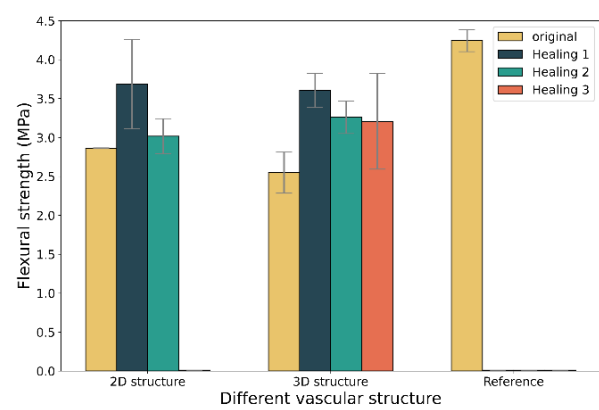
To seal the cracks, epoxy resin was injected through the vascular networks. The healed samples were tested again after the epoxy resin had hardened. Multiple healing events were carried out until it became difficult to manually inject the epoxy resin to the vascular networks. Based on the test, we performed two healing cycles for 2D vascular self-healing cementitious materials, while three cycles for the samples embedded with the 3D vascular network. The flexural responses of samples embedded with 2D/3D vascular networks are shown in Figure 4.9.

As shown in Fig. 4.9, flexural strength can be regained upon healing in vascular self-healing cementitious mortar. Compared with reference specimens, the specimens with vascular networks have higher flexural strength after the first healing process, manifested with healing efficiencies (defined by Equation 2.4) higher than 100%. In addition, after healing, the residual load-bearing capacity of the specimens increased. Note that a new crack is formed after the second round of 4-point bending test. Considering that the epoxy is stronger than the matrix, the increased residual load-bearing capacity is inferred to be caused by the residual epoxy resin in the vascular network. Additionally, this may be also caused by the enhanced fibre/matrix interface due to the increase of the interfacial frictional bond strength of FRCC after autogenous healing [16].

After the second healing process, the flexural strength was still higher than the initial one, although it was lower than that after the first healing. This was observed for both 2D and 3D vascular self-healing composite mortar. A possible reason is that the



(a)



(b)

Figure 4.9: Comparison of the healed specimens embedded with 2D-/3D- vascular network regarding (a) flexural response; (b) flexural strength.

epoxy resin injected in the first healing process hardened in the vascular system, even though pressurized air was used to remove the excess epoxy resin from the vascular network. As a result, less epoxy could flow into the crack during the second healing process. Compared with the 2D vascular specimens, the flexural strength of the 3D vascular specimens after the second healing cycle is higher. Furthermore, the samples embedded with 3D vascular network were healed for 3 rounds. Therefore, the samples embedded with 3D vascular network have higher healing potential. In terms of residual load-bearing capacity after cracking, 2D vascular specimens perform better than 3D vascular specimens after the second healing cycle.

4.5. WATER TIGHTNESS

4.5.1. RECOVERY OF WATER TIGHTNESS

PERMEABILITY tests were carried out on the cracked specimens before and after the healing procedure. The water permeability was measured after each 4-point bending test and healing process. The recovery of water tightness is defined as Equation 3.2 in chapter 3.

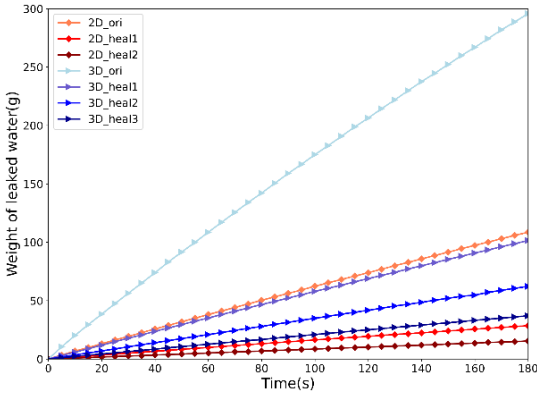
The amounts of water leaked through the healed cracks of the 2D/3D vascular self-healing cementitious specimens are 0 after each healing process. Therefore, the water tightness of the investigated specimens has fully recovered (i.e., RWT=100%). One possible reason for the high recovery of water tightness is that the fibres in the cracks increase the roughness of crack, promoting the injected epoxy resin to remain in the cracks instead of flowing out the cracks. It should be noted, however, that the permeability test setup used only with a water head of 0.75m, which does not allow measuring low values of flow speed.

4.5.2. CRACK WATER PERMEABILITY AFTER HEALING

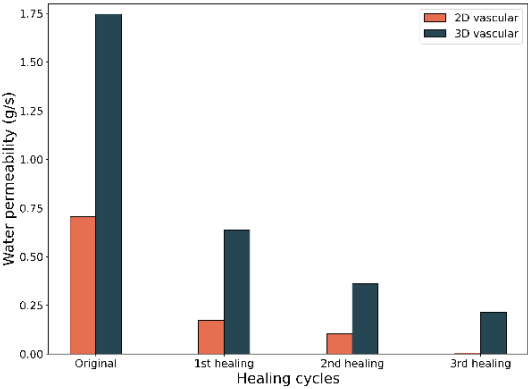
Except for recovery of water tightness, water permeability of the cracked samples was also investigated since several healing processes were carried out. The water permeability of the cracked specimens could help judge whether it is possible to carry out another round of healing process. The mean water permeability of the specimens embedded with 2D/3D vascular networks are shown in Figure 4.10.

The mean water permeability of the original samples embedded with 3D vascular network is much larger than that of the 2D vascular ones (Fig. 4.10). A possible reason is that the two channels of the 3D vascular network are closer to the bottom of the sample. With the increased number of healing cycles, the water permeability of the cracked samples decreased for both 2D and 3D vascular self-healing cementitious mortar. This is caused by the increasing amount of residual hardened epoxy resin in the vascular network.

Compared with the samples with 3D vascular networks, water permeability of the 2D vascular self-healing cementitious materials is lower after each 4-point bending test. However, this may decrease the possibility of further healing because the low water permeability will also prevent the healing agent (i.e., epoxy resin) from entering the crack. This could explain why the flexural strength of 3D vascular self-healing cementitious materials is higher than that of the 2D vascular samples after the second



(a)



(b)

Figure 4.10: Water permeability of the cracked specimens after 4-point bending tests; (a) The change of leaked water with time; (b) Water tightness comparison in different healing cycles.

healing process. As a result, 3D vascular network enables performing more healing processes than the 2D vascular network for the vascular self-healing concretes.

4.6. CONCLUSIONS

HEREIN, a self-healing cementitious material was developed using 3D printed sacrificial vascular networks. Thereby, the influence of printing direction, thickness/radius and wax coating on the dissolution of one-dimensional PVA tubes was first investigated. Under the optimal printing configuration, two kinds of vascular networks (i.e., 2D/3D) with PVA tubes in the middle span were fabricated and embedded in the cementitious mortar. Four-point bending tests were carried out to evaluate the flexural strength as well as the mechanical recovery after healing. Furthermore, crack water tightness test of the 2D and 3D vascular self-healing cementitious mortar was performed to investigate the water tightness of samples before and after healing. Based on the obtained results, the following conclusions can be drawn:

- The reaction between PVA and cementitious matrix prevents the PVA tubes from dissolving, making coating of the tubes necessary (e.g., with wax, as done herein). The vertically printed PVA tubes dissolve better than the horizontally printed ones. The smaller circumference of thin tube results in unstable printing, which also affects the dissolution of PVA. The dissolution of PVA in the 2D/3D vascular networks is excellent, as shown by X-ray tomography.
- The existence of vascular network adversely influences the initial flexural strength. The mechanical recovery after each healing process is over 100% compared with the original specimens. The flexural strength after the first healing process is higher than after the second healing process. This is inferred to be caused by the extra hardened epoxy resin in the vascular system.
- Except for the improvement of flexural strength, the residual flexural stress of the healed samples is higher than the original specimens. A possible reason is that the interface between fibres in the crack and the cementitious matrix is strengthened by the injected epoxy resin.
- The water tightness of the cracked 3D vascular specimens is much better than of the 2D counterpart after the first 4-point bending test. However, the recovery of water tightness of the 2D and 3D vascular self-healing cementitious materials are both 100% when performing crack water tightness test with a water head of 0.75m. Further, the water permeability of the cracked samples sees an increase when more healing processes are performed. However, the low water permeability causes problems for the following healing process. Therefore, the cementitious mortar embedded with 3D vascular network has higher healing potential than the one with 2D vascular network.

REFERENCES

- [1] Z. Wan, Y. Zhang, Y. Xu, and B. Šavija, *Self-healing cementitious composites with a hollow vascular network created using 3d-printed sacrificial templates*, *Engineering Structures* **289**, 116282 (2023).
- [2] K. Van Tittelboom and N. De Belie, *Self-healing in cementitious materials—a review*, *Materials* **6**, 2182 (2013).
- [3] Y. Shields, N. M. Alderete, P. Van den Heede, Y. Villagran Zaccardi, P. Trtik, N. De Belie, and K. Van Tittelboom, *Influence of 3d printed vascular networks in self-healing cementitious materials on water absorption studied via neutron imaging*, in *76th RILEM Annual Week and International Conference on Regeneration and Conservation of Structures (ICRCS2022)* (2022).
- [4] S. Pareek and A. Oohira, *A fundamental study on regain of flexural strength of mortars by using a self-repair network system*, in *Proceedings of the 3rd International Conference on Self Healing Materials, Bath, UK*, Vol. 2729 (2011).
- [5] S. Sangadji and E. Schlangen, *Self healing of concrete structures-novel approach using porous network concrete*, *Journal of Advanced Concrete Technology* **10**, 185 (2012).
- [6] R. E. Davies, A. Jefferson, R. Lark, and D. Gardner, *A novel 2d vascular network in cementitious materials*, (2015).
- [7] K. S. Toohey, N. R. Sottos, J. A. Lewis, J. S. Moore, and S. R. White, *Self-healing materials with microvascular networks*, *Nature materials* **6**, 581 (2007).
- [8] Z. Li, L. R. d. Souza, C. Litina, A. E. Markaki, and A. Al-Tabbaa, *Feasibility of using 3d printed polyvinyl alcohol (pva) for creating self-healing vascular tunnels in cement system*, *Materials* **12**, 3872 (2019).
- [9] S. Dwiwati, A. Kholil, R. Riyadi, and S. Putra, *Influence of layer thickness and 3d printing direction on tensile properties of abs material*, in *Journal of Physics: Conference Series*, Vol. 1402 (IOP Publishing, 2019) p. 066014.
- [10] C. D. Murray, *The physiological principle of minimum work applied to the angle of branching of arteries*, *The Journal of general physiology* **9**, 835 (1926).
- [11] Y. Xu, E. Schlangen, M. Luković, and B. Šavija, *Tunable mechanical behavior of auxetic cementitious cellular composites (cccs): Experiments and simulations*, *Construction and Building Materials* **266**, 121388 (2021).
- [12] Y. Shields, T. Van Mullem, N. De Belie, and K. Van Tittelboom, *An investigation of suitable healing agents for vascular-based self-healing in cementitious materials*, *Sustainability* **13**, 12948 (2021).
- [13] Y. Xu, H. Zhang, B. Šavija, S. C. Figueiredo, and E. Schlangen, *Deformation and fracture of 3d printed disordered lattice materials: Experiments and modeling*, *Materials & Design* **162**, 143 (2019).

- [14] R. Davies, T. Jefferson, and D. Gardner, *Development and testing of vascular networks for self-healing cementitious materials*, Journal of Materials in Civil Engineering **33**, 04021164 (2021).
- [15] Z. Li, L. R. de Souza, C. Litina, A. E. Markaki, and A. Al-Tabbaa, *A novel biomimetic design of a 3d vascular structure for self-healing in cementitious materials using murray's law*, Materials & Design **190**, 108572 (2020).
- [16] J. Qiu, S. He, and E.-H. Yang, *Autogenous healing and its enhancement of interface between micro polymeric fiber and hydraulic cement matrix*, Cement and Concrete Research **124**, 105830 (2019).

5

NUMERICAL SIMULATION OF SELF-HEALING CEMENTITIOUS MATERIALS EMBEDDED WITH VASCULAR NETWORKS

Mechanical properties of vascular self-healing cementitious materials are significantly affected by the vascular configuration. In this chapter, self-healing cementitious materials with vascular networks (or hollow channels) are numerically investigated using concrete damage plasticity model (CDPM) in Abaqus software. The flexural response of 3D-printed ABS vascular self-healing cementitious materials (experimentally tested in chapter 3) was first simulated with 3D models. Afterwards, numerical simulation was performed to model the self-healing cementitious materials with hollow channels. Except for 3D model, 2D model with pores in the middle span as vascular system was used to improve the sensitivity of mechanical response to the change of vascular configurations, and the fracture behavior of different structures is discussed. The results show that the proposed numerical approach can provide an accurate simulation on the fracture behavior of cementitious composites with 3D-printed ABS vascular networks. After evaluating the computational time of the discussed models and the sensitivity of target property to the change of structures, 2D model with pores in the middle span was found to be the most suitable numerical model to generate a dataset for the optimization of vascular configuration using machine learning.

5.1. INTRODUCTION

MECHANICAL properties of vascular self-healing cementitious materials are significantly affected by the vascular configuration [2, 3]. However, due to the relatively simple design of vasculature in self-healing cementitious materials used in the past, most previous investigations focused on the fast transportation of healing agents and high healing effectiveness, rather than looking into the overall mechanical properties [4–6].

The recent development of additive manufacturing enables the fabrication of complicated vascular networks for self-healing cementitious materials. Although 3D-printed plastic vascular networks could act as the reinforcement [7], most vascular networks compromise the initial mechanical properties of the specimens (as shown in chapter 3). When creating hollow channels using dissolvable printing filaments (as shown in chapter 4), the vascular configuration further decreases the mechanical properties compared with the vascular networks printed with Acrylonitrile Butadiene Styrene (ABS) or Polylactic Acid (PLA) filaments [8]. To mitigate the adverse influence of vascular network while maintaining good healing capabilities, the vascular system in self-healing cementitious materials needs to be carefully designed.

The influence of vascular configuration on the properties of vascular self-healing cementitious materials has mainly been experimentally investigated [7]. However, it can be considered impossible to optimize vascular configuration using experiments due to the large design space. Numerical modelling can be useful in this respect. However, most numerical studies of vascular self-healing cementitious materials focused on the transport of healing agents [4, 9]. The mechanical response of self-healing cementitious materials embedded with vascular networks with different geometries has not been extensively studied using numerical models. Furthermore, optimization of the vascular configuration using tools such as machine learning (ML) has not been attempted to date.

In this chapter, the mechanical response of self-healing cementitious materials with 3D-printed vascular network is simulated. Concrete damage plasticity model (CDPM) is first introduced (section 5.2). Afterwards, 3D models were employed to investigate the fracture behavior of self-healing cementitious materials embedded with ABS vascular networks (section 5.3). Then, 2D and 3D models were adopted to simulate the fiber reinforced mortar with hollow channels (or pores) as vascular system for self-healing (section 5.4). Last, the feasibility of vascular configuration optimization with ML using the simulated results as the dataset is discussed (section 5.5).

5.2. CONCRETE DAMAGED PLASTICITY MODEL

THE commercial simulation software Abaqus was employed to simulate the 4-point bending test on the pristine specimens from chapter 3. The software uses concrete damaged plasticity model (CDPM), which is commonly used to study the nonlinear response of cementitious materials and is capable of capturing the main features of the response of concrete [10–12]. Tension stiffening and compression hardening are defined in Figure 5.1. The stress-strain relations under uniaxial tension and compression loading are shown in Equation 5.1 and 5.2, respectively.

$$\sigma_t = (1 - d_t)E_0(\varepsilon_t - \tilde{\varepsilon}_t^{pl}) \quad (5.1)$$

$$\sigma_c = (1 - d_c)E_0(\varepsilon_c - \tilde{\varepsilon}_c^{pl}) \quad (5.2)$$

where σ_t and σ_c are the tensile stress and compressive stress, respectively; d_t and d_c are tensile damage variable and compressive damage variable ranging from 0 (undamaged) to 1 (total loss of strength); E_0 is the initial (undamaged) elastic stiffness of the material; represents the load recovery index; ε_t and ε_c are the total strains; $\tilde{\varepsilon}_c^{pl}$ and $\tilde{\varepsilon}_t^{pl}$ are the equivalent plastic strains.

In this study, stiffness degradation is not considered and the damage variables are set to 0. Therefore, the equivalent plastic strains are equal to crack strains. As shown in Figure 5.1, the crack strains ($\tilde{\varepsilon}_t^{ck}$ and $\tilde{\varepsilon}_c^{ck}$) are defined as the total strain minus the elastic strain corresponding to the undamaged materials (Equations 5.3 and 5.4).

$$\tilde{\varepsilon}_t^{ck} = \varepsilon_t - \varepsilon_{0t}^{el} \quad or \quad \tilde{\varepsilon}_c^{ck} = \varepsilon_c - \varepsilon_{0c}^{el} \quad (5.3)$$

$$\varepsilon_t^{el} = \frac{\sigma_t}{E_0} \quad or \quad \varepsilon_c^{el} = \frac{\sigma_c}{E_0} \quad (5.4)$$

5.3. SIMULATION OF SELF-HEALING CONCRETE EMBEDDED WITH ABS VASCULAR NETWORKS

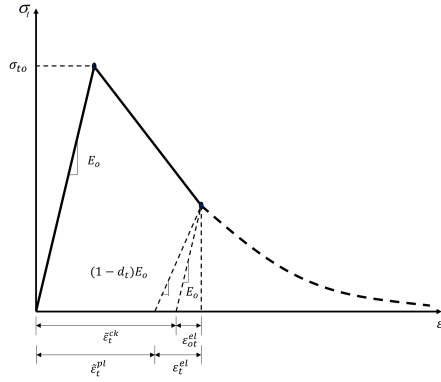
COMPARED with experiments, numerical simulation can be faster and cheaper. Herein, the simulation results are analyzed and compared with the experimental results from chapter 3. If the agreement is good, numerical simulations instead of experiments can be used to generate training data for optimizing the vascular geometry with machine learning (ML).

5.3.1. CALIBRATION FOR THE CEMENTITIOUS MATRIX

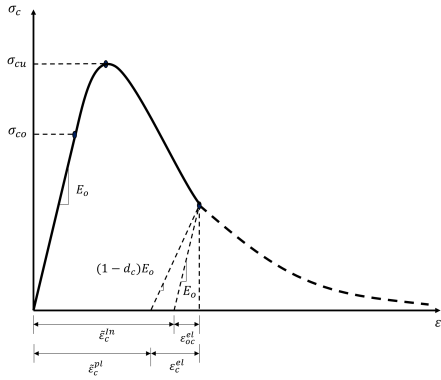
Before the numerical simulation, calibration is first performed to determine the inputs for models. The input parameters of CDPM are taken from [13] (Table 5.1), in which an identical cementitious matrix was used.

Table 5.1: Input parameters for cementitious mortar in the CDPM model.

(a) Compressive parameters		(b) Tensile parameters	
Yield stress (MPa)	Inelastic strain (%)	Yield stress (MPa)	Inelastic strain (%)
32	0	5.8	0
37	0.149	0.1	0.05
3	0.18		
1	0.2		



(a)



(b)

Figure 5.1: Constitutive law of CDPM in (a) Tension; (b) Compression.

5.3.2. CALIBRATION FOR ABS VASCULAR NETWORK

It is noted that 3D-printed ABS structure shows anisotropic fracture behaviors [14]. Therefore, ABS bars with different printing parameters were fabricated and tested to provide data for model calibration. The thickness of hollow vascular networks is 0.5mm. The ABS bar for calibration should keep the same, otherwise the nominal bending strength is different [15]. However, it is hard to print a solid bar with a dimension of 0.5mm. The section of ABS bar is fabricated as small as possible to minimize the size effect caused by 3D printing. Compared to a horizontally printed ABS bar, the vertically printed ABS bars with same section have lower printing quality due to the shorter time interval for cooling. Using a trial-and-error approach, the section of horizontally- and vertically- printed ABS bars are chosen as 2mm×1mm and 4mm×4mm, respectively. The dimension of ABS bars for calibration is listed in Table 5.2. Uniaxial tension tests were carried out with a speed of 0.001 mm/s by a Micro Tension-Compression Testing device (Figure 5.2) and three ABS bars of each group were tested.

Table 5.2: Dimension of the ABS bars tested for calibration (printing parameters refer to Table 3.2).

Printing parameters	L1H	L1V	L3H	L3V
Section (mm ²)	2x1	4x4	2x1	4x4
Length (mm)	40			

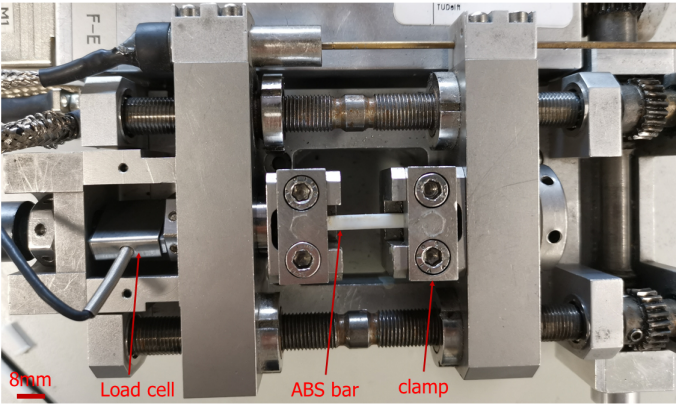


Figure 5.2: Micro Tension-Compression Testing device during testing of 3D printed ABS bars.

Since (3D printed) ABS structure is brittle, the brittle cracking model in Abaqus is employed to define the mechanical response of ABS vascular network during the 4-point bending test. The brittle cracking model is used with the linear elastic material model, which defines the behavior before cracking. The post failure stress-strain curve is shown in Figure 5.3. σ_t^I is the remaining direct stress after cracking and e_n^{ck} is the direct cracking strain [16].

Considering that the 3D-printed ABS bars were very small, the measured displacements were much higher than the real value due to the deformation of the loading and transmission for the Micro Tension-Compression Testing device [17]. The input parameters for the 4 kinds of ABS bars are shown in Table 5.3.

5.3.3. INTERACTION BETWEEN VASCULAR NETWORK AND THE CEMENTITIOUS MATRIX

The 6 displacements of the load rollers in the bottom (support) are fixed. The load rollers in the top are loaded downward to 2mm, while the other five displacements are fixed. The 4 load rollers contact with the samples with the contact type of surface-to-surface contact (Explicit), where normal behavior is defined as “hard” contact and tangential behavior is defined as penalty friction with a coefficient of 0.05. The connection between the vascular network and the cementitious matrix is considered as a tie constraint to reduce the computing time.

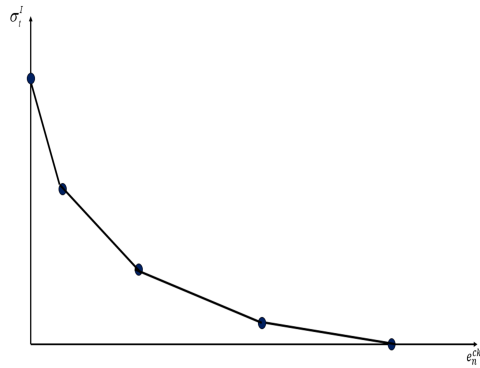


Figure 5.3: Post failure stress-strain curve of ABS (details depend on the printing parameters, see Table 5.3).

Table 5.3: Input parameters for ABS vascular networks.

(a) L1H		(b) L3H	
Direct stress after cracking	Direct cracking strain (%)	Direct stress after cracking	Direct cracking strain (%)
36.17	0	36.00	0
31.00	0.12	30.05	0.11
12.01	0.16	24.00	0.13
0.05	0.29	0.05	0.20
(c) L1V		(d) L3V	
Direct stress after cracking	Direct cracking strain (%)	Direct stress after cracking	Direct cracking strain (%)
19.50	0	13.51	0
16.16	0.025	0.68	0.02
0.11	0.034	0.05	0.05
0.05	0.075		

5.3.4. THE SIMULATION RESULTS OF CEMENTITIOUS MATERIALS WITH ABS VASCULAR NETWORKS

Considering the structure is symmetric in the longitudinal direction, half of the structure is simulated to reduce the computational time. A schematic of the numerical model is shown in Figure 5.4.

The results of simulated 4-point bending tests are compared with the experimental results in Figure 5.5.

In general, the simulated curves show a good agreement with the experimental counterparts. The simulated flexural strength of the reference specimen is slightly overestimated compared with the experiments. Furthermore, the simulated result shows a more brittle behavior. In the simulation, the loading speed is controlled by vertical displacement instead of a constant crack mouth opening speed, as done in the experiments. For all the 4 different designs, after cracking, a hardening branch can be observed in both the experiments and the simulations. The extent of this hardening branch is dependent on the printing parameters, although nominally all vascular designs are identical.

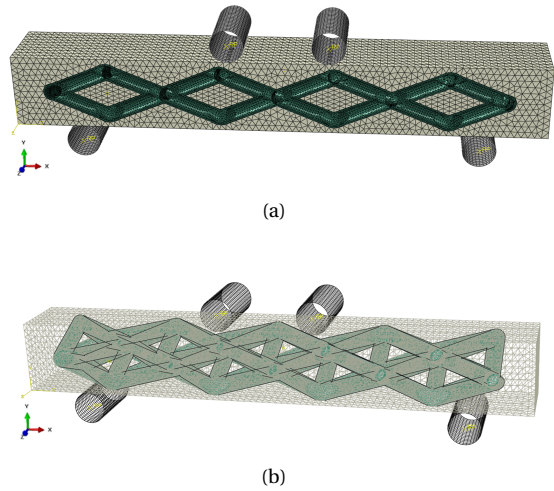


Figure 5.4: Schematics of numerical model in (a) main view; and (b) perspective view (green: vascular network; gray: the cementitious matrix; black: load cell).

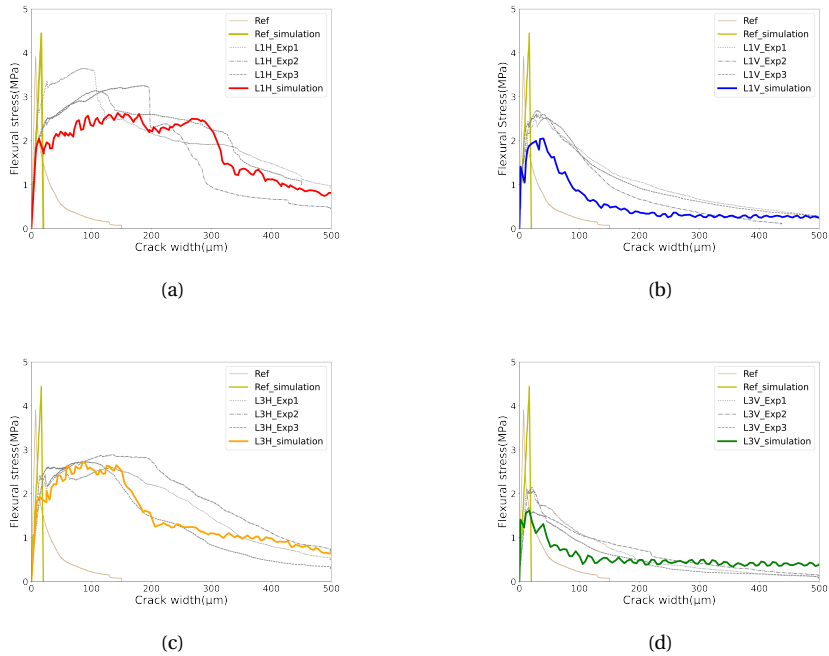


Figure 5.5: Simulated results of specimens with different vascular networks (a) L1H; (b) L1V; (c) L3H; (d) L3V.

Although the embedded vascular networks do reduce the flexural strength, the ductility of ABS-printed vascular self-healing concretes is higher compared with the reference since the ABS vasculature acts as a reinforcement for the specimens. The area below the experimental curves is defined as the toughness of the cementitious composite. For the vascular self-healing cementitious materials, toughness is calculated by the area till the crack width is $500\mu\text{m}$, while the reference is calculated till the crack width is $150\mu\text{m}$ where the stress is less than 0.1MPa . Compared with the vascular self-healing concrete, the reference is brittle and it breaks into two halves when crack width reaches $150\mu\text{m}$. The result is shown in Figure 5.6.

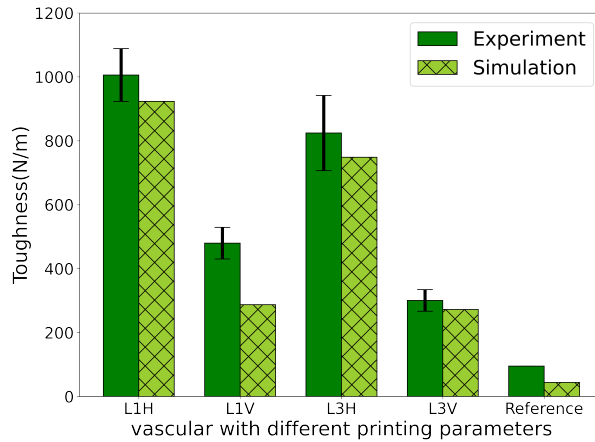


Figure 5.6: Toughness comparison of specimens with different vascular networks.

As shown in Figure 5.6, the toughness calculated by numerical simulation is very close to the experimental results, except for L1V. Compared with the reference, the vascular self-healing concretes absorb more energy during deformation and fracture. The specimens embedded with horizontally printed vascular networks have much higher toughness than the vertically printed counterparts. It is inferred that the horizontally printed vascular network has better ductility, resulting in stronger reinforcement effect compared with the other three groups. The crack morphology obtained by the numerical simulations and the experiments is also compared for the L1V specimen (Figure 5.7). As shown in Figure 5.7, the crack morphologies from numerical simulation and experiment are very similar. In both numerical simulations and experiments, there is only one crack, and the crack develops upwards with a small angle. A possible reason is that the ABS-printed vascular network is not strong enough to act as the reinforcement that could create multiple cracks. A similar trend has been reported in [13], where solid octet lattice structures are embedded in the cementitious matrix.

Therefore, the numerical approach can provide an accurate simulation of the fracture behavior of cementitious composites with 3D printed ABS vascular networks.

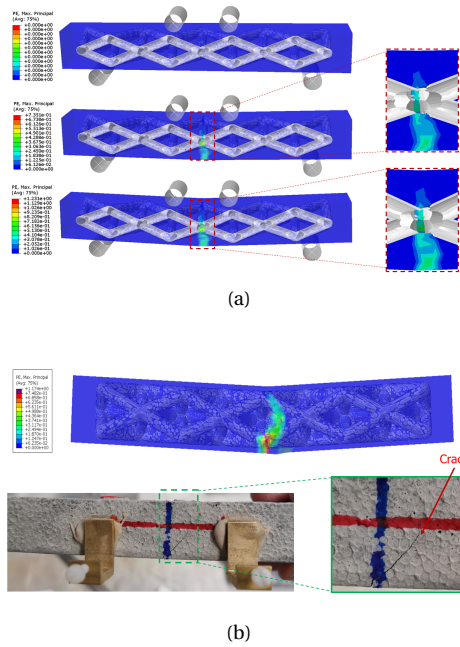


Figure 5.7: (a) Inner crack evolution from simulation; (b) crack morphology from simulation and experiment.

Even with vascular networks prepared with various printing parameters, the simulated stress-crack width by the Concrete Damaged Plasticity model (CDPM) in Abaqus is in excellent agreement with the experimental results, in terms of crack width and flexural strength under four-point bending.

However, these simulations of specimens with a 3D vascular network are time-consuming, which makes it difficult to generate a large amount of data needed for data-driven design process of the 3D vascular systems. The computational effort is in part caused by the three-dimensional nature of the simulation, and in part by the fact that fracture of the ABS vascular network is explicitly simulated.

5.4. SIMULATION OF SELF-HEALING CONCRETE WITH HOLLOW CHANNELS

EXCEPT for thermoplastic filaments such as ABS or PLA, vascular networks could also be printed with PVA filament, leaving hollow channels to act as the path for transporting healing agents (Chapter 4). In this scenario, the computational time for numerical simulation could be shorter than the one embedded with ABS vasculature due to the absence of vascular tube walls. In addition, simplifying the numerical model (e.g., from 3D to 2D) or the vascular shape could further reduce the computational cost.

5.4.1. 3D MODEL FOR SELF-HEALING CEMENTITIOUS MATERIALS WITH HOLLOW CHANNELS

The geometry of the vascular network with hollow channels (see chapter 4) could be further simplified to reduce computational costs. Although the vascular network is designed as hierarchical (i.e., using Murray's law) to better transport the healing agent, the crack and PVA tubes of the vascular network mainly occur in the middle span under 4-point bending. A 3D model with four hollow tubes could be created to simulate the flexural response of specimens. As shown in Figure 5.8(a), the 4 hollow channels are selected from the 49 positions. An example of the model is shown in Figure 5.8(b). The simulated stress-displacement curves of 5,000 structures with different vascular configurations are shown in Figure 5.8(c).

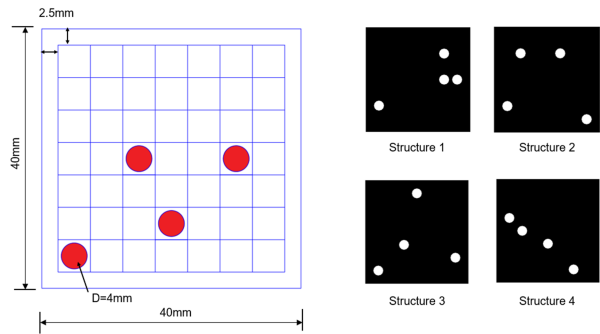
In this study, the residual stress is defined as the flexural stress in the post-peak part of the displace-load curve. According to Figure 5.8(c), the difference in flexural response (both flexural strength and residual stress) between different structures is very limited. After training the deep neural network using the 5,000 examples (4,000 for the training set and 1,000 for the test set), it was not possible to map structures to peak load/toughness since the performance of the ML model on the test set is poor. A possible reason is that the vascular orientation does not significantly influence the crack morphology since the tubes are perpendicular to the crack. As a result, the flexural response is not very sensitive to the change of vascular configuration. This could also be verified from the results in Chapter 4 (Figure 4.8), where the difference of peak load (and toughness) is very limited between specimens with a 2D and a 3D vascular system.

5.4.2. CALIBRATION FOR 2D MODEL

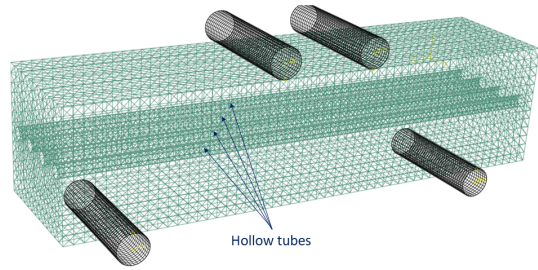
Instead of full 3D simulations, two-dimensional (2D) structures with pores in the middle span as vascular system are simulated to investigate the feasibility of vascular configuration optimization using machine learning (ML). The pores in the middle span could represent vasculature perpendicular to the plane of the beam. Compared with 3D model with tubes in y direction, the flexural response is more sensitive to the change of vascular configuration (i.e., position of the pores) since the crack path is influenced by the pores. To avoid the influence from crack initiation under 4-point bending, 3-point bending load is performed. Furthermore, a notch ($h/H=0.3$) is included in the beams. A schematic of 2D model with pores is shown in Figure 5.9. Note that these simulations have been used herein for data-driven optimization but have not been verified experimentally yet.

The input parameters for CDPM were taken from a published literature [12]. Uniaxial tensile and compressive tests were carried out to calibrate the model parameters related to the cementitious matrix. According to the obtained results (Figure 5.10), the calibrated parameters of CDPM for the used mortar are listed in Table 5.4. The mesh size is set as 0.5mm during the calibration process.

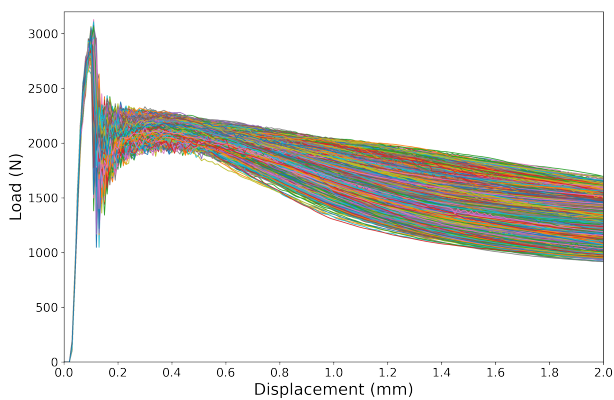
When simulating the 3-point bending test, the displacement of concrete structure gradually increases to 0.4mm with a speed of 0.02mm/s. The mesh size in the midspan is chosen as 0.5mm, which is kept same with the mesh size in the calibration process. To reduce the total number of elements, the mesh size gradually increases to 4mm, then



(a)



(b)



(c)

Figure 5.8: Schematics of 3D model for self-healing concrete with hollow tubes (a) Design space of vascular configuration; (b) One example of the simulated structure; (c) flexural response of different structures.

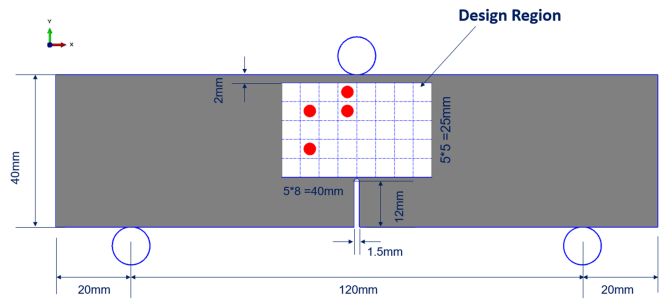


Figure 5.9: Schematic of 4-pore structure under 3-point bending.

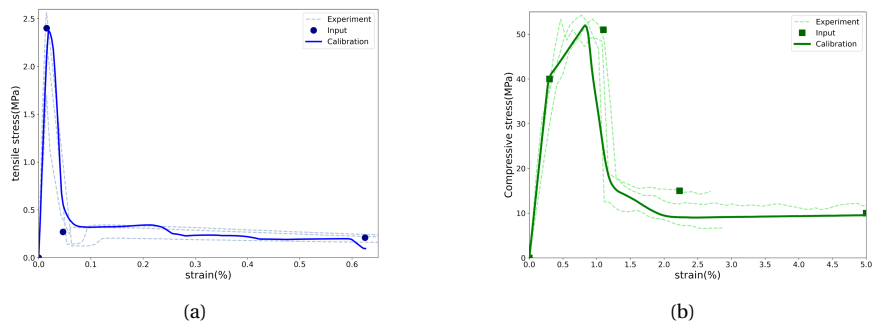


Figure 5.10: Calibration result for CDPM. (a) Tension; (b) Compression.

Table 5.4: Input parameters for fiber reinforced mortar in the CDPM model.

(a) Compressive parameters		(b) Tensile parameters	
Yield stress (MPa)	Inelastic strain (%)	Yield stress (MPa)	Inelastic strain (%)
40	0	2.4	0
53	0.008	0.15	0.05
15	0.022	0.1	0.976
10	0.047		

it stays 4mm for the remaining 40mm (as shown in Figure 5.11). A structure without pores is first created and meshed to act as the prototype. The mesh of the prototype is symmetric to eliminate the impact of mesh size on the numerical analysis. To avoid the influence of the mesh on the simulated response, structures with pores are generated based on the meshed prototype. As a result, the mesh of the structure is identical in all simulations, except for the existence of pores.

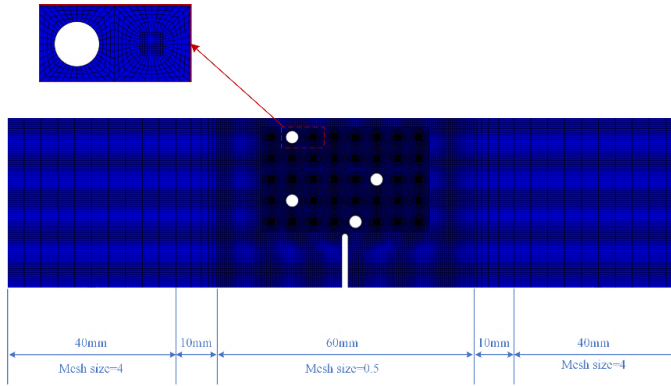
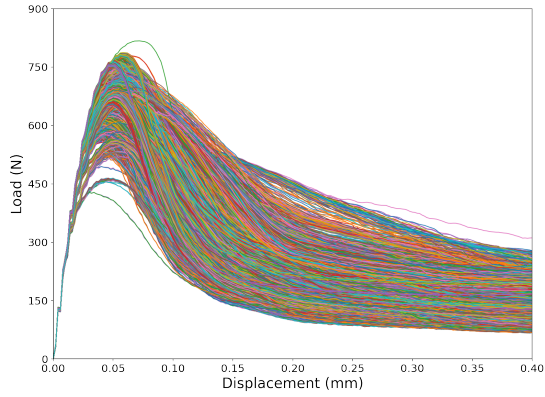


Figure 5.11: Mesh size of the 4-pore structure under 3-point bending.

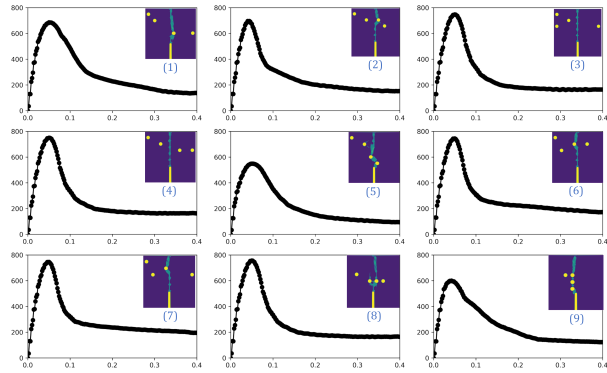
5.4.3. THE SIMULATION RESULTS OF CEMENTITIOUS MATERIALS WITH HOLLOW CHANNELS WITH 2D MODEL

Structures with 4 pores in the design region are modelled to investigate the influence of pore orientation on the fracture behavior. The simulated results of some examples are shown Figure 5.12.

Even though the post-peak part of the flexural stress curves shows similar ductile behavior due to the fibers in the mixture, the peak load as well as the residual stress is different when the position of pores changes. The peak load is higher when the crack hits less or no pores (see Figure 5.12(b)). The existence of pores has a great influence on the peak load when the pores are hit by the crack. However, if the crack does not hit the pores, the structure can be assumed to be not healable since the healing agent in the pores cannot reach the crack. Note that the flexural response may also be different when the cracks hit same number of pores. One possible reason is that these hit pores influence the crack morphology thereby causing different fracture behavior. For example, in Figure 5.12(b), when two pores are hit, the peak load of one structure (structure 8) is much higher than of the other one (structure 5). In this scenario, structure 8 is preferable since the structure is healable without significantly lowering the peak load. Instead of peak load, the area below the flexural stress curve (defined as toughness in Section 5.3.4) could be used to judge the applicability of vascular structures as self-healing cementitious materials. However, unlike the peak load (directly obtained from flexural stress curve), the toughness is calculated based on the simulated flexural stress curve. The truncated error may be introduced due to the limited vertical displacement during the numerical simulation because some structures



(a)



(b)

Figure 5.12: Mechanical response of different vascular structures of concrete (a) displacement-load curve; (b) some examples of displacement-load curve and the corresponding structure.

have higher residual stress at the displacement of 0.4mm. As a result, the prediction accuracy of the trained ML model may be lower when the target property is set as toughness.

5.5. FEASIBILITY OF USING MACHINE LEARNING FOR OPTIMIZATION

WHEN using machine learning (ML) approaches for optimization, one precondition is an accurate ML model for mapping the input (structures) to the output (target property). Therefore, the mapping relation between input and output should be created. In other words, the target property should be sensitive to the change of input (i.e., vascular configuration). It is called mapping relationship in this study.

On the other hand, the computational time must be considered as well. Machine learning is data-hungry and a large dataset benefits the training of ML model. If the computational time needed for a simulation is long, it could be extremely time-consuming to generate the dataset for model training. Therefore, two aspects, i.e., computational time and mapping relation, should be considered when evaluating the feasibility of numerical models for ML-based optimization. A summary of the three discussed numerical models considered for optimization herein, with varying assumptions and levels of complexity, is given in Table 5.5.

Based on Table 5.5, a 2D model with pores in the design space is the most suitable for vascular configuration optimization in vascular self-healing cementitious materials. For the 3D model with the ABS vascular network, the fracture of vasculature and the interaction between the cementitious matrix and the vascular significantly increase the computational time, making it impossible (in practical terms) to generate a large dataset for machine learning. In the 3D model with hollow channels, toughness is not sensitive to the change of vascular structure, and it is difficult to map structure to toughness using ML model. Therefore, the 3D model with hollow channels is not suitable for generating dataset for vascular optimization with machine learning approach.

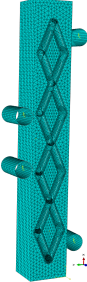
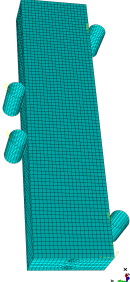
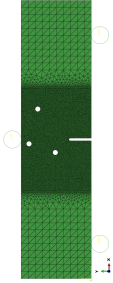
5.6. CONCLUSIONS

IN this chapter, self-healing cementitious materials with vascular network (or hollow channels) are numerically investigated. Numerical modelling is first used to simulate the flexural response of 3D-printed ABS vascular self-healing cementitious materials in chapter 3. To save computational time, a 2D model with pores in the middle span as vascular network is simulated and the fracture behavior of different structures is discussed. Based on the obtained results, the following conclusions can be drawn:

- The proposed numerical approach can provide an accurate simulation of the fracture behaviour of cementitious composites with 3D printed vascular networks. Even with vasculature prepared with various printing parameters, the simulated stress-crack width by the Concrete Damaged Plasticity model (CDPM) in Abaqus has shown excellent agreement with experimental results, in terms of

¹Intel (R) Xeon (R) W-2225 CPU @4.10GHz, 4 core and 8 logical processes; 32G Memory

Table 5.5: Comparison of numerical model for vascular self-healing cementitious materials.

Numerical model	3D model with ABS vascular	3D model with hollow tubes	2D model with pores in middle span
schematics			
Matrix	Plain mortar	Fiber reinforced mortar	Fiber reinforced mortar
Vascular type	3D-printed ABS vascular	Hollow channels	Hollow channels (pores)
Computational time per structure (min) ¹	399	10	2
Mapping relation	-	Not accurate	Yes

crack width and flexural strength under four-point bending. However, the numerical modelling of self-healing cementitious materials with 3D vascular systems is time-consuming.

- A 2D model with different pore orientation shows different flexural response in terms of peak load and toughness. The number of pores hit by crack tends to influence the peak load. However, sometimes the peak loads are different even when same number of pores are hit. Therefore, it is necessary to optimize the vascular configuration for higher peak load or toughness.
- After comparing the computational time and mapping relationship of three numerical models, 2D model with pores in the middle span is the most suitable numerical model for generating dataset for vascular configuration optimization through machine learning approach.

REFERENCES

- [1] Z. Wan, Y. Xu, Y. Zhang, S. He, and B. Šavija, *Mechanical properties and healing efficiency of 3d-printed abs vascular based self-healing cementitious composite: Experiments and modelling*, Engineering Fracture Mechanics **267**, 108471 (2022).
- [2] C. Joseph, A. D. Jefferson, B. Isaacs, R. Lark, and D. Gardner, *Experimental investigation of adhesive-based self-healing of cementitious materials*, Magazine of Concrete Research **62**, 831 (2010).
- [3] A. Formia, S. Terranova, P. Antonaci, N. M. Pugno, and J. M. Tulliani, *Setup of extruded cementitious hollow tubes as containing/releasing devices in self-healing systems*, Materials **8**, 1897 (2015).
- [4] D. Gardner, A. Jefferson, A. Hoffman, and R. Lark, *Simulation of the capillary flow of an autonomic healing agent in discrete cracks in cementitious materials*, Cement and Concrete Research **58**, 35 (2014).
- [5] K. Van Tittelboom, N. De Belie, D. Van Loo, and P. Jacobs, *Self-healing efficiency of cementitious materials containing tubular capsules filled with healing agent*, Cement and Concrete Composites **33**, 497 (2011).
- [6] H. Huang, G. Ye, and Z. Shui, *Feasibility of self-healing in cementitious materials—by using capsules or a vascular system?* Construction and Building materials **63**, 108 (2014).
- [7] Z. Li, L. R. de Souza, C. Litina, A. E. Markaki, and A. Al-Tabbaa, *A novel biomimetic design of a 3d vascular structure for self-healing in cementitious materials using murray's law*, Materials & Design **190**, 108572 (2020).
- [8] Z. Wan, Y. Xu, and B. Šavija, *Influence of printing direction on 3d-printed vascular based self-healing cementitious composites*, in MATEC Web of Conferences, Vol. 378 (EDP Sciences, 2023) p. 02027.
- [9] A. Jefferson, T. Selvarajoo, B. Freeman, and R. Davies, *An experimental and numerical study on vascular self-healing cementitious materials*, in MATEC Web of Conferences, Vol. 289 (EDP Sciences, 2019) p. 01004.
- [10] S. Chaudhari and M. Chakrabarti, *Modeling of concrete for nonlinear analysis using finite element code abaqus*, International Journal of Computer Applications **44**, 14 (2012).
- [11] Y. Xu and B. Šavija, *Development of strain hardening cementitious composite (shcc) reinforced with 3d printed polymeric reinforcement: Mechanical properties*, Composites Part B: Engineering **174**, 107011 (2019).
- [12] Y. Xu, E. Schlangen, M. Luković, and B. Šavija, *Tunable mechanical behavior of auxetic cementitious cellular composites (cccs): Experiments and simulations*, Construction and Building Materials **266**, 121388 (2021).

- [13] Y. Xu, H. Zhang, Y. Gan, and B. Šavija, *Cementitious composites reinforced with 3d printed functionally graded polymeric lattice structures: Experiments and modelling*, Additive Manufacturing **39**, 101887 (2021).
- [14] K. R. Hart and E. D. Wetzel, *Fracture behavior of additively manufactured acrylonitrile butadiene styrene (abs) materials*, Engineering Fracture Mechanics **177**, 1 (2017).
- [15] A. Nurizada and K. Kirane, *Induced anisotropy in the fracturing behavior of 3d printed parts analyzed by the size effect method*, Engineering Fracture Mechanics **239**, 107304 (2020).
- [16] A. Hillerborg, M. Mod  er, and P.-E. Petersson, *Analysis of crack formation and crack growth in concrete by means of fracture mechanics and finite elements*, Cement and concrete research **6**, 773 (1976).
- [17] Y. Xu, H. Zhang, B. Šavija, S. C. Figueiredo, and E. Schlangen, *Deformation and fracture of 3d printed disordered lattice materials: Experiments and modeling*, Materials & Design **162**, 143 (2019).

6

OPTIMIZATION OF VASCULAR CONFIGURATION OF SELF-HEALING CEMENTITIOUS MATERIALS USING GENERATIVE DEEP NEURAL NETWORK

In this chapter, optimization of vascular configuration in self-healing cementitious materials is carried out with generative neural networks. Considering the increasing discrepancy between the optimized input and the prescribed input domain as the number of design loops increases for generative neural networks, a correction technique is incorporated into the generative deep neural network (GDNN). The vascular configuration was optimized towards increased peak load and toughness. Based on the obtained results, it was feasible to optimize vascular configuration by fixing the weights of the DNN model and training the input. After optimization with the well-trained DNN models, structures with higher peak load or toughness were obtained. The optimization of vascular configuration towards higher toughness is less effective compared with that of peak load. A possible reason is that the DNN model with toughness as the target is less accurate, making it difficult to find a concrete structure as good as the DNN model with peak load as the target. A possible solution would be to increase the accuracy of the DNN model by training it with a larger dataset, which would however significantly increase the computational costs.

Parts of this chapter were published in Materials (2021) [1]; Construction and Building Materials (2023) [2]; and Advanced Intelligent Systems (2023) [3].

6.1. INTRODUCTION

EXCEPT for experiments, numerical simulations can also be used to optimize materials. For example, gradient-based topology optimization has been widely used for optimization due to its time-effectiveness [4–6]. Topology optimization works by calling a finite element analysis (FEA) of a structure, calculating the gradient of the objective function with respect to the design variables, and updating the design variables [7]. This process is repeated until convergence. However, there are three major challenges when using gradient-based topology optimization: (1) the local minima problem; (2) the calculation of analytical gradients; (3) the availability of objective functions [8]. Some researchers attempt to solve these problems by combining topology optimization and machine learning (ML) [9]. In this way, the computational burden of generating the data and the training process is non-trivial, but after proper training, the model can provide a gradient-free topology design tool [10]. However, some intrinsic problems caused by topology optimization remain unsolved.

Inspired by generative machine learning models such as auto-encoders and generative adversarial networks (GANs) [11], Gu and coworkers developed generative machine learning algorithms including generative inverse design networks (GIDNs) [8] and hybrid neural network and genetic optimization (NN-GO) [12] for inverse material design. Generative deep neural networks (GDNNs) effectively avoid problems associated with topology optimization: the local minima are significantly mitigated by random initialization of the input; gradients could be calculated rapidly by backpropagation; and the optimization target is the output of the neural network. Although the GDNN was capable of finding a structure with increased toughness in multiple iterations in their study, the increasing discrepancy between the optimized input and the prescribed input domain compromises the optimization effectiveness of GDNN.

To date, no advanced optimization approaches based on ML have been developed for vascular self-healing cementitious materials. Herein, we show the feasibility of vascular configuration optimization with generative deep neural networks (GDNN). To mitigate the increasing discrepancy between the optimized input and the prescribed input domain as the number of design loops increases, a correction technique is incorporated to generative deep neural networks to form ‘*corrected GDNN*’. The convergence and optimization effectiveness of the corrected GDNN and the uncorrected GDNN (called ‘*original GDNN*’ hereafter) are compared. A dataset is first created by numerically simulating the mechanical response of fiber reinforced concrete beams subjected to 3-point bending using Abaqus software to map self-healing concretes with different vascular configurations to the target mechanical property. The calibration of inputs is presented in Chapter 5. Data representation and ML method are first introduced in detail (Section 6.2). The statistical properties of the dataset are then discussed (Section 6.3). Afterwards, vascular configuration optimization towards a higher peak load (Section 6.4) and toughness (Section 6.5) is performed. The concrete structures before and after ML optimization are compared and conclusions are drawn based on the obtained results (Section 6.6).

6.2. DATA REPRESENTATION AND MACHINE LEARNING METHOD

WHEN using machine learning for optimization, the first step is to establish a relationship between the input (concrete structure and vascular configuration) and the output (peak load or toughness). Therefore, a large dataset is needed for the training of ML model. According to Chapter 5, 2-dimensional models with plane stress are built to allow fast computation. The optimization constrain is that 4 pores are placed out of the 40 positions in the middle span of a beam to act as the vascular reservoirs of the healing agent, perpendicular to the longitudinal axis of the beam (Figure 5.9).

6.2.1. DATA REPRESENTATION

It is of great importance to define the input and output when creating a dataset for ML [13]. Identifying the characterizing features is important to accelerate the training process and minimize the cost function [1]. To accelerate the training process of the ML model, the information without much variance should be removed. In this work, the concrete structure outside the design space is identical for all investigated structures. Therefore, the characterization of concrete structures can be effectively represented by the design space in the middle span. The design space can be described by the state of the 40 locations, i.e., with or without pores.

For convenience, a location is encoded as a 1 if there is a pore, otherwise it is encoded as a 0. In this way, one concrete structure could be encoded as a matrix with elements of 1 or 0. Subsequently, the matrix is flattened to a 40-dimensional vector, which is used as the input for DNN model. The input representation can be found in Figure 6.1(a).

As to the output representation, it is less complicated than the input since it is a scalar corresponding to the mechanical property that we aim to optimize. To verify the feasibility of optimizing the concrete structure for a certain mechanical property with the data representation method, the target is first set as peak load, which can be directly obtained from the simulated load-displacement curve. Afterwards, toughness, which is defined by the area below the load-displacement curve (Equation 6.1), is used as the target to search for vascular configuration in which more pores are hit by the crack. The structure with more pores hit by the crack is preferable for self-healing since the healing agents could enter the cracks from pores hit by the crack. One example of target representation could be seen in Figure 6.1(b).

$$Toughness = \int_0^{0.4} F ds \quad (6.1)$$

Here F and s are load and displacement of the load-displacement curve, respectively.

6.2.2. ARTIFICIAL NEURAL NETWORK (ANN)

Artificial Neural Network (ANN) is a powerful algorithm for processing data by simulating the functioning of the biological neurons [14]. ANN uses linking functions to correlate features with targets. According to previous research [15], a deep network can represent functions of increasing complexity by adding more layers and more units

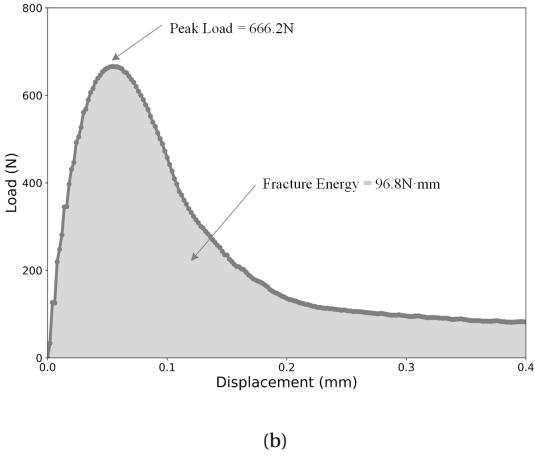
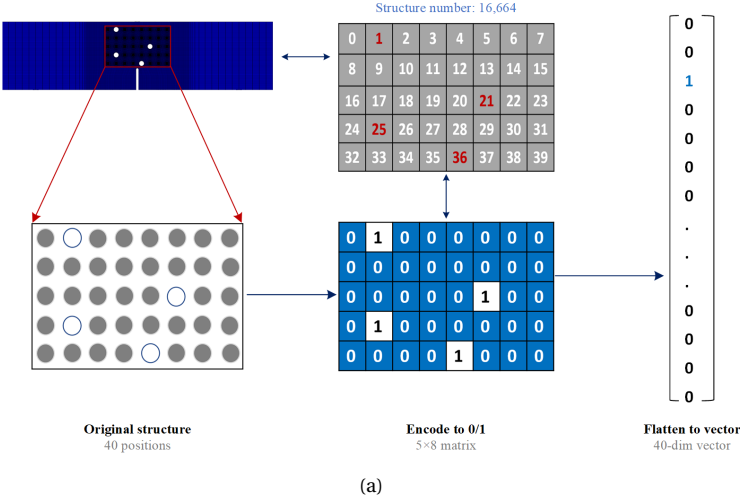


Figure 6.1: Data representation (a) input representation (b) output representation.

within a layer. Theoretically, a neural network could approximate any function mapping from any finite dimensional discrete space to another.

There are two processes for ANN: forward propagation and backward propagation. During the forward propagation process, the artificial neuron sums the weighted inputs from the neurons in the previous layer (or input) and then uses activation functions (such as ReLu function, sigmoid function, tanh function, or others) to carry out nonlinear operation [16]. After obtaining the predicted target, the gap between predicted target and actual target is used to improve the weights in each layer, using backward propagation. In the backward propagation process, optimization algorithms such as stochastic gradient descent (SGD), Root Mean square prop (RMSprop), and Adaptive moment estimation (Adam) are employed to improve the weight matrix (W) and bias matrix (b). The two processes continue until the predicted values are close enough to the actual ones (measured by loss function). A general architecture of an ANN is shown in Figure 6.2 [17]. The calculation of neurons in the l^{th} layer is as Equations 6.2-6.7.

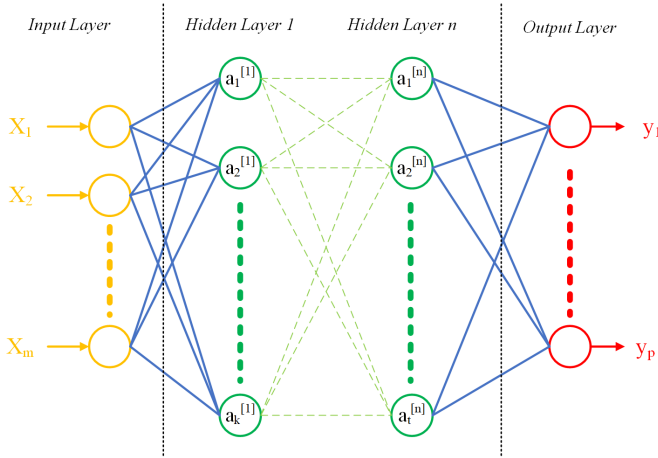


Figure 6.2: General structure of an Artificial Neural Network (ANN).

Forward propagation:

$$Z^{[l]} = W^{[l]} A^{[l]} + b^{[l]} \quad (6.2)$$

$$A^{[l]} = g^{[l]}(Z^{[l]}) \quad (6.3)$$

Backward propagation:

$$dZ^{[l]} = dA^{[l]} * g^{[l]'}(Z^{[l]}) \quad (6.4)$$

$$dW^{[l]} = \frac{1}{m} dZ^{[l]} * A^{[l-1]T} \quad (6.5)$$

$$db^{[l]} = \frac{1}{m} \sum_{i=1}^m dZ^{[l]}(axis = 1) \quad (6.6)$$

$$dA^{[l-1]} = W^{[l]T} * dZ^{[l]} \quad (6.7)$$

where $W^{[l]}$, $b^{[l]}$ are the weight matrix and bias matrix of layer l ; $Z^{[l]}$ is the weighted sum matrix of layer l ; $A^{[l]}$ is the activation of units in layer l ; $A^{[l]} = [a_1^{[l]}, a_2^{[l]}, \dots, a_k^{[l]}]$, $g^{[l]}(x)$ is the activation function of layer l ; $dZ^{[l]}$, $dW^{[l]}$, $db^{[l]}$ are the derivative of the weighted sum matrix $Z^{[l]}$, weight matrix $W^{[l]}$, bias matrix $b^{[l]}$ in layer l , respectively; and $dA^{[l-1]}$ is the derivative of activation of units in layer $l-1$.

In this study, DNN with 6 hidden layers is established to predict the target property (peak load and toughness) based on the 40-dimensional vector representing the concrete structure with different vascular configurations. The number of neurons of the hidden layers is chosen as 512 for all hidden layers after hyperparameter tuning.

6.2.3. INVERSE DESIGN WITH NEURAL NETWORK

The optimization method used here is similar to the research of Chen and Gu [8]. Two steps, i.e., weights (of DNN) training and input optimization, are used during the process. First, the weights (W , b) of DNN are trained to accurately map concrete structures to the target mechanical property with the dataset. 10,000 structures are randomly chosen and then numerically simulated (using Abaqus). The dataset is split with a split of 90-10% between the training and test sets, i.e., trainset (size=9,000) and test set (size=1,000). The batch size is chosen as 512 after hyperparameter tuning. According to [17], coefficient of determination (R-squared) is selected as a metric to evaluate the accuracy of the ML models (Equation 6.8). Mean squared error (MSE) is employed as the loss function (Equation 6.9). Adam is used as the optimizer for the back-propagation with the default learning rate (0.001). ReLu function is employed as the activation function. The training process stops when the loss function is steady. The weights contributing to the highest R-squared on test set is saved.

$$R^2(y, y') = 1 - \frac{\sum (y_i - y'_i)^2}{\sum (y_i - \bar{y})^2} \quad (6.8)$$

$$MSE = \frac{1}{n} \sum_{i=1}^{i=n} |y - y'|^2 \quad (6.9)$$

where y_i and y'_i are the actual and predicted values of the i^{th} sample, and \bar{y} is the mean target values.

After the DNN is well trained, the weights of the DNN are fixed while the input (X) is set as the trainable variables to optimize input for higher mechanical property. To drive the DNN to search for the inputs (X) with maximum target property, we define the negative of target as the loss function. During the optimization process, 4,000 inputs (40-dimensional vector with four 1's and thirty-six 0's) are randomly sampled. The random initialization is to avoid the influence of initial exploration points to the optimization process. Since the weights of the trained DNN are frozen, the backpropagation process will drive the changes of input to minimize the loss function (i.e., higher mechanical properties). Adam is also used as the optimizer with a learning rate of 0.01 for the back-propagation to accelerate the optimization process. 40,000 epochs are performed in this

process since the loss function based on post-processed input keeps unchanged after that.

Note that the learning rate is set as 0.01 and the elements after backpropagation are decimals, which fails to represent the position state (with or without pores). Therefore, it is necessary to convert the elements to 0/1 to describe the state of positions by post-processing. We convert the positions with the maximum 4 elements to 1's and the rest to 0's. This way, all the ML-recommended inputs are 40-dimensional vectors with four 1's out of 40 positions. Then, the 40-dimensional vectors are reshaped into matrices and decoded into concrete material structures. The schematics of the post-processing/correction is shown in Figure 6.3. Those ML-recommended structures are numerically verified with Abaqus software and their corresponding mechanical properties are re-calibrated. Finally, the concrete structure with the highest target property is selected from the ML-recommended dataset and compared with the original dataset.

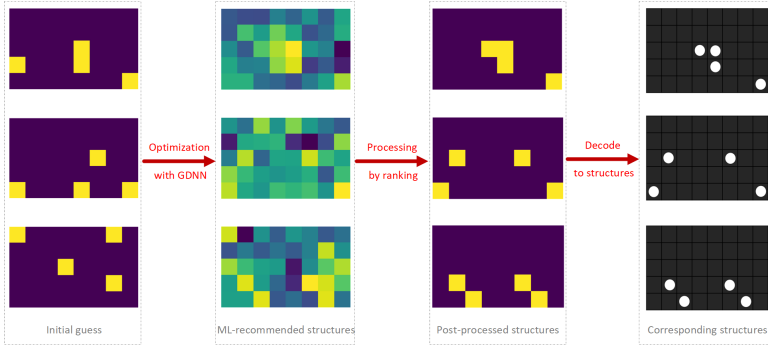


Figure 6.3: Post-processing of ML-recommended input.

For the corrected GDN, input correction is performed during the optimization process instead of only post-processing at the end of the optimization process. Therefore, the original GDN can be regarded as a special case of corrected GDN with a large correction frequency. Considering that the loss function during the optimization process is defined by the negative sum of peak load or toughness, the average negative loss function based on the corrected input (called average peak load or toughness hereafter) is used as an index to monitor the optimization state. The schematics of the corrected GDN is shown in Figure 6.4.

6.3. STATISTICAL PROPERTIES OF THE DATASET

To train the neural network, 10,000 examples are randomly chosen and simulated to generate the dataset (9,000 examples for trainset and 1,000 examples for test set). The histograms of peak load and toughness are shown in Figure 6.5(a) and 6.5(b), respectively. The structures with highest peak load and toughness in the dataset (10,000 examples) are shown in Figure 6.5(c) and 6.5(d) respectively. The statistical properties of the targets are shown in Table 6.1.

The maximum peak load and toughness are 784.30N and 173.49N·mm, respectively.

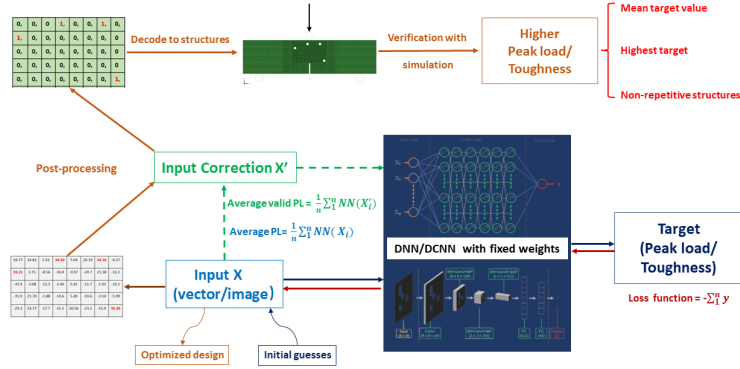


Figure 6.4: The schematic of the corrected GDN.

Table 6.1: Statistical properties of the dataset.

	Peak load (N)	Toughness (N·mm)
Mean value	708.78	110.24
Standard deviation	45.22	11.53
Maximum value	784.30	173.49
Minimum value	427.76	67.27
Reference	753.56	108.01

Except for the structures with 4 pores, the structure without pores is also numerically calculated as the reference. Based on Table 6.1, the highest toughness is much larger than the reference (108.01N·mm). The largest peak load is slightly higher than the reference (753.56N), which may be caused by the simulation accuracy. The corresponding concrete structures with the highest peak load and the highest toughness are shown in Figure 6.5(c) and 6.5(d), respectively. As shown in Figure 6.5(c) and 6.5(d), the peak load of the concrete structure with the highest toughness is low and vice versa. The residual stress is defined herein as the flexural stress in the post-peak part of the displace-load curve. Therefore, the concrete structure the with the highest peak load has lower residual stress than the structure with highest toughness in the post peak part. In addition, the crack hits less pores than in the case of the structure with highest toughness.

6.4. OPTIMIZATION FOR MAXIMUM PEAK LOAD

To search for a vascular configuration with a higher peak load, a neural network is first trained to map the concrete structure to the peak load. The prediction accuracy of the well-trained DNN model is shown in Figure 6.6. It is obvious that the performance of the neural network model is remarkable with a R-squared of 0.9898 on the test set.

After the neural network is well trained, 4,000 examples are randomly generated as initial structures for optimization. To keep this process reproducible, the random seed is

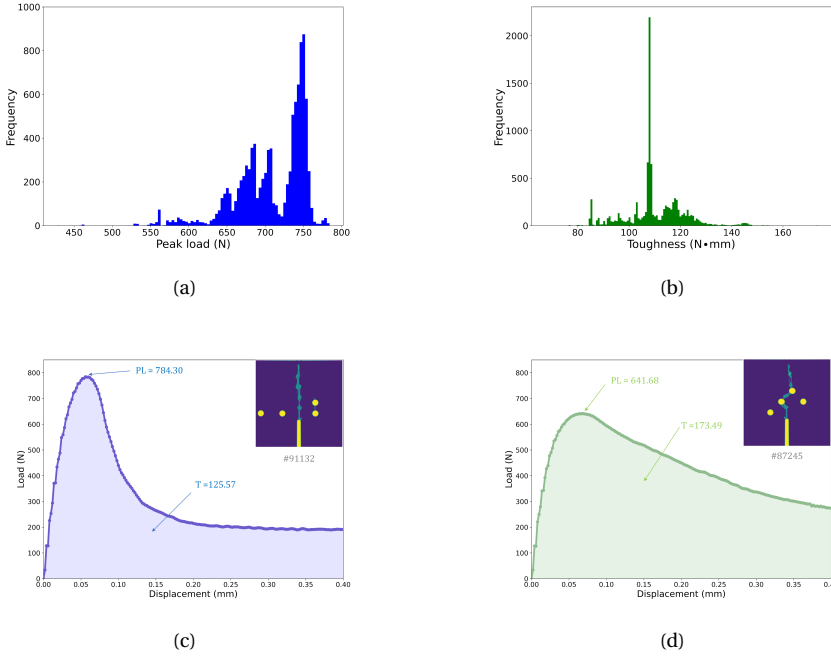


Figure 6.5: (a) Histogram of peak load; (b) Histogram of toughness; (c) structure with the highest peak load; (d) structure with highest toughness (in the 10,000 examples).

fixed to ensure that the same examples are generated in different cases. These examples are fed into the neural network and ran for 40,000 epochs. To illustrate the optimization process, the negative of average loss function (average peak load change), instead of loss is presented to see the improvement of mean (predicted) peak load. The changes of average peak load are compared when the correction frequency changes. The result is shown in Figure 6.7. Note that the average peak load is calculated based on the valid inputs (vectors with four 1's and thirty-six 0's).

For the original GDNN, the average peak load dramatically increases in the first 2,000 epochs and keeps increasing steadily after that (grey dashed line). In other words, the initial concrete structures are optimized towards higher peak load. The average peak load after 40,000 epochs is 745.38N, which increases by 5.23% from the initial guess (708.35N).

Compared with the original GDNN, the average peak loads from the corrected GDNN are higher after 40,000 epochs, except when the correction frequency is 100. The average peak load increases as the increase of correction frequency. However, the speed of increase gradually decreases after the correction frequency of 400. Considering that the original GDNN could be regarded as corrected GDNN with a large correction frequency (40,000 or even larger in this study), the average peak load should decrease after the correction frequency continues increasing. When correction frequency is

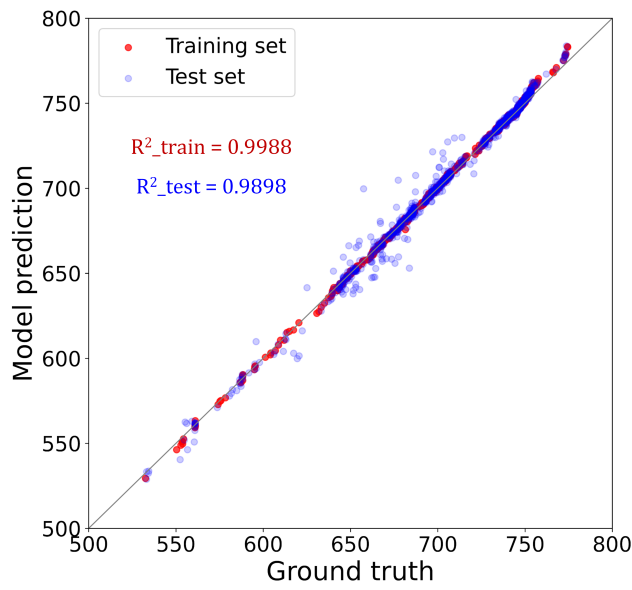


Figure 6.6: Prediction accuracy of peak load.

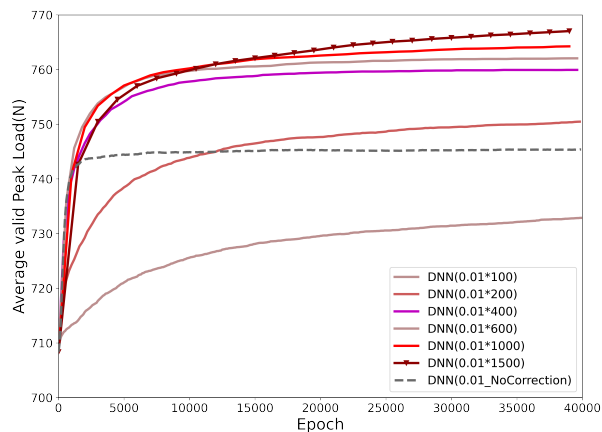


Figure 6.7: Change of the average peak load with different correction frequencies (the numbers in the parentheses are learning rate and the correction frequency, respectively).

1,500, the average peak load after 40,000 epochs is 767.03N, which increases by 8.28% from the initial guess. The ML-recommended structures will be verified by numerical simulation and the concrete material structure with highest peak load will be selected.

As mentioned above, the ML-recommended results are not (directly) the structures we needed due to the decimal values after optimization. To correctly describe the state of the positions, these results are converted into 0/1 binary values by ranking the 40 values. Subsequently, those post-processed inputs are decoded into the concrete structures. It is found that the 4,000 initial structures converge to 622 and 82 unique concrete structures for original GDNN and corrected GDNN (with correction frequency of 1,500) respectively. The histogram of 4,000 recommended structures with the original GDNN and the corrected GDNN (with correction frequency of 1,500) is shown in Figure 6.8.

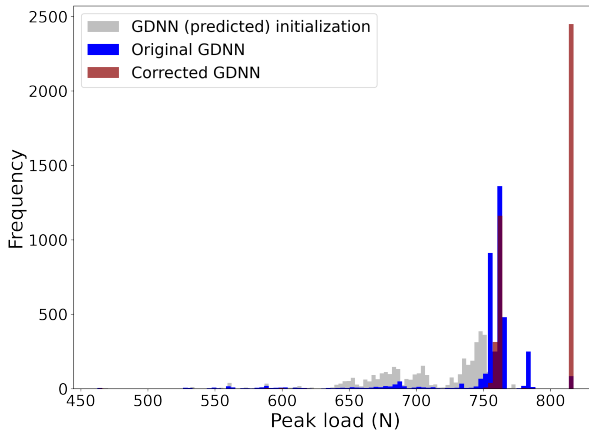


Figure 6.8: Histogram of ML-recommended structures (peak load).

The overall peak loads of ML-recommended structures are higher than that of the original dataset (Figure 6.8). The concrete structures improve for higher peak load after the optimization process using GDNNs. Compared with the original GDNN, the optimization effectiveness of the corrected GDNN is even higher since the histogram moves further right with an average peak load of 794.53N. Among the optimized structures, the concrete structure with the highest peak load is selected. It is worth mentioning that there are 84 and 2,449 initial structures that converge to the best structure (i.e., the structure with the highest peak load) for original GDNN and corrected GDNN, respectively. Therefore, correction during the optimization process is beneficial to search for a structure with higher peak load. The corresponding load-displacement curve (calculated in Abaqus) is shown in Figure 6.9.

The peak load of the ML-recommended structure is 817.29N, which is an increase of 4.21% from the concrete structure in the original dataset (see Figure 6.9). In the ML-recommended concrete material structure, the main crack does not hit the pores, which

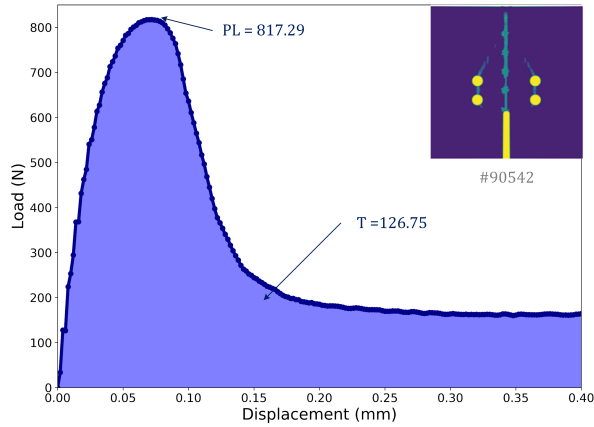


Figure 6.9: ML-recommended structure with highest peak load.

is why the structure has the highest peak load. Clearly, while this is certainly optimal in terms of peak load, it is useless in terms of vascular self-healing: self-healing can only be triggered if the crack hits a pore (i.e., the vasculature).

6.5. OPTIMIZATION FOR MAXIMUM TOUGHNESS

BASED on the result in section 6.4, it is feasible to optimize concrete structure towards higher peak load using the proposed data representation method and GDNN. Therefore, the neural network is retrained to map the concrete structure to toughness, which is calculated from the load-displacement curve. The prediction accuracy of the well-trained DNN model is shown in Figure 6.10. The performance of the DNN model is relatively good with a R-squared of 0.8693 on test set. However, it is much poorer than the performance of the peak load one. A possible reason is that some concrete structures still have large residual stress (about 300N) when the displacement reaches 0.4mm, which significantly underestimates the toughness. As a result, the target is less accurate than the peak load.

After the neural network is trained, 4,000 initial guesses are also used as starting points for the optimization process. Similarly, these examples are fed into the DNN model and ran for 40,000 epochs. The average toughness change with different correction frequencies is shown in Figure 6.11. From Figure 6.11, the average toughness increases during the optimization process, manifesting that the inputs changes towards higher toughness. For the original GDNN, the average (predicted) toughness based on post-processed input after 40,000 epochs is 132.58N-mm, which is an increase of 20.44% compared with the average toughness of the initial structures.

Similar to peak load optimization, correction during the optimization process helps further improve the optimization effectiveness since higher average toughness is achieved through the corrected GDNN after 40,000 epochs. In particular, the average

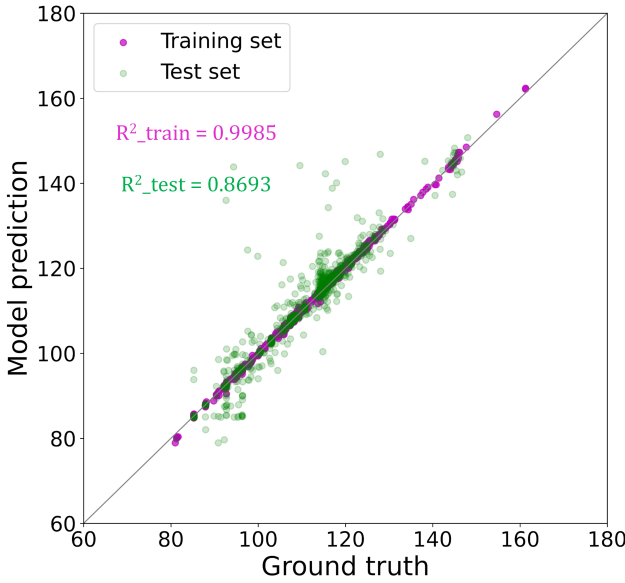


Figure 6.10: Prediction accuracy of toughness.

toughness increases when the correction frequency increases from 100 to 1,500. The rate of increase is almost unchanged after epoch of 1,000. The average toughness is 162.74N·mm, which is much higher than that of the original GDNN (132.58N·mm).

After postprocessing and decoding the ML-recommended inputs into 4-pore structures, the 4,000 initial structures converge to 2,127 and 217 unique concrete structures for original GDNN and corrected GDNN respectively. Therefore, the correction significantly increases the convergence and reduces the computation needed for verification. The histogram of 4,000 recommended structures with original GDNN and corrected GDNN (with correction frequency of 1,500) is shown in Figure 6.12.

The overall toughness of ML-recommended structures optimized by original GDNN and corrected GDNN are higher than that of the original dataset (see Figure 6.12). The average toughness after optimization with the original GDNN is 134.14N·mm, which is close to the predicted value (132.58N·mm). Therefore, the model is capable of mapping concrete structures to toughness. Compared with the original GDNN, the optimization effectiveness of corrected GDNN is even higher since the histogram moves further right with an average toughness of 165.68N·mm.

Among the optimized structures, the concrete structure with highest toughness is selected. Although the corrected GDNN has better convergence and optimization effectiveness (i.e., higher average toughness), no better concrete structure is found after the optimization. In other words, the highest toughness of the optimized structure is

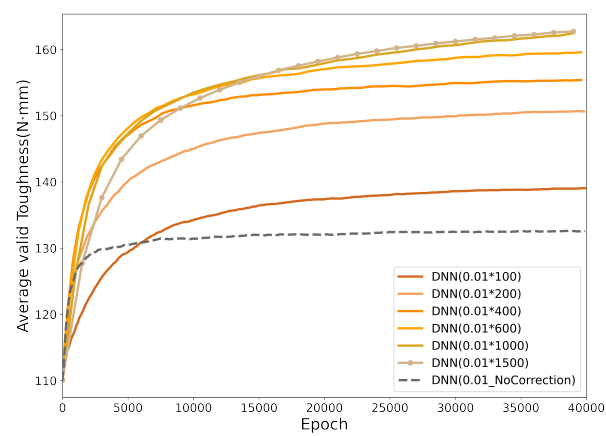


Figure 6.11: Change of toughness with different correction frequencies.

6

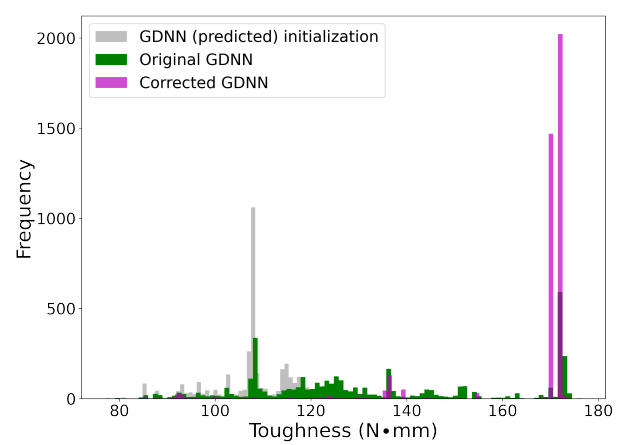


Figure 6.12: Histogram of ML-recommended structures (toughness).

still 173.49N·mm. However, a vascular configuration with a higher toughness was found by the original GDNN. The corresponding load-displacement curve is shown in Figure 6.13.

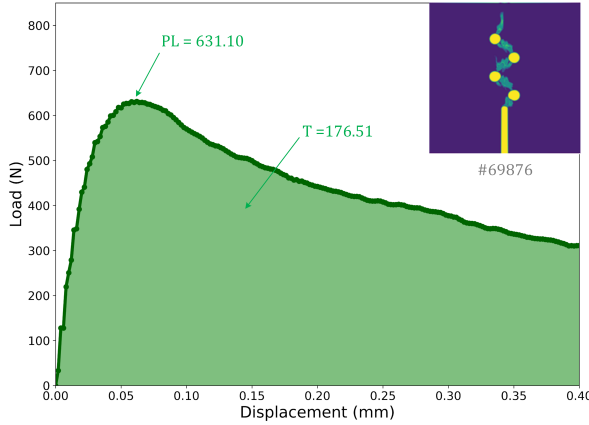


Figure 6.13: ML-recommended structure with highest toughness.

The ML-recommended structure has a slightly higher toughness (176.51N·mm) than the one in the original dataset (173.49N·mm) (see Figure 6.13). The difference between the best structures in the dataset and the GDNN-optimized one is very limited. Compared with the peak load, the mapping from concrete structure to toughness is less accurate. In addition, the initial guess also influences the final optimized results. Although correction helps improve the convergence and optimization effectiveness, accurate mapping remains extremely important for concrete structure optimization.

Compared with the best structure (structure with highest toughness) in the original dataset, 4 pores of the optimized structure are hit/damaged by the crack, making the structure more ductile after the crack occurs. As a result, the toughness is slightly larger than the original concrete structure. For self-healing, the crack could be regarded to be healed by the sufficient healing agent supplied by the 4 pores.

6.6. CONCLUSIONS

IN this chapter, concrete structures were optimized towards different target mechanical properties using generative deep neural network (GDNN). The optimization objective is the concrete structures with 4 pores representing vascular reservoirs of the healing agent in the 40 positions in the middle span of the concrete beam. To investigate the feasibility of using GDNN to optimize a concrete structure with the proposed data representation method, peak load is set first as optimization target. Subsequently, toughness is defined as target to optimize a concrete structure for good self-healing capacity. Based on the presented results, the following conclusions can be drawn:

- DNN model is able to accurately predict the peak load and toughness based on concrete structures with the R-squared of the three ML models on test set are over 0.87. However, the DNN models become less accurate when the target changes from a direct mechanical property (peak load) to an indirect mechanical property(toughness). A possible reason is that toughness may be slightly underestimated for some concrete structures which have high residual stress when the displacement reaches 0.4mm.
- It is feasible to optimize concrete structure by fixing the weights of the DNN model and training the input (concrete structures). After optimization with the well-trained DNN with frozen weights, the largest peak load and toughness of the ML-recommended concrete structures increase.
- For peak load, correction during optimization helps increase the convergence and optimization effectiveness compared with original GDNN. For corrected GDNN, there are only 82 unique structures after the optimization process. In addition, 2,449 out of 4,000 structures converge to the best structure.
- For toughness, the corrected GDNN also has better convergence and optimization effectiveness with 217 unique structures. Furthermore, the average toughness obtained by corrected GDNN is 176.51N·mm, which is much higher than that of original GDNN (134.14N·mm).
- A structure with the highest toughness is discovered by the original GDNN. Compared with the structure with the highest toughness in the training dataset, 4 pores of the optimized structure are hit/damaged by the crack, making the structure more ductile after the crack occurs.

REFERENCES

- [1] Z. Wan, Y. Xu, and B. Šavija, *On the use of machine learning models for prediction of compressive strength of concrete: influence of dimensionality reduction on the model performance*, *Materials* **14**, 713 (2021).
- [2] Z. Wan, Z. Chang, Y. Xu, and B. Šavija, *Optimization of vascular structure of self-healing concrete using deep neural network (dnn)*, *Construction and Building Materials* **364**, 129955 (2023).
- [3] Z. Wan, Z. Chang, Y. Xu, Y. Huang, and B. Šavija, *Inverse design of digital materials using corrected generative deep neural network and generative deep convolutional neural network*, *Advanced Intelligent Systems* **5**, 2200333 (2023).
- [4] Z.-L. Zhao, S. Zhou, K. Cai, and Y. M. Xie, *A direct approach to controlling the topology in structural optimization*, *Computers & Structures* **227**, 106141 (2020).
- [5] Y. Zhou, H. Zhan, W. Zhang, J. Zhu, J. Bai, Q. Wang, and Y. Gu, *A new data-driven topology optimization framework for structural optimization*, *Computers & Structures* **239**, 106310 (2020).
- [6] R. Sivapuram, P. D. Dunning, and H. A. Kim, *Simultaneous material and structural optimization by multiscale topology optimization*, *Structural and multidisciplinary optimization* **54**, 1267 (2016).
- [7] S. Kumar, S. Tan, L. Zheng, and D. M. Kochmann, *Inverse-designed spinodoid metamaterials*, *npj Computational Materials* **6**, 73 (2020).
- [8] C.-T. Chen and G. X. Gu, *Generative deep neural networks for inverse materials design using backpropagation and active learning*, *Advanced Science* **7**, 1902607 (2020).
- [9] A. Chandrasekhar and K. Suresh, *Tounn: Topology optimization using neural networks*, *Structural and Multidisciplinary Optimization* **63**, 1135 (2021).
- [10] N. K. Brown, A. P. Garland, G. M. Fadel, and G. Li, *Deep reinforcement learning for engineering design through topology optimization of elementally discretized design domains*, *Materials & Design* **218**, 110672 (2022).
- [11] I. Goodfellow, J. Pouget-Abadie, M. Mirza, B. Xu, D. Warde-Farley, S. Ozair, A. Courville, and Y. Bengio, *Generative adversarial networks*, *Communications of the ACM* **63**, 139 (2020).
- [12] S. Lee, Z. Zhang, and G. X. Gu, *Generative machine learning algorithm for lattice structures with superior mechanical properties*, *Materials Horizons* **9**, 952 (2022).
- [13] J. Heaton, *An empirical analysis of feature engineering for predictive modeling*, in *SoutheastCon 2016* (IEEE, 2016) pp. 1–6.
- [14] E. Aarts, J. Korst, and W. F. Verhaegh, *Algorithms in ambient intelligence* (Springer, 2004).

- [15] Y. LeCun, Y. Bengio, and G. Hinton, *Deep learning*, nature **521**, 436 (2015).
- [16] M. Alnaggar and N. Bhanot, *A machine learning approach for the identification of the lattice discrete particle model parameters*, Engineering Fracture Mechanics **197**, 160 (2018).
- [17] W. B. Chaabene, M. Flah, and M. L. Nehdi, *Machine learning prediction of mechanical properties of concrete: Critical review*, Construction and Building Materials **260**, 119889 (2020).

7

AUTOMATIC ENHANCEMENT OF VASCULAR CONFIGURATION FOR SELF-HEALING CEMENTITIOUS MATERIALS THROUGH REINFORCEMENT LEARNING APPROACH

Designing concrete with high self-healing capacity by optimizing a specific arrangement of vascular structure is of great importance. In this chapter, an automatic optimization method based on a reinforcement learning (RL) approach is proposed to enhance the vascular arrangement of concrete with high self-healing capacity. The goal of the model is to optimize a concrete beam with 4 pores (representing a vascular network) positioned in the beam midspan within a design space of 40 possibilities. The optimization is performed by the interaction between RL agent and Abaqus simulation environment with the change of target properties as a reward signal. The results illustrate that the RL approach is able to automatically enhance the vascular arrangement. The RL optimization method is able to identify the structure with high toughness in the new optimization task for 4-pore concrete structure.

7.1. INTRODUCTION

ALTHOUGH vascular configuration in self-healing cementitious materials could be optimized towards higher peak load or toughness with the generative deep neural network (GDNN) in Chapter 6, there are still several issues in the optimization process: (1) a large dataset is indispensable to train the DNN model; (2) the ML-recommended structures must be verified by the mechanical simulation software to obtain the best structure; (3) the ML model has to be re-trained with a new dataset when the optimizing structure or the target property are changed. In recent years, reinforcement learning (RL) has shown significant success in solving complex real-world problems in material optimization [1–3]. Compared with other ML algorithms, reinforcement learning takes the actions maximizing the future rewards by iteratively interacting with the environment [4]. Furthermore, the algorithm does not rely on prior knowledge nor the large amount of initialization samples.

In this chapter, the vascular configuration of vascular self-healing concrete (SHC) is enhanced with reinforcement learning (RL). Q-network is adopted to describe the state-action value [5, 6]. To promote convergence of the Q-network, experience replay and two separated networks are used [7]. Similar to Chapter 6, the objective is to maximize peak load or toughness of the concrete beams under a certain restraint. To enable automatic optimization of vascular configuration through the interaction, the 3-point bending test of concrete beam with different vascular arrangements is modelled with Abaqus/Explicit. The constraint is that 3/4 pores are arranged in the design region. The data representation is introduced in section 7.2. The formation of Markov decision process (MDP) is shown in section 7.3 and the deep Q-learning approach to optimize vascular structures is described in section 7.4. Optimization of 3-pore concrete structure with two updating strategies (3→2→3 and 3→4→3) is compared and analyzed, and the result and discussion are provided in section 7.5 and 7.6. Finally, a new optimization of 4-pore concrete structure is carried out (section 7.7).

7.2. DATA REPRESENTATION

TO investigate concrete structure optimization via the interaction between the simulation software and the RL agent, 3-point bending tests on notched concrete specimens are numerically simulated. The pores in the design region act as the channels for transporting the self-healing agents. Based on the load-displacement curve, different mechanical properties are obtained and set as the optimization targets to calculate the reward signals. The used concrete structure with 4 pores is the same with Chapter 6.

7.2.1. STRUCTURE REPRESENTATION

To enable the automatic optimization process, an input file for numerical simulation should be automatically generated based on the updated state after taking an action. Although the concrete structure seems complicated, the structures could be characterized by the difference in the design region. More details could be found in Figure 6.1(a) in Chapter 6.

In the simulation environment, the 40 positions are numbered from 0 to 39 in

accordance with the Python programming convention. The total design space for structures with 3 and 4 pores is 9,880 (C_{40}^3) and 91,390 (C_{40}^4) respectively. The 3-pore structure is sequentially encoded from 0 (combination 0, 1, 2) to 9,879 (combination 37, 38, 39) and the same goes for 4 pores (0 for combination 0, 1, 2, 3; and 91,389 for combination 36, 37, 38, 39). Based on the updated state after taking an action, a structure number ranging from 0 to $C_{40}^N - 1$ ($N=2, 3, 4$) is passed to the Abaqus environment. Afterwards, the corresponding 3 or 4 positions are set as pores when generating the input file for the numerical simulation.

In the RL environment, the state of concrete structure is represented with a 5×8 matrix. In particular, a position with pore is designated as 1, and 0 otherwise. Afterwards, the matrix is transformed into a 40-dimensional vector to serve as the input state. An action is performed by converting the state from 0 to 1 (matrix to pore) or vice versa.

7.2.2. TARGET REPRESENTATION

The target mechanical property is initially defined as peak load to investigate the RL approach as well as to tune the hyperparameters of the Q-networks. Afterwards, structures are optimized for high self-healing capacity. Self-healing capacity could be optimized from two aspects: (1) the flexural strength of the concrete structure is not significantly decreased; and (2) more pores should be hit by the crack and thereby triggering the healing process, resulting in higher toughness. The calculation of toughness is the same with Equation 6.1 in Chapter 6.

Similar to the input generation, the output file should also be automatically post-processed to obtain the target properties. In addition, the target value should be passed to the RL agent so as to calculate the reward corresponding to the state and action pair. Note that the Python running environment is different for RL agent training (Tensorflow framework), Abaqus running (system environment) and pre-/post- process (Abaqus Python). Therefore, the environment should be shifted during the interaction process.

7.3. MARKOV DECISION PROCESS AND Q-LEARNING

MARKOV Decision Process (MDP) is a mathematically idealized form of RL problems [4]. The agent takes an action based on the perceived state s_t and the state transfers to a new state s_{t+1} . To guide the action, a numerical value R_t is given as reward. The interaction between the agent and the environment continues until the perceived state is the terminal state s_T . MDPs are meant to be straightforward framing of the problem of learning from interaction to achieve a goal. In this study, the agent-environment interaction in a Markov decision process is shown in Figure 7.1.

The aim of RL is to maximize the expected discounted return in an interaction episode, which is called the reward hypothesis. The expected discounted return can be expressed as shown in Equation 7.1.

$$G_t = R_{t+1} + \gamma R_{t+2} + \dots + \gamma^{T-t-1} R_T \quad (7.1)$$

Where γ is discount rate; and T is the final time step.

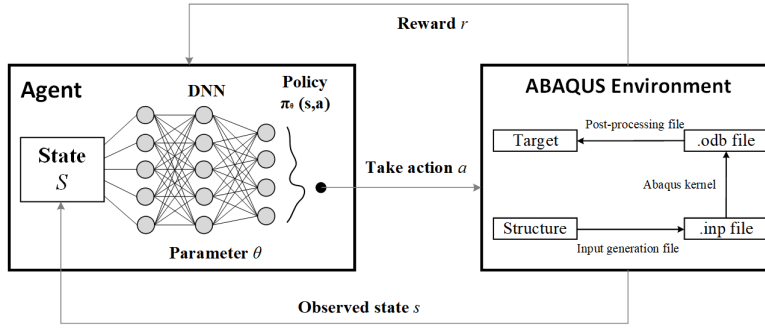


Figure 7.1: Agent-environment interaction in Markov Decision Process (MDP).

Among the RL algorithms, Q-learning is a widely-used off-policy control method due to its capacity to converge to optimal policy even if acting sub-optimally [4]. Watkins was the first to introduce Q-learning, in which the value of a state-action pair is represented by $Q(s, a)$, and the value is based on Equation 7.2.

$$Q(s_t, A_t) \leftarrow Q(s_t, A_t) + \alpha [R_{t+1} + \gamma \max_a Q(s_{t+1}, a) - Q(s_t, A_t)] \quad (7.2)$$

Where α is the learning rate.

The learned action-value function $Q(s, a)$ directly approximates q^* , which is the optimal action-value function. In most cases, a q-table is sufficient to store the action-value pair when using Q-learning. However, a linear form cannot take into account any interactions between features. In this study, a neural network is employed for the nonlinear function approximation. In other words, Q-network is adopted to describe the state-action value. The input is the state s and the output is the parameterized Q function $Q_\theta(s, a)$.

7.4. DEEP Q-LEARNING APPROACH TO OPTIMIZE VASCULAR STRUCTURES

THE optimization target is to design a concrete structure with high flexural strength or toughness (taken as a proxy of the self-healing capacity) under the predefined constraint. The updating strategy is as follows: (1) A concrete structure with 3 pores is randomly generated as the start state s_0 ; (2) One agent (Agent 1) performs an action to decrease the number of pores from 3 to 2 (state transfers from s_t to s'_t); (3) The other agent (Agent 2) performs an action to increase the number of pores from 2 to 3 with (state transfers from s'_t to s_{t+1}); (4) State s_t is updated to state s_{t+1} in step (3) until reaching the terminal state s_T .

The optimization of a 3-pore structure could also be performed via the updating strategy of changing 3 pores to 4 pores, then changing from 4 pores to 3 pores. Importantly, a structure with a different number of pores could be optimized without significantly changing the programming code. Therefore, structures with 3 pores are first investigated with the RL framework. The optimization effectiveness via the

updating strategies of $3 \rightarrow 2 \rightarrow 3$ and $3 \rightarrow 4 \rightarrow 3$ is compared. The two updating strategies for a 3-pore structure optimization are shown in Figure 7.2.

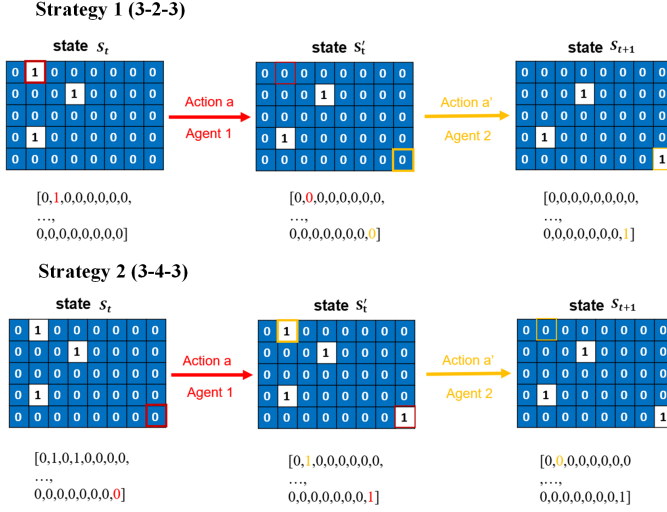


Figure 7.2: Post-processing of ML-recommended input.

Based on [8], an MDP is defined by seven elements, i.e., (1) set of state S ; (2) Set of action A ; (3) Transition function $P(s'|s, a)$; (4) Reward function $R(s', a, s)$; (5) start state s_0 ; (6) Discount factor γ ; (7) Horizon H . According to previous studies [2], the discount factor is set to be 0.95. All other elements are introduced in the following section.

7.4.1. SET OF STATE S AND START STATE s_0

The entire design space comprises all possible structures when there are 3 pores out of the 40 positions in the middle span. Theoretically, there are 9,880 (C_{40}^3) possibilities at most, and each state can be represented by a 40-dimensional vector with 0's and 1's. For updating strategy 1, the transition state is a 2-pore structure, for which there are 780 (C_{40}^2) possibilities.

At the beginning of each episode, we initialize the concrete structure: this is called the start state (s_0). To optimize the concrete structure with less computational burden, the interaction process does not always start from a certain structure. The start state is randomly generated by choosing 3 unique integers in the range between 0 and 39 at the beginning of each episode. The 3 selected positions are encoded as 1's (pores) and the remaining 37 positions are encoded as 0's (matrix) to form a 40-dimensional vector, which is used as the start state.

Similarly, for the updating strategy of $3 \rightarrow 4 \rightarrow 3$, the sets of state and transition state are 9,880 (C_{40}^3 , 3-pore structure) and 91,390 (C_{40}^4 , 4-pore structure), respectively. The start state is also randomly generated at the beginning of each episode.

7.4.2. ACTION FUNCTION AND TRANSITION FUNCTION

Based on the current state s_t , the agent takes actions to maximize the discounted future reward. Herein, actions are taken to convert the 'state' of one position: turn a position from pore to matrix (1→0) or from matrix to pore (0→1). Considering that the agent can only take one action in one interaction with the environment, two agents are created to take two separate actions in a row to maintain the pore number as 3 based on the research of Sui et al [2]. Taking the updating strategy 2 as example: Agent 1 first takes an action a to turn one position from matrix to pore (0→1). To ensure that the pore number changes from 3 to 4, the action should be taken among the 37 matrix positions. Afterwards, Agent 2 takes another action a' to turn one position from pore to matrix (1→0). Similarly, the action a' acts on the 4 positions which are defined as pores. The transition functions are shown in Equation 7.3-7.6 respectively.

For updating strategy 1 (3→2→3):

$$P(s'_t|s_t, a) = \begin{cases} \frac{1}{3}, & \text{pores} \\ 0, & \text{others} \end{cases} \quad (7.3)$$

$$P(s_{t+1}|s'_t, a') = \begin{cases} 0, & \text{pores} \\ \frac{1}{38}, & \text{others} \end{cases} \quad (7.4)$$

For updating strategy 2 (3→4→3):

$$P(s'_t|s_t, a) = \begin{cases} \frac{1}{37}, & \text{matrix} \\ 0, & \text{others} \end{cases} \quad (7.5)$$

$$P(s_{t+1}|s'_t, a') = \begin{cases} 0, & \text{matrix} \\ \frac{1}{4}, & \text{others} \end{cases} \quad (7.6)$$

7.4.3. REWARD FUNCTION

The feedback the agent receives from the environment in response to its action is referred to as a reward. In this study, the reward function is based on the target properties. To optimize structures towards the higher peak load (i.e., higher flexural strength), the change of the peak load before and after taking actions is defined as the reward function. Two actions are taken in a row by the two agents and the reward function when state transfers from s_t to s'_t , s'_t to s_{t+1} are shown in Equations 7.7 and 7.8 respectively.

$$R_1(s'_t|s_t, a) = PL'_t - PL_t \quad (7.7)$$

$$R_1(s_{t+1}|s'_t, a') = PL_{t+1} - PL'_t \quad (7.8)$$

where PL_t , PL'_t and PL_{t+1} are the peak load of the concrete structure at state s_t (3 pores, before action a), state s'_t (2/4 pores, after action a) and state s_{t+1} (3 pores, after action a'), respectively.

Similarly, the reward function is defined as the change of toughness before and after taking actions in order to enhance the vascular arrangement for higher self-healing capacity. The reward functions are shown in Equations 7.9 and 7.10, respectively.

$$R_2(s'_t|s_t, a) = T'_t - T_t \quad (7.9)$$

$$R_2(s_{t+1}|s'_t, a') = T_{t+1} - T'_t \quad (7.10)$$

where T_t , T'_t and T_{t+1} are the toughness of the concrete structure at state s_t (3 pores, before action a), state s'_t (2/4 pores, after action a) and state s_{t+1} (3 pores, after action a'), respectively.

7.4.4. HORIZON

Horizon defines how long the agent interacts with the environment. In this study, the concrete structure optimization task is mapped into a finite MDP and it is an episodic task. Therefore, we should determine when to stop the interaction. Here, two termination criteria are set to stop the interaction process for each episode: (1) the maximum number of steps is 200; (2) the target value (peak load or toughness) exceeds a threshold value.

For an episodic task, it is necessary to set a maximum number of steps for each episode. However, the maximum number of steps is not sufficient for looking for the best structure since the agent is likely to miss better structures that occur during the interaction. In addition, the starting state is randomly generated, and the initial guess may be with high peak load or toughness. As a result, the interaction should be terminated in advance if a concrete structure with high target (flexural strength or toughness) occurs. The historical highest value is set as the threshold value to judge whether an equally good or better structure has been encountered during the training process. The threshold value is initialized as 0 before the interaction, and it is updated with the highest peak load/toughness during the interaction. To increase the exploration of agent, the historical maximum value is multiplied by a factor (<1). Since the computational errors for peak load and toughness are different, the factors for peak load and toughness are tuned separately.

7.4.5. RL AGENT

The agent learns to choose the subsequent actions based on the current state in an attempt to achieve maximum reward. Two agents are created to make two sequential actions in a row to maintain a constant number of pores. Deep Q-network (DQN) is employed to map the state to the action-state pair. The number of neurons of the input and the output layers is set to 40 since the concrete structure is represented with a 40-dimensional vector (section 7.2.1). There are 2 hidden layers with 1,024 and 512 hidden neurons, respectively. For the agent takes action to change 2-pore structures to 3-pore structures, one hidden layer is created with 1,024 neurons considering the limited state ($C_{40}^2=780$) after hyperparameter tuning. The output layer has 40 neurons so that any of the 40 locations can be selected. The loss function and activation

function are chosen as Huber loss and ReLu function. The used DQN is schematically presented in Figure 7.3.

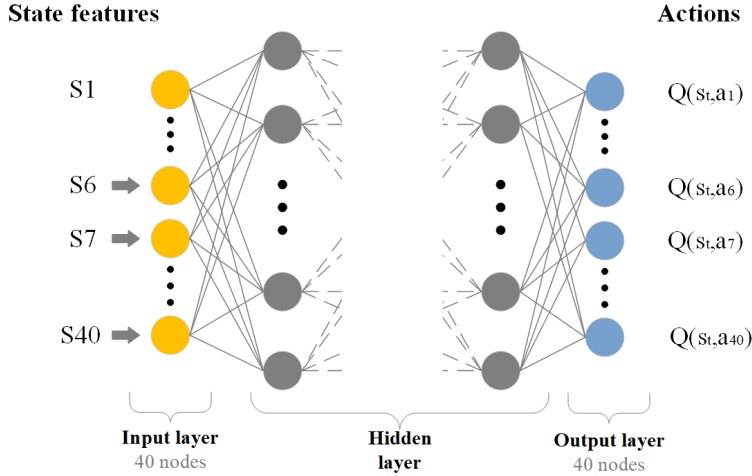


Figure 7.3: Schematic illustration of DQN.

During the learning process, the weights (θ) of the deep Q-network are updated instead of directly updating the Q-value. The updating logics are given in Equation 7.11 and 7.12.

$$target(s') = R(s, a, s') + \gamma \max_{a'} Q_{\theta_k}(s', a') \quad (7.11)$$

$$\theta_{k+1} \leftarrow \theta_k - \alpha \nabla_{\theta} \left[\frac{1}{2} (Q_{\theta}(s, a) - target(s'))^2 \right] |_{\theta=\theta_k} \quad (7.12)$$

Considering that function approximation with neural network faces possible instabilities or even divergence [9], two heuristics, i.e., experience replay and target Q-network, are employed to fix this problem. They could help disconnect the data correlation and increase the learning efficiency. The replay buffer is 64, and the update target frequency is 10, and the batch-size is 16. Tensorflow framework is adopted for the coding and the training process.

7.5. 3-PORE CONCRETE STRUCTURE OPTIMIZATION FOR MAXIMUM PEAK LOAD

To test the feasibility of vascular structure optimization using the RL approach, SHC with 3 pores are first enhanced aiming to mitigate the influence of pores on flexural strength. The optimization process is run independently for multiple times to investigate the average behavior of the learning algorithm.

7.5.1. THE OPTIMIZED STRUCTURE AND FREQUENCY

Considering that the goal is to search a concrete structure with the maximum peak load, the historical maximum peak load is recorded during the interaction process. Both updating strategies are employed and compared with respect to the percentage of the best structures (Figure 7.4(a) and 7.4(b)). In addition, the displacement-load curves of the optimized structures are illustrated in Figure 7.4(c) and 7.4(d).

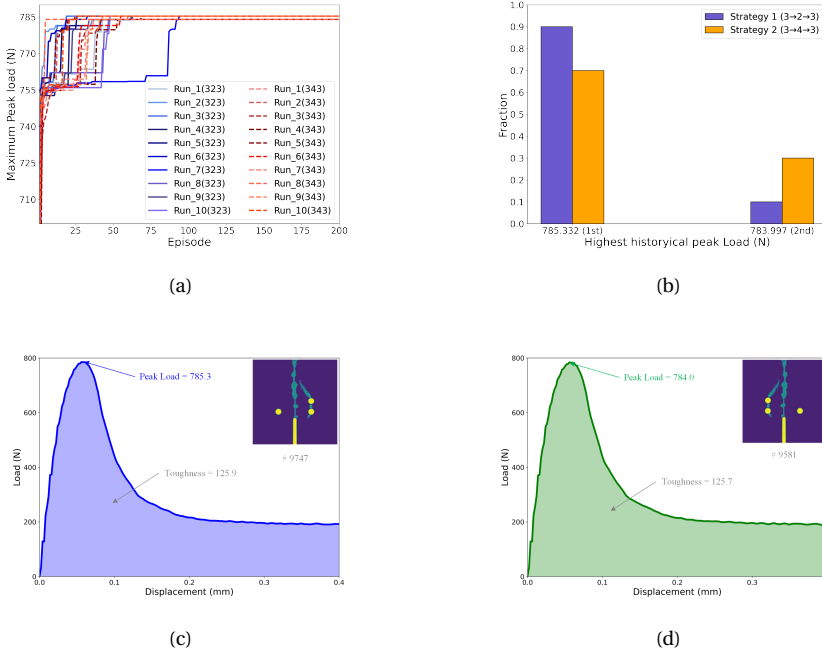


Figure 7.4: Optimization result of 3-pore structure towards high peak load. (a) Historical best structure during the interaction process; (b) Fraction of the best historical structures; (c) Structure with a peak load of 785.3N; (d) Structure with a peak load of 784.0N.

For both updating strategies, there are two optimal structures with peak loads of 785.3N and 784.0N (See Figure 7.4(a) and 7.4(b)). During the 20 independent runs (10 runs for each updating strategy), the final two structures are encountered before the episode number 100 in most runs. In the whole design space, the maximum peak load of a 3-pore structure determined by the Abaqus model is 785.3N, which has been identified in 16 out of the 20 optimization runs. The remaining 4 runs identify a structure with a peak load of 784.0N, which is ranked as the second highest in the whole design space. As shown in Figure 7.4(b), the percentage of runs which successfully identified the best structure (peak load=785.3N) through updating strategy 1 (3→4→3) is higher than that of updating strategy 2 (3→2→3).

When looking into the corresponding optimal structures, it is found that those two structures are symmetric (see Figure 7.4(c) and 7.4(d)). The main crack does not hit pores in either of the two structures, which explains why these structures have a high peak

load. Note, however, that this is not optimal for self-healing: in these cases, no vascular networks would have been activated, and no self-healing would have been possible. In theory, the peak load of symmetric structures should be identical; the slight difference between the two structures (0.16%) is a result of a simulation error. Therefore, it could be concluded that the optimization algorithm successfully identified the structure with the highest peak load in all 20 runs.

7.5.2. NUMBER OF VISITED STRUCTURES DURING INTERACTION

The total number of visited structures can reflect the number of interactions as well as the convergence of Q-networks. More importantly, more computation time is used if more unique structures are visited. Therefore, the number of visited 3-pore structures is recorded (Figure 7.5).

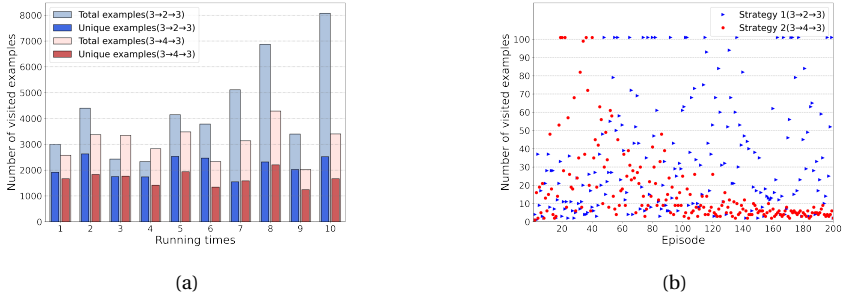


Figure 7.5: Number of visited structures. (a) Number of visited structures in different runs; (b) Number of visited examples in Run 8.

As shown in Figure 7.5(a), the total number of visited 3-pore structures is dramatically different between the two updating strategies. Except for the random initialization of the start state, this may be also caused by the high probability of exploration since the exploration rate decays from 1 with a decay rate of 0.995 in each episode. Exploration enables the RL agent to get rid of suboptimal actions. The average numbers of total visited 3-pore structures with the updating strategy 1 and 2 are 4,355 and 3,078, which are much less than 20,000 (maximum number of visited 3-pore structures). In other words, the interaction process in most of the runs stops before reaching the maximum number of steps (i.e., 200 steps). This can also be verified by Figure 7.5(b), where the number of visited 3-pore structures in most episodes is less than 100. As a result, the small number of totally visited structure decreases the training time of RL agent.

Compared with the time spent on training Q-networks, the simulation time (i.e., time for running Abaqus models) accounts for most of the training time in this study. The simulation time increases only when new structures are encountered since the target properties of previous structures could be directly accessed. For a reinforcement learning task, it is common that one structure (including the best structure) is visited multiple times during the interaction process. Therefore, the number of visited unique

structures is also recorded to investigate the computation burden. According to Figure 7.5(a), the number of visited unique 3-pore structures is much lower than the total number of visited structures. The average numbers of visited unique structure with the two update strategies are 2,143 and 1,666 respectively. Therefore, the RL agent manages to find the best structure by visiting 22% of the complete dataset. Compared with the updating strategy 1, the other strategy is more efficient since less computational power is needed. The advantage of an RL agent will be more pronounced as the design space increases.

7.5.3. CHANGE OF AVERAGE REWARD

The increase in expected reward with experience is another important parameter that measures the average behavior of the learning algorithm. The average reward of the 10 independent runs for the two updating strategies is shown in Figure 7.6.

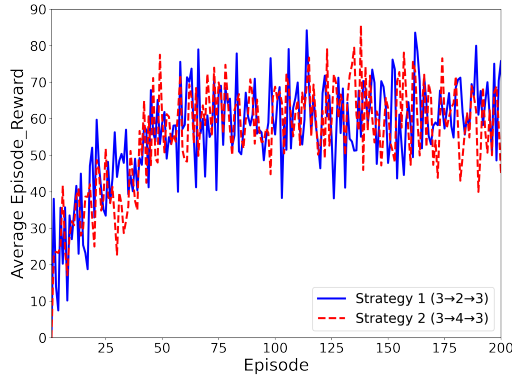


Figure 7.6: Average reward of structure optimization for high peak load.

From Figure 7.6, it can be seen that the average reward fluctuates due to the noisy reward, which is set as the change of the peak load of 3-pore structure before/after the actions. For the two updating strategies, the average reward gradually improves before episode 70. Afterwards, the average reward levels off at the reward of about 60N. Compared with the first terminal condition, the second terminal condition greatly influences the average reward. The target value of the historically best structure is relatively low at the beginning, where an equally good or better structure is encountered easily at the beginning. However, the threshold value increases with an increasing number of visited structures. Although the RL agent is trained to take right actions to maximize the reward, it is possible that the interaction cannot find an equally good or better structure within 200 steps. As a result, the average reward gradually increases and then remains steady.

7.5.4. LOSS FUNCTION OF THE TWO Q-NETWORKS

To evaluate the performance of two RL agents, it is necessary to investigate the change of loss functions as training progresses. The loss functions of the two Q-networks in one run is shown in Figure 7.7.

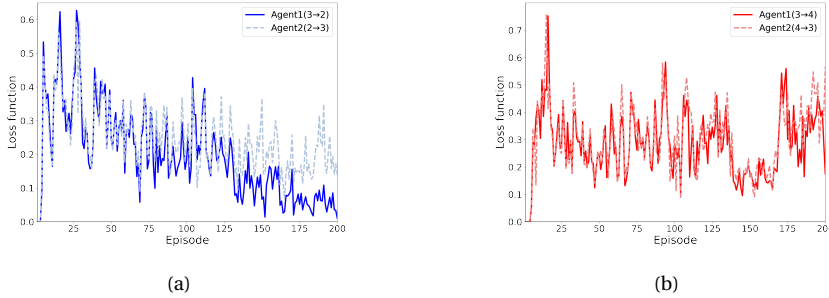


Figure 7.7: Loss functions of two Q-networks of structure optimization for high peak load with (a) Updating strategy 1; (b) Updating strategy 2.

For updating strategy 1, the loss functions of the two Q-networks decrease with the episode even though they fluctuate during the training process (see Figure 7.7(a)). Due to the limited number of visited examples (restricted by terminal criterion 2) in the beginning, the loss functions remain 0 for both agents. This can also be observed in updating strategy 2 (see Figure 7.7(b)). Compared with Agent 1, the loss function of Agent 2 starts increasing at the last stage of training process. The possible reason is visiting the repetitive examples.

As to updating strategy 2, the loss functions of the two agents show similar trends during the training process. The loss functions gradually decrease before episode 50, then keep fluctuating until episode 130. A clear decrease can be seen around the episode 150. At the last stage of the training process, the loss functions of the two agents increase again. Compared with updating strategy 1, the two Q-networks are deeper and therefore more likely to suffer from overfitting with repetitive examples. Note, however, that the loss functions do not influence the search for the best structures according to the results in section 7.5.1.

7.6. 3-PORE CONCRETE STRUCTURE OPTIMIZATION FOR MAXIMUM TOUGHNESS

7.6.1. THE OPTIMIZED STRUCTURE AND FREQUENCY

IN section 7.5, it is shown that the vascular concrete can be optimized for maximum peak load (i.e., flexural strength). However, as stated, this is not optimal for self-healing. To design a vascular structure with more pores hit by the crack, in this section toughness is set as the target property. The results are shown in Figure 7.8.

As shown in Figure 7.8, two 3-pore structures with the toughness of 136.0N·mm and 134.6N·mm are found in the 20 runs. The performance of updating strategy 2 is better,

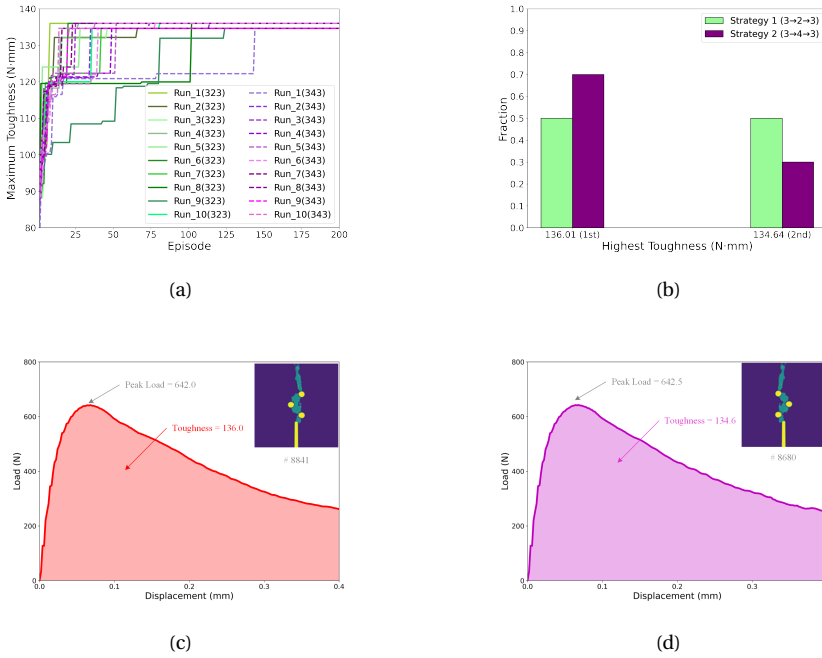


Figure 7.8: Optimization result of 3-pore structure for maximum toughness (a) historical best structure during the interaction process (b) Fraction of the best historical structures; (c) Structure with a toughness of 136.0N-mm; (d) Structure with a toughness of 134.6N-mm.

since 70% of the runs end with the structure with higher toughness. According to the whole dataset, the highest toughness of 3-pore structure from numerical simulation is 136.0N-mm. However, considering that the two best structures are symmetric, it could be concluded that the best structure is identified in all of the runs. Compared with the peak load, the computation error of toughness for the two symmetric structures is larger (1.03%). This is caused by the truncation error when calculating toughness (until maximum displacement of 0.4mm). Compared with the peak load optimization, the final two structures are encountered after the episode number 100 in most runs. Therefore, it is necessary to set the maximum step to be 200 when optimizing concrete structure towards high toughness.

7.6.2. NUMBER OF VISITED STRUCTURES DURING INTERACTION

Similarly, the numbers of visited structures in the 20 runs are recorded to study the training time as well as the convergence. The results are shown in Figure 7.9(a). In addition, the number of visited structures in one episode is shown in Figure 7.9(b).

Compared with the peak load, the numbers of total visited structures is much larger, showing that it is more difficult for the RL agent to converge when optimizing for high toughness. Furthermore, the large number of visited unique structures requires more

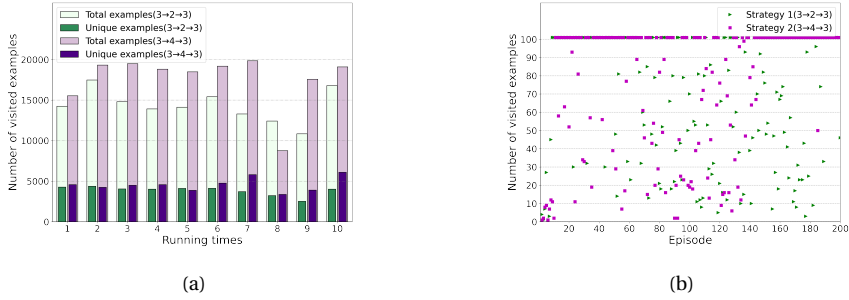


Figure 7.9: Number of visited structure (a) Number of visited structures in different runs; (b) Number of visited examples in Run 1.

computational time during the interaction process.

The performance of updating strategy 1 is better than that of updating strategy 2. For updating strategy 1 ($3 \rightarrow 2 \rightarrow 3$), the numbers of total visited and unique 3-pore structures are 14,329 and 3,843, respectively, which are lower than that of updating strategy 2 (17,609 and 4,570, respectively). From Figure 7.9(b), it can be seen that the interactions in most of the episodes is terminated by the maximum step criterion when using update strategy 2.

7.6.3. CHANGE OF AVERAGE REWARD

The average reward of the 20 independent runs for the two updating strategies is shown in Figure 7.10.

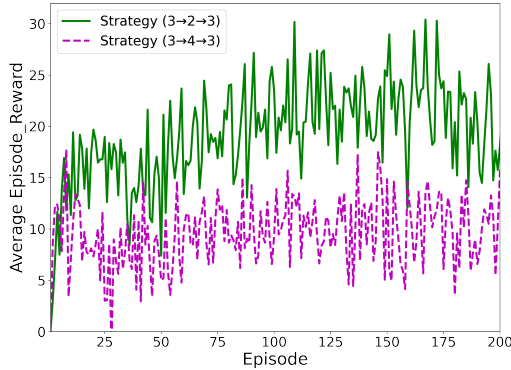


Figure 7.10: Average reward of structure optimization for higher toughness over 20 runs.

From Figure 7.10, the average reward also fluctuates for the two update strategies. The average reward of updating strategy 1 is significantly higher than that of updating

strategy 2. For updating strategy 1, the average reward gradually improves at the beginning and then remains steady with an average reward of about 25N·mm after episode 100. However, the average reward of updating strategy 2 sees a significant increase at the beginning, but it increases and remains unchanged in the following training process. The average reward of strategy 2 is less than 10N·mm. Therefore, updating strategy 1 is recommended for optimizing the 4-pore structures for high self-healing capacity in the following part.

7.6.4. LOSS FUNCTION OF THE TWO Q-NETWORKS

Similarly, the loss functions of two Q-networks in one run are shown in Figure 7.11.

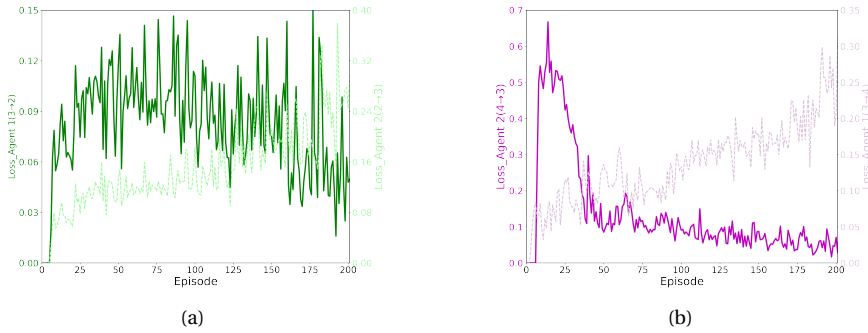


Figure 7.11: Loss functions of two Q-networks of structure optimization for maximum toughness with (a) Updating strategy 1; (b) Updating strategy 2.

It is shown in Figure 7.11 that the average loss functions also fluctuate for the two update strategies. Loss functions of the two Q-networks show different trends. The loss functions of Q-network turning matrix to pore (agent 2 for updating strategy 1, agent 1 for updating strategy 2) increases as the episodes pass. Compared with updating strategy 1, the loss function of agent 2 (4→3) dramatically decreases at the first 50 episodes and then gradually decreases in the remaining episodes. The loss function of agent 1 in updating strategy 1 first increases and then gradually decreases. The loss functions also prove that it is more difficult for the RL agent to converge when optimizing concrete for high toughness compared with optimization for high peak load.

7.7. APPLICATION TO A NEW OPTIMIZATION PROBLEM

Based on the results above, vascular optimization towards good self-healing capacity (i.e., toughness) through RL approach is performed for 4-pore concrete structures. The set of state is 91,380, which would make it time consuming to optimize by brute force. Considering that the performance of updating strategy 1 is better than updating strategy 2 in section 7.6, the updating strategy for 4-pore structure optimization is chosen as 4→3→4. The two Q-networks consist of 2 hidden layers with 1,024 and 512 neurons in each layer. The result of 4-pore structure optimization for toughness is shown in Figure 7.12.

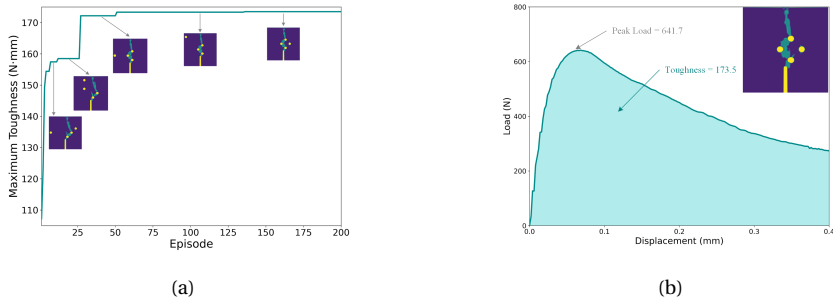


Figure 7.12: Optimization result of 4-pore structure towards higher toughness (a) Historical best structure during the interaction process; (b) Structure with highest toughness.

As shown in Figure 7.12, the optimized 4-pore vascular structure has a toughness of 173.5N-mm, which is higher than the highest toughness of 3-pores. When looking at the historical best structure in the optimization process (Figure 7.12(a)), great improvement of toughness occurs at the episode 27, where 3 of the 4 pores are the same with the 3-pore structure with the highest toughness. In the following episodes, the 4th pore changes at the episodes of 51 and 136, and ends up with the position of 29. Compared with other structures, the 4th pore of the final optimized structure is the closest to the other 3 pores. As a result, the toughness of the final structure is higher than the other structures.

The number of the total visited structures and unique visited structures are 18,902 and 12,392 respectively. Considering that there are 91,390 combinations of 4-pore structures, the interaction visits 13.6% of the complete dataset. As a result, it is feasible to arrange the vascular configuration of concrete using the RL approach.

7.8. CONCLUSIONS

IN this chapter, an automatic optimization method is proposed to arrange the vascular configuration of vascular SHC through RL approach. A Markov Decision Process (MDP) is first formed and its elements are defined. To assess the viability of utilizing the method for vascular arrangement, SHC with 3 pores is first enhanced for higher peak load or toughness with two update strategies. Subsequently, vascular structure of a 4-pore concrete is optimized for good self-healing capacity by setting toughness as the target property. The main conclusions are as follows:

- The proposed method is capable of automatically enhancing the vascular configuration of concrete for different target properties through the interaction between the RL agent and the Abaqus simulation environment. The optimization process is influenced by the design constraint, target properties and updating strategies.
- Considering the symmetry of structures, the structure with highest peak load of 3-pore concrete structures is accessed in all 20 independent runs through two updating strategies. The change trends of average reward for the two updating

strategies are similar during the training process. However, updating strategy 2 ($3 \rightarrow 4 \rightarrow 3$) outperforms strategy 1 ($3 \rightarrow 2 \rightarrow 3$) since the average number of unique visited structure is lower, which saves computational time.

- The 3-pore structure with the highest toughness is also visited in all 20 independent runs. However, the loss functions of RL agents taking action to increase the pore number dramatically increase as the episode increases. For both updating strategies, the numbers of total visited and unique visited structures are much larger than those of the peak load optimization of 3-pore structures. Therefore, it is more difficult for the RL agent to converge when optimizing concrete for high toughness.
- When optimizing a 3-pore structure towards high toughness, the optimization performance of updating strategy 1 is better since the number of unique visited structures is smaller and it is time-efficient. Besides, the average reward of strategy 1 is higher.
- The RL optimization method is able to identify the structure with high toughness in the new optimization task for 4-pore concrete structure. As such, the method can be a powerful tool to automatically optimize structure towards higher target property.

REFERENCES

- [1] N. K. Brown, A. P. Garland, G. M. Fadel, and G. Li, *Deep reinforcement learning for engineering design through topology optimization of elementally discretized design domains*, *Materials & Design* **218**, 110672 (2022).
- [2] F. Sui, R. Guo, Z. Zhang, G. X. Gu, and L. Lin, *Deep reinforcement learning for digital materials design*, *ACS Materials Letters* **3**, 1433 (2021).
- [3] C. Qiu, S. Du, and J. Yang, *A deep learning approach for efficient topology optimization based on the element removal strategy*, *Materials & Design* **212**, 110179 (2021).
- [4] R. S. Sutton and A. G. Barto, *Reinforcement learning: An introduction* (MIT press, 2018).
- [5] Z. Jinshi and H. Jiazhen, *Coordination mechanism combining supply chain optimization and rule in exchange*, *Asia-Pacific Journal of Operational Research* **30**, 5_1 (2013).
- [6] T. Kim, Y.-W. Kim, D. Lee, and M. Kim, *Reinforcement learning approach to scheduling of precast concrete production*, *Journal of Cleaner Production* **336**, 130419 (2022).
- [7] V. Mnih, K. Kavukcuoglu, D. Silver, A. A. Rusu, J. Veness, M. G. Bellemare, A. Graves, M. Riedmiller, A. K. Fidjeland, G. Ostrovski, *et al.*, *Human-level control through deep reinforcement learning*, *nature* **518**, 529 (2015).
- [8] A. Nair, B. McGrew, M. Andrychowicz, W. Zaremba, and P. Abbeel, *Overcoming exploration in reinforcement learning with demonstrations*, in *2018 IEEE international conference on robotics and automation (ICRA)* (IEEE, 2018) pp. 6292–6299.
- [9] J. Tsitsiklis and B. Van Roy, *Analysis of temporal-difference learning with function approximation*, *Advances in neural information processing systems* **9** (1996).

8

DIRECT INK WRITING OF VASCULARIZED SELF-HEALING CEMENTITIOUS MATERIALS

Direct ink writing of cementitious materials can be an alternative way for creating vascular self-healing concrete by intentionally incorporating hollow channels in the cementitious matrix to act as a 'vascular network'. In this chapter, a 3D-printable fiber reinforced mortar was first developed. Three groups of specimens were fabricated using direct ink writing, where the two top and bottom printing layers were printed with different printing directions. The microstructure of the hardened specimens was studied using CT scanning. The results from CT scanning show that printing direction influences the actual volumes of hollow channels and the volume of small pores which are a consequence of the deposition process. The hollow channels in all samples were squeezed by the layers above during the printing process, and the longitudinally printed samples were the most affected. When printing direction changes from longitudinal to transverse, the initial flexural strength decreases. Similarly, the average permeability of the cracked samples increases when the printing direction changes from longitudinal to transverse. Although the healing effectiveness regarding flexural strength is over 100% for all specimens, it was only possible to perform a single healing process as hollow channels were then blocked by the epoxy resin. We believe that the rough surface of the hollow channels makes it difficult to extract the epoxy resin out of the specimens with pressurized air.

8.1. INTRODUCTION

ALTHOUGH 3D hollow channels were successfully created in Chapter 4, this process of fabrication and dissolution of the 3D-printed PVA vascular network is labor-intensive. Furthermore, the 3D-printed vascular is relatively small, making its upscaling to large-scale structures non-trivial. Direct ink writing of cementitious materials can be an alternative way for creating vascular self-healing concrete [2–5]. For self-healing concrete, hollow channels could be intentionally incorporated in the cementitious structures to act as the ‘vascular network’. However, to the best of the authors’ knowledge, there have been no attempts to achieving this. In direct ink writing of cementitious materials, printing direction influences the printing quality as well as the interlayer bond [6]. More importantly, the reserved hollow channels may be squeezed during the printing process. As a result, the actual volume of the hollow channels may be different when different printing directions are used.

In this chapter, a fiber reinforced mortar with hollow channels is additively manufactured as vascular self-healing cementitious material. First, a 3D-printable fiber reinforced mortar was designed as the printing ink. Prisms with 3D hollow channels were printed with three printing directions (longitudinal, inclined and transverse). The printed samples were examined using X-Ray computed tomography (CT scanning) after hardening to investigate the influence of printing direction on the structures of hollow channels. The flexural strengths under 4-point bending of the virgin samples were tested first. Then, a water permeability test was carried out on the cracked samples. Afterwards, epoxy resin was injected as the healing agent to heal the cracked samples. The healing performance regarding the flexural strength regain and the water permeability is compared and discussed.

8.2. MATERIALS AND SETUPS

8.2.1. MIX DESIGN OF A 3D PRINTABLE MORTAR

HEREIN, a mix design of the 3D-printable mortar presented. The material for 3D printing needs to have good pumpability and buildability [7, 8]. A low water/cement ratio should ensure the stiffness and the strength of the extruded materials for good buildability [9]. However, low water/cement ratio could cause problems for the pumpability of the materials. Therefore, superplasticizer (Glenium 51) is added to improve the fluidity of the cementitious material. In addition, hydroxypropyl methylcellulose-based viscosity modifying admixture (VMA) is added to improve the cohesion and consistency of the fresh mixture [10, 11]. After a series of trial-and-error tests, the water/cement ratio is determined as 0.343.

To avoid brittle failure of specimens during mechanical tests, ultra-high molecular weight polyethylene fiber (UHMWPE) is incorporated into the cementitious matrix to enhance the ductility. The properties of UHMWPE could be seen in Table 4.3. However, it has been shown that a large percentage of fibers may introduce air voids and fiber balls during the printing process [7]. Based on Chapter 4, 0.17 vol% of PE fiber is added to the printing mix. The mix design of the mortar is given in Table 8.1.

Table 8.1: Mix design of the 3D printable mortar (kg/m^3).

Cement III B 42.5	Water	Sand (0.125-0.25mm)	Superplasticizer (Glenium 51)	VMA	UHMWPE
1385.1	474.7	117.0	0.28	1.1	1.7

8.2.2. RHEOLOGICAL PROPERTY OF THE DESIGNED MIXTURE

An Anton Paar MCR 302e rheometer was used to determine the flow properties of the proposed mixture [12]. For each measurement, 85–90g of fresh paste was filled into the measuring cup. Note that time zero is defined as the moment when water is added to the dry components during mixing. After a pre-shear ($60s^{-1}$ of shear rate and 30s of duration time) and resting session (30s), the flow curve test was executed at the material age of 5min. The shear rate ramped linearly from $0s^{-1}$ to $30s^{-1}$ within 1min and was maintained at $30s^{-1}$ for 40s. After that, the shear rate was decreased in four consecutive steps from $30s^{-1}$ to $10s^{-1}$ and was kept constant at about 40s for each step. The data was recorded each 0.2s. A detailed test protocol is presented in Figure 8.1(a). For each shear rate regime in the descending part, the shear stress was averaged by using the final 50 measuring points. The flow curve is shown in Figure 8.1(b). For the fresh cementitious materials, the Herschel-Bulkley (HB) model (Equation 8.1) is often used to describe the rheological behavior [13]. Note that the model is identical to Bingham model when the exponent is 1.

$$\tau = \tau'_0 + k\dot{\gamma}^n \quad (8.1)$$

Where τ'_0 is the dynamic yield stress; k and n are consistency factor and power index, respectively.

After the flow curve test and 5min of resting, a constant shear rate (CSR) test was used to measure the static yield stress at the material age of 15min. In CSR test, the applied shear rate is $0.1s^{-1}$ and the testing time was 40s. This test was also performed at material age of 30, 45 and 60min and the resting time between two tests was about 14min. As shown in Figure 8.1(c), the peak value of shear stress with a small constant shear rate could be seen as static yield stress (SYS) [14].

As shown in Figure 8.1(b), the shear stress-shear rate curve could be well fitted with the Herschel-Bulkley model. For this mixture, the value of τ'_0 , k and n are 1235.38, 0.3555 and 2, respectively. Since the fitted component is 2, the designed mortar cannot be employed in a printing process with a high shear/extrusion because the shear thickening behavior would make the apparent viscosity become too high for the mix to be pump and extruded. The static yield stress of the mix can be found in Figure 8.1(c). While the static yield stress increases with time, the speed of increase gradually decreases.

8.2.3. DESIGN OF THE VASCULAR NETWORK

For simplicity, rectangular cross sections are used to form the networks. The joint angle of the second and third generation of vascular network are chosen as 90° (Figure 8.2).

As shown in Figure 8.2(a), the first and second generations of the vascular network

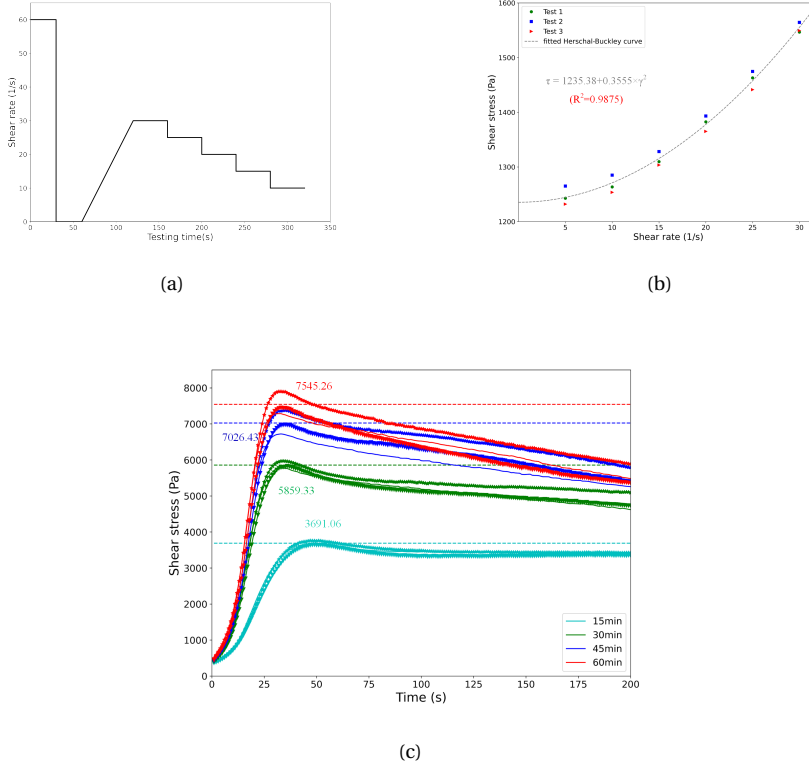


Figure 8.1: (a) Testing protocol of flow curve; (b) Flow curve; (c) Shear stress under constant shear rate.

have the same height for ease of printing. Furthermore, the width of the second and third generations of vascular is identical. Although the cross section is rectangular, one side length in each generation of vascular network is designed based on Murray's law (Equation 2.2) to minimize the flow energy of the healing agents [15]. Considering the dimension of the printing table and the printing time, the dimension of the printed mortar is designed as 200mm (length) \times 50mm (width) \times 32.5mm (height). Note that the positions of vasculature measured from the printing bed (bottom vasculature: 5mm; middle vasculature: 10mm; upper vasculature: 17.5mm) are chosen in accordance with the printing layer-height (2.5mm). This is described in more detail in Figure 8.4. The volumes of the designed cementitious matrix and hollow channels (i.e., vascular network) are 302.18cm^3 and 22.82cm^3 , respectively. The 3D model is designed using Auto CAD, and the slicing is carried out with Matlab software. The actual volumes of matrix and hollow channels with different printing directions will be calculated based on the CT scanning results in Section 8.4.

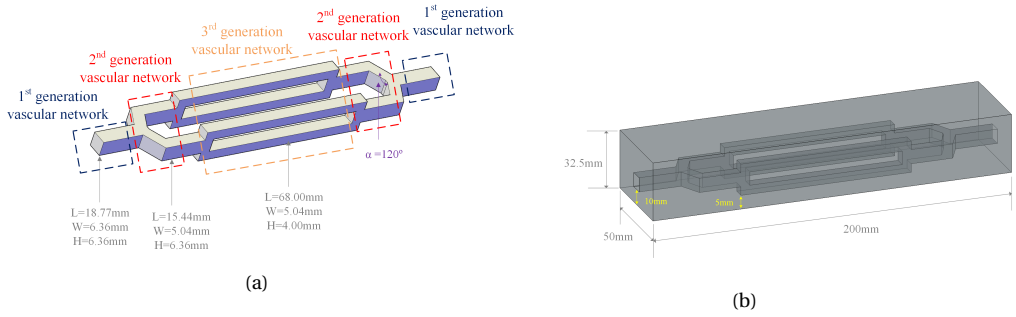


Figure 8.2: Schematic of the 3D-printed mortar with hollow channels. (a) Vascular network; (b) Mortar with vascular networks.

8.2.4. PRINTING PROCESS

An extrusion-based commercial 3D printer (Stone Flower 3.1 Multi-material 3D printer) was used for printing (see Figure 8.3). As shown in Figure 8.3, a ram extruder, consisting of electrical machinery, a steel bar and a piston, is fixed on a gantry. The prepared printing material is stored in the cylinder with a maximum volume of 1.5L [9]. The printing table has dimensions of 480mm (length)×480mm (width)×500mm (height). After the printing file is imported to the 3D printer, operations could be performed through the touch screen of the control system. During the printing process, all relevant information (e.g., printing time and printing speed) is displayed on the screen. A nozzle with a 4mm diameter was used. The rotor above the nozzle helps remove the bubbles from the printing materials before extrusion.

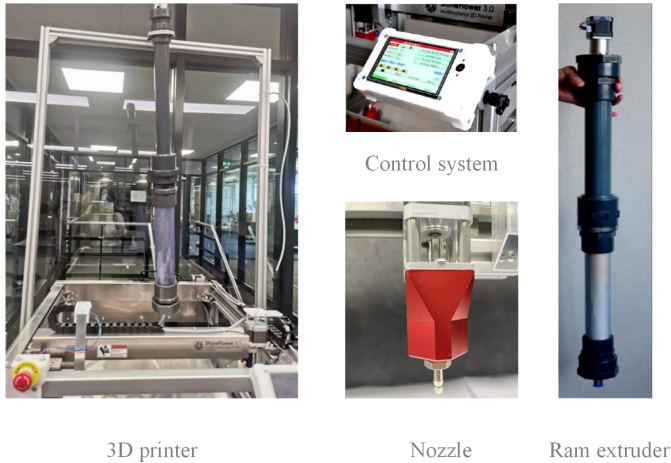


Figure 8.3: The Stone Flower 3.1 Multi-material 3D printer and its components.

Before printing, the fiber reinforced mortar was mixed as follows: (1) The dry

components (cement, sand and VMA) were pre-mixed in a Hobert mixer for 4min; (2) Water and superplasticizer were added to the dry components and mixed for 4min; (3) Fibers were added and mixed for 4min. The mixed mortar was then filled in the cylinder of 3D printer.

The printing layer-height is set as 2.5mm. As a result, thirteen layers are needed in the height direction to print the designed samples. It has been shown that the mechanical behavior of 3D-printed materials is influenced by printing direction [6]. To investigate the influence of printing directions, different variants have been used for the bottom and top 2 printing layers: longitudinal (0°), inclined (45°) and transverse (90°); the remaining layers have been transversely printed to minimize the cantilevered length of the layers above the hollow channels. The printing speed is set as 10mm/s, and the movement speed is set as 20mm/s when changing the printing layer in the height direction. The inflow velocity of mortar is 60cm/min and it takes approximately 45min for the entire printing process. The schematics of different paths are shown in Figure 8.4.

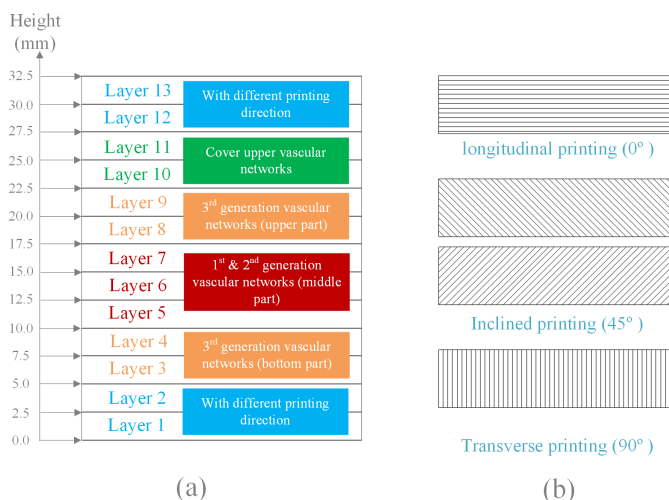


Figure 8.4: Schematic description of (a) Printing layers; and (b) Printing direction.

After determining the printing parameters, one specimen was printed to test the pumpability and buildability of the mix design (Figure 8.5). From Figure 8.5, it is obvious that the designed mortar is suitable for 3D printing since the printing quality of the samples is excellent with very limited visible imperfections between the interlayers.

8.2.5. CURING AND HEALING PROCESS

After printing, the samples were kept on the printing table for 24h covered with plastic film to mitigate water evaporation. Afterwards, the hardened specimens were moved to a curing room where the relative humidity and temperature are kept as $96\pm 2\%$ and $20\pm 2^\circ\text{C}$, respectively. They were cured for 28 days before the first round of mechanical testing. The mechanical properties of the printed samples at 28 days will be compared with the cast counterparts in future research.

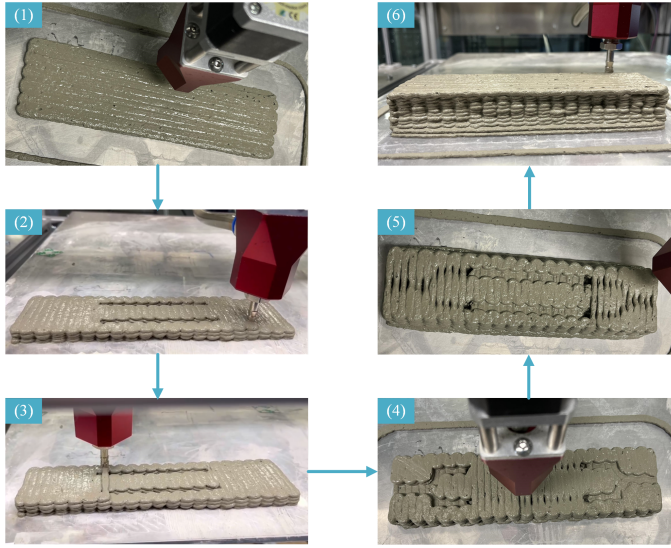


Figure 8.5: Printing process of mortar with hollow channels as vascular networks (longitudinal printing path).

After the mechanical test, the cracked samples were injected with a two-component epoxy resin (Conpox Resin BY 158 and Conpox Hardener BY 2996 supplied by Condor Kemi A/S). According to [16], epoxy resin shows a remarkable performance as the healing agent. We have used the same healing process in Chapter 4: (i) Epoxy resin is manually injected into the cracked samples through one inlet while the other inlet is blocked with a clip; (ii) Pressurized air is injected to blow the extra epoxy resin out of the hollow channels for the reuse of hollow channels after 30min. The amount of epoxy resin is kept as 30ml considering the volume of designed hollow channels (22.82ml). The injected samples were kept in room temperature for 24h until the next round of mechanical tests.

8.3. CHARACTERIZATION METHODS

8.3.1. CT SCANNING

A CT scanner (TESCAN CoreTOM) was used to observe the influence of the printing direction on the printing quality of the samples before the mechanical tests. the actual volumes of the cementitious matrix, hollow channels and small pores are compared with the designs and discussed. The structures were reconstructed using the Dragonfly software. The resolution of the scanned slice is $75\mu\text{m}$. One specimen was scanned for each designed printing parameter.

8.3.2. 4-POINT BENDING TEST

The fracture behavior of virgin samples printed in different directions was studied using a servo-hydraulic press (INSTRON 8872). These specimens were loaded with a constant crack opening speed of $0.5\mu\text{m/s}$ until the crack width reached $450\mu\text{m}$ [17]. Considering

that the crack is likely to develop in the weak inter-layer of the printed samples, there is only one crack during the 4-point bending test. The change of crack width was monitored with a Linear Variable Differential Transformer (LVDT) on the bottom surface of the samples. In this study, the LVDTs go across the whole midsection of the specimen (i.e., between the loading points), where the cracks will surely occur. The crack width was recorded until the samples were completely unloaded. The 4-point bending test is shown schematically in Figure 8.6. Two specimens per group were tested.

For the healed samples, another 4-point bending test was carried out to evaluate the mechanical response of the samples after injecting the healing agent (epoxy resin). The healed samples were reloaded to $500\mu\text{m}$ with a crack opening speed of $0.5\mu\text{m/s}$.

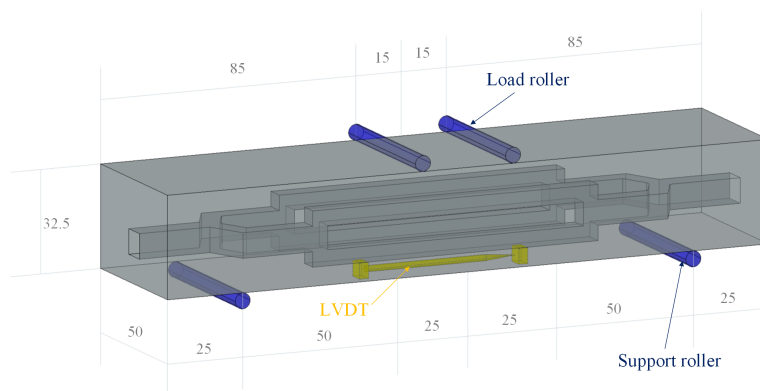


Figure 8.6: Schematic of 4-point bending test.

8

8.3.3. WATER PERMEABILITY TEST

Water permeability of the cracked samples was measured and compared. Water permeability of the samples before and after healing can be used to evaluate the sealing efficacy in terms of watertightness [17]. More detailed information is given in chapter 4. In addition, the water permeability of the cracked specimens could reflect the healing capacity of the samples: the cracked specimens with larger permeability tend to have greater self-healing potentials compared with the ones with smaller permeability in that the higher permeability allows more healing agents to enter the cracks.

8.4. MACROSTRUCTURE OF SAMPLES WITH DIFFERENT PRINTING DIRECTIONS

8.4.1. INFLUENCE OF PRINTING DIRECTION ON THE HOLLOW CHANNELS

As mentioned above, the reserved hollow channels would be squeezed by the upper printing layer during the printing process. The influence of printing direction on the actual volumes of the cementitious matrix and hollow channels is investigated and the reconstructed CT results are shown in Figure 8.7.

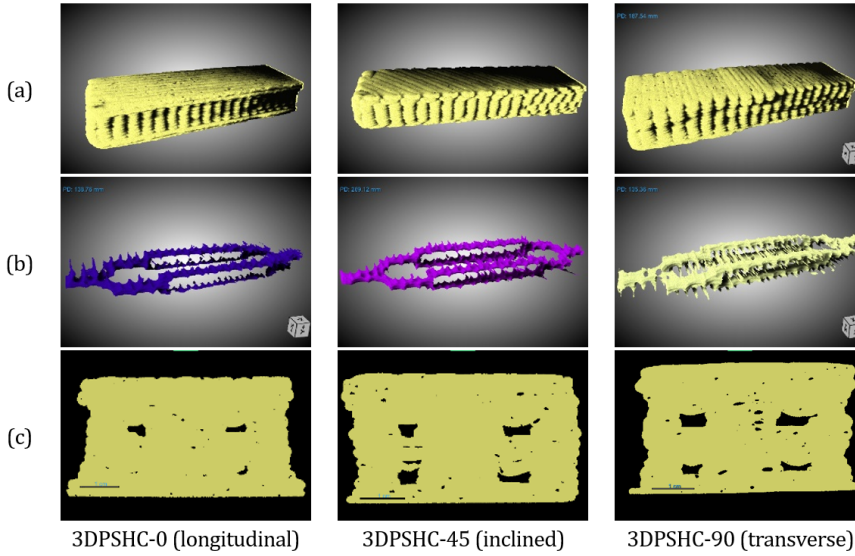


Figure 8.7: Reconstructed CT scan results of 3D-printed mortar with hollow channels. (a) The scanned whole samples; (b) The reconstructed hollow channels; (c) Cross sections in the middle part.

As shown in Figure 8.7, the shapes of actual hollow channels are different from the designed one. Instead of the rectangular cross section in each generation of the vascular network, the hollow channels are irregular, which is caused by two reasons: (1) the hollow channels are squeezed by the self-weight of the layers above; and (2) the imperfections occurring between the printed layers induce additional hollow channels. There are more additional hollow channels in the transversely printed sample than in the other cases. A possible reason is that the interlayers are aligned from bottom layer to top layer, so the interlayers are always in the same places. Compared with transversely and inclined printed specimens, the hollow channels of the longitudinally printed sample are less continuous, which may influence the transport of healing agents during the healing process. To quantitatively investigate whether the influence of printing direction on the vascular network is different, the ratios between actual and designed volume of matrix and hollow channels are given in Figure 8.8.

The actual volumes of hollow channels in the three groups decrease by more than 40% of the designed hollow channel (Figure 8.8). When the printing direction changes from longitudinal (0°) to transverse (90°), the volume of the cementitious matrix and hollow channels show a decrease and an increase, respectively. Although the printing direction influences the actual volume of hollow channels, the printable material should be further optimized in order to achieve better buildability and mitigate the squeezing of hollow channels from the upper layers.

8.4.2. INFLUENCE OF PRINTING DIRECTION ON THE PORES

Compared with the cast samples, 3D-printed samples have higher porosity due to the layer-by-layer printing process [18]. Therefore, the influence of printing direction on

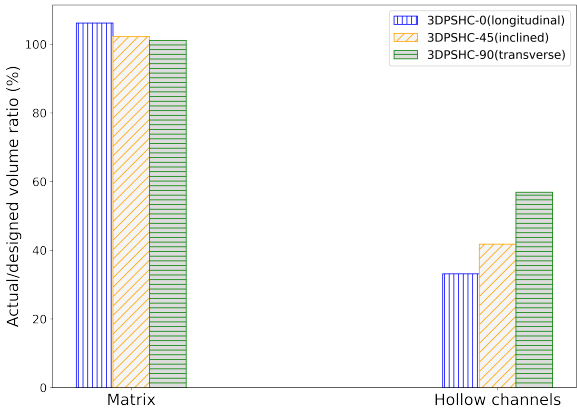


Figure 8.8: Reconstructed CT scan results of 3D-printed mortar with hollow channels.

the porosity is also investigated by comparing the volume of small pores (i.e., those that occur purely as a consequence of the printing process) (Figure 8.9). Note that the pores connected to the designed hollow channels are regarded as part of the ‘vascular network’ in this study.

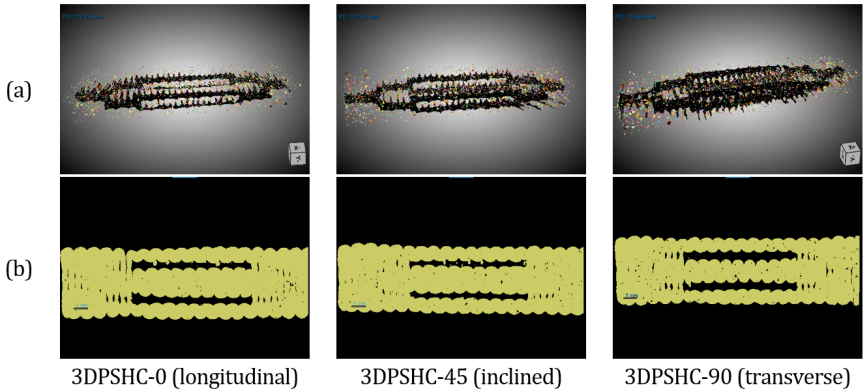


Figure 8.9: Sliced CT results of 3D-printed mortar with hollow channels. (a) Reconstructed hollow channels and pores (black: hollow channels; colorful: small pores); (b) Vertical sections (yellow: matrix; black: hollow channels or small pores).

Additional small pores are present in all specimens (Figure 8.9). Compared with the inclined- and longitudinally printed samples, there are more additional pores in the transversely printed one. The total volumes of additional pores are calculated based on CT scanning (Figure 8.10). Note that only pores larger than the XCT resolution are considered.

The volume of small pores increases when the printing direction changes from

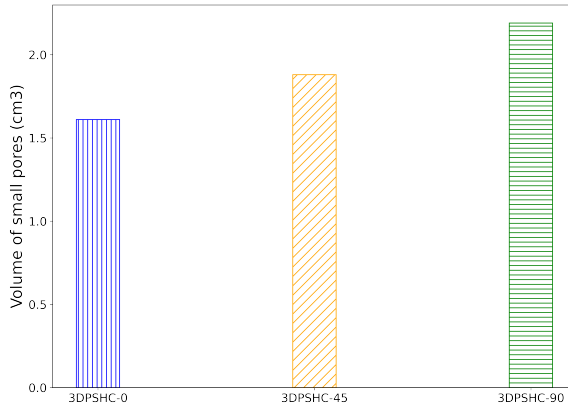


Figure 8.10: Volume of small pores of specimens printed in different direction.

longitudinal (0°) to transverse (90°) (Figure 8.10). The volume of the cementitious matrix in longitudinally printed specimens is larger than the other two groups (see Figure 8.8). As a result, the larger self-weight load of upper layers squeezes not only the hollow channels, but also the small pores.

8.5. FRACTURE BEHAVIOR

8.5.1. INITIAL FLEXURAL STRESS

THE fracture behavior of the virgin samples is first investigated through 4-point bending test. The stress-crack width curves of specimens printed in 3 different directions are shown Figure 8.11.

Flexure stress/crack width curves are significantly influenced by printing direction (Figure 8.11). The flexural strength of the longitudinally printed specimens is higher than those of the inclined printed and transversely printed specimens. According to section 8.4, the possible reasons are the denser cementitious matrix (less pores) and the smaller volume hollow channels in the longitudinally printed specimens. Except for flexural strength, the stiffness of longitudinally- and inclined printed specimens is obviously larger than the transversely printed counterpart.

Different post-peak behavior is also observed for the three groups. Although the interlayers of transversely printed samples are parallel to the loading direction, the transversely printed samples still show ductile behavior. This could be a result of fibers bridging the cracks. In other words, cracks probably do not always occur in the interlayers. The flexural stress when unloading at the crack width of $450\mu\text{m}$ is defined as the residual flexural stress. However, the ductility of transversely- and inclined printed samples is higher than the transverse one due to the higher residual flexural stress. Compared with the transversely printed samples, there are more fibers bridging

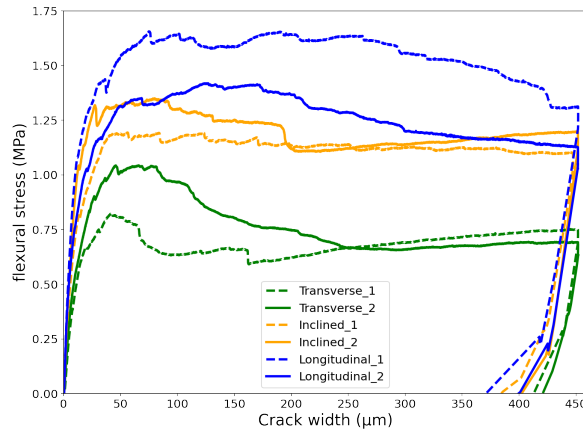


Figure 8.11: Flexural response comparison of specimens printed with different directions.

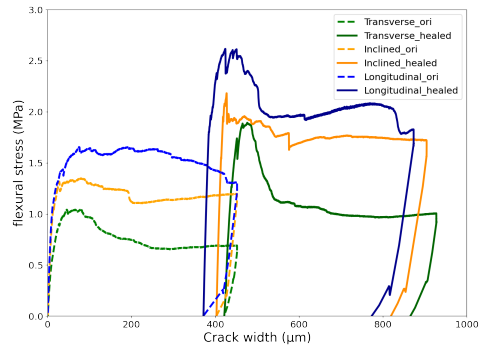
the cracks.

8.5.2. FLEXURAL STRENGTH OF THE HEALED SAMPLES

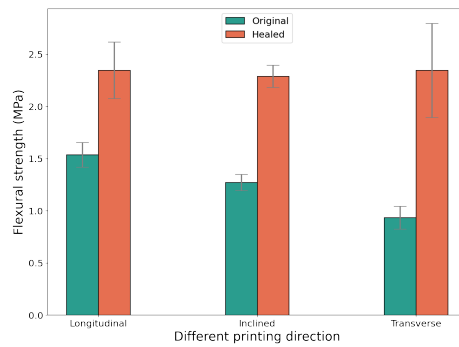
After the first round of 4-point bending test, epoxy resin was injected to seal the cracks. Another round of 4-point bending was carried out on the healed samples. Based on chapter 2, the healing performance could be estimated with healing efficiency (Equation 2.4) and load recovery index (Equation 2.5). The result is shown in Figure 8.12

All specimens regain flexural strength after the healing process (Figure 8.12(a)). Similar to chapter 4, the residual load-bearing capacity of the healed samples is higher than the original ones. In particular, the residual flexural stress of inclined and longitudinally printed specimens is much higher than the transverse one. The change of flexural strength can be seen in Figure 8.12(b). The average flexural strength of longitudinally printed samples is the largest amongst the three groups. Compared with the other two groups, there are less defects in the longitudinally printed samples. As a result, most of the injected epoxy resin flows into the crack thereby sealing it. However, except for filling the crack, the injected epoxy resin may also fill the printing defects since enough epoxy resin (30ml) was supplied during the healing process. As a result, the healing efficiency of transversely printed samples is also remarkable. Note that the variance in transversely printed samples is larger than in the other two groups.

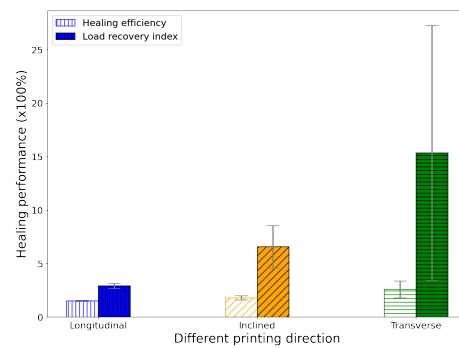
As to the influence of printing direction on healing performance, it is found that the healing efficiency and load recovery index of three groups show the same trend (see Figure 8.12(c)). The overall self-healing performance of the 3D-printed samples improves when the printing direction changes from longitudinal to transverse. However, compared with healing efficiency, the change of load recovery index is more obvious due to the relatively low initial flexural strength of transversely printed samples. Furthermore, the variance of load recovery index of transversely printed sample is



(a)



(b)



(c)

Figure 8.12: Flexural response comparison of the healed specimens (a) flexural stress-crack width curve; (b) Flexural strength comparison of healed samples printed in different directions; (c) Healing performance of sample printed in different directions..

extremely large compared with other two groups.

8.6. WATER TIGHTNESS

EXCEPT for flexural stress, the water permeability of the cracked samples is also investigated. The water permeability of the cracked samples before injecting epoxy resin is shown in Figure 8.13.

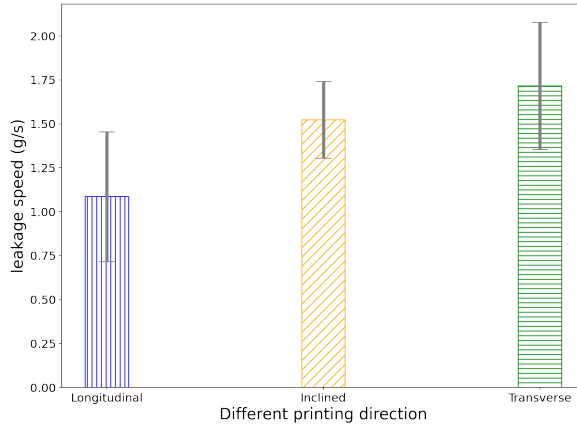


Figure 8.13: Flow speed of leaked water of specimens printed in different directions.

The permeability of cracked samples is also influenced by the printing direction (see Figure 8.13). When the printing direction changes from longitudinal to transverse, the average permeability of the samples increases. There are two reasons for the increase of permeability. On the one hand, the amount of printing defects increases when the printing direction changes (see Figure 8.10). On the other hand, from Figure 8.11, the final crack width (i.e., after unloading) decreases when printing direction changes from longitudinal to transverse. Therefore, the average permeability of transversely printed specimens is larger than that of the longitudinally printed ones. It is worth mentioning that the variance of the permeability is very large for all of the three groups. This is probably caused by the variability in the printing quality which inevitably exists even when the printing direction is the same.

As to the water permeability of the healed specimens, no leaked water was observed for all the samples. Besides, the epoxy resin could not be injected through both of the two outlets. Therefore, it is hard to evaluate the water tightness recovery in this study. It is inferred that the hardened epoxy resin blocks the hollow channels although pressurized air was blown to remove the extra epoxy in the hollow channels. The rough surface of the hollow channels (see Figure 8.7 makes it difficult to blow the epoxy resin out of the specimens. In order to perform multiple healing events with the 3D-printed mortar with hollow channels, this problem should be addressed. More importantly, the squeezing from the upper layers allows for the hollow channels be easily blocked with

the epoxy resin. In order to perform multiple healing events with the 3D-printed mortar with hollow channels, the squeezing to the hollow channels should be addressed from the aspect of printable materials. Furthermore, squeezing of hollow channels during the printing process should be considered when designing the vascular system in the future study.

8.7. CONCLUSIONS

IN this study, vascular self-healing cementitious material is directly ink written by reserving hollow channels in the cementitious matrix as the path for healing agent transportation. The rheology of the designed fiber reinforced mortar was first investigated. Afterwards, vascular self-healing cementitious materials were fabricated, where the top and bottom two printing layers were printed in three different directions (i.e., longitudinal, inclined and transverse). The influence of printing direction on the microstructure of 3D-printed specimens was investigated through CT scanning. Furthermore, 4-point bending tests were performed to assess the flexural strength as well as the flexural strength regain after injecting epoxy resin as the healing agent. The water tightness of the cracked specimens printed in different directions was also measured. Based on the results, the following conclusions could be drawn:

- The actual volumes of hollow channels are much smaller than the designed volume, with more than 40% of the hollow channels being squeezed by the upper layers during the printing process. The amount of “squeezing” depends on the printing direction. The volume of small pores is also influenced by printing direction: it increases when the printing direction changes from longitudinal to transverse. Although printing direction influences the actual volume of hollow channels, the printable material should be further optimized in order to achieve better buildability and mitigate the squeezing of hollow channels from the upper layers.
- The flexural strength of 3D-printed samples is influenced by the printing direction. The longitudinally printed specimen has the highest initial flexural strength amongst the three groups, followed by inclined printed specimens. The residual stress of longitudinally printed specimens is also the highest. A possible reason is that more fibers bridge the cracks in longitudinally printed samples.
- The flexural strength regain of the three groups is remarkable since all of the samples have the healing effectiveness of over 100%. The average flexural strength of longitudinally printed samples is the largest amongst the three groups. However, only one healing process could be carried out due to the blockage of hollow channels. The rough surface of the hollow channels makes it difficult to blow the epoxy resin out of the specimens. Except for improving the printing materials, squeezing of hollow channels during the printing process should be considered when designing the vascular system to enable multiple healing events in the future study.
- When the printing direction changes from longitudinal to transverse, the average water permeability of the samples before healing increases. The water tightness

recovery after the healing process is unknown due to the blockage of hollow channels.

REFERENCES

- [1] Z. Wan, Y. Xu, S. He, Y. Chen, J. Xie, and B. Šavija, *Direct ink writing of vascularized self-healing cementitious composites*, Cement and Concrete Composites , 105295 (2023).
- [2] S. Bhattacharjee, A. S. Basavaraj, A. Rahul, M. Santhanam, R. Gettu, B. Panda, E. Schlangen, Y. Chen, O. Copuroglu, G. Ma, *et al.*, *Sustainable materials for 3d concrete printing*, Cement and Concrete Composites **122**, 104156 (2021).
- [3] Y. Chen, S. He, Y. Zhang, Z. Wan, O. Çopuroğlu, and E. Schlangen, *3d printing of calcined clay-limestone-based cementitious materials*, Cement and Concrete Research **149**, 106553 (2021).
- [4] C. Gosselin, R. Duballet, P. Roux, N. Gaudillière, J. Dirrenberger, and P. Morel, *Large-scale 3d printing of ultra-high performance concrete—a new processing route for architects and builders*, Materials & Design **100**, 102 (2016).
- [5] A. Perrot, A. Pierre, V. Nerella, R. Wolfs, E. Keita, S. Nair, N. Neithalath, N. Roussel, and V. Mechtcherine, *From analytical methods to numerical simulations: A process engineering toolbox for 3d concrete printing*, Cement and Concrete Composites **122**, 104164 (2021).
- [6] M. Moini, J. Olek, J. P. Youngblood, B. Magee, and P. D. Zavattieri, *Additive manufacturing and performance of architected cement-based materials*, Advanced Materials **30**, 1802123 (2018).
- [7] A. L. van Overmeir, S. C. Figueiredo, B. Šavija, F. P. Bos, and E. Schlangen, *Design and analyses of printable strain hardening cementitious composites with optimized particle size distribution*, Construction and Building Materials **324**, 126411 (2022).
- [8] Y. W. D. Tay, Y. Qian, and M. J. Tan, *Printability region for 3d concrete printing using slump and slump flow test*, Composites Part B: Engineering **174**, 106968 (2019).
- [9] Z. Chang, M. Liang, Y. Xu, Z. Wan, E. Schlangen, and B. Šavija, *Early-age creep of 3d printable mortar: Experiments and analytical modelling*, Cement and Concrete Composites **138**, 104973 (2023).
- [10] Y. Chen, S. Chaves Figueiredo, Ç. Yalçinkaya, O. Çopuroğlu, F. Veer, and E. Schlangen, *The effect of viscosity-modifying admixture on the extrudability of limestone and calcined clay-based cementitious material for extrusion-based 3d concrete printing*, Materials **12**, 1374 (2019).
- [11] S. Hou, Z. Duan, J. Xiao, and J. Ye, *A review of 3d printed concrete: Performance requirements, testing measurements and mix design*, Construction and Building Materials **273**, 121745 (2021).
- [12] Y. Chen, M. Liang, Y. Zhang, Z. Li, B. Šavija, E. Schlangen, and O. Çopuroğlu, *Can superabsorbent polymers be used as rheology modifiers for cementitious materials in the context of 3d concrete printing?* Construction and Building Materials **371**, 130777 (2023).

- [13] F. De Larrard, C. Ferraris, and T. Sedran, *Fresh concrete: a herschel-bulkley material*, Materials and structures **31**, 494 (1998).
- [14] I. Ivanova and V. Mechtcherine, *Possibilities and challenges of constant shear rate test for evaluation of structural build-up rate of cementitious materials*, Cement and Concrete Research **130**, 105974 (2020).
- [15] C. D. Murray, *The physiological principle of minimum work applied to the angle of branching of arteries*, The Journal of general physiology **9**, 835 (1926).
- [16] S. Sangadji and E. Schlangen, *Self healing of concrete structures-novel approach using porous network concrete*, Journal of Advanced Concrete Technology **10**, 185 (2012).
- [17] E. Tziviloglou, V. Wiktor, H. Jonkers, and E. Schlangen, *Bacteria-based self-healing concrete to increase liquid tightness of cracks*, Construction and Building Materials **122**, 118 (2016).
- [18] Y. Chen, O. Çopuroğlu, C. R. Rodriguez, F. F. de Mendonca Filho, and E. Schlangen, *Characterization of air-void systems in 3d printed cementitious materials using optical image scanning and x-ray computed tomography*, Materials Characterization **173**, 110948 (2021).

9

CONCLUSIONS AND RECOMMENDATIONS

In this chapter, a brief summary of this thesis is given. Based on the obtained results, some general conclusions are drawn. Finally, recommendations are presented for the future research.

9.1. SUMMARY

AMONG the possible crack-repair strategies for concrete structures, self-healing concrete is promising as cracks are repaired with no or little human intervention. Compared with other self-healing approaches, the vascular system embedded in the cementitious matrix is capable of supplying healing agents to the cracked region in a continuous way or multiple times [1]. Although extensive research has been devoted to understanding and improving vascular self-healing cementitious materials, early designs of vascular networks have been relatively simple due to the use of brittle materials such as glass tubes. The recent development of additive manufacturing (AM) enables fabricating and tailoring vascular networks with complicated geometry. However, the influence of printing parameters on the properties of self-healing cementitious materials with 3D-printed vascular networks has not been fully understood. Besides, the mechanical response of self-healing cementitious materials with different vascular configurations has been extensively studied. In this thesis, the application of additive manufacturing in vascular self-healing cementitious materials was investigated.

After a general introduction (**Chapter 1**) and literature review of vascular self-healing concrete (**Chapter 2**) given in Part 1, the influence of printing parameters on the properties of self-healing concrete embedded with 3D-printed vascular networks was experimentally investigated in the second part of this study (**Chapter 3** and **Chapter 4**). Two commonly used commercial printing filaments, i.e., Acrylonitrile Butadiene Styrene (ABS) and Polyvinyl Alcohol (PVA), were used to fabricate the vascular systems. In particular, the influence of printing direction and printing layer-height on the initial properties and the healing effectiveness of specimens with ABS octet-shape vasculature are discussed (**Chapter 3**). The dissolution of vascular tubes printed in different directions was studied when the vascular network was created using PVA. A possible approach to minimize the chemical reaction between the PVA vasculature and the cementitious matrix (and thereby limit its dissolution) – the use of wax coating – was explored as well (**Chapter 4**).

The third part of the thesis (**Chapter 5–Chapter 7**) focuses on numerical simulation and optimization of self-healing vascular cementitious materials. In **Chapter 5**, the mechanical behaviour of self-healing cementitious materials with 3D printed ABS vasculature was studied using the concrete damage plasticity model (CDPM) in Abaqus software. In addition, the self-healing cementitious materials with different vascular configurations were numerically investigated through 2D models. Based on the obtained results, it is noted that vascular configurations have significant influences on the flexural stress and it is necessary to optimize the vascular configuration towards different target properties. In **Chapter 6** and **Chapter 7**, two different machine learning approaches, i.e., generative deep neural network (GDNN) and deep reinforcement learning (DRL) were employed to optimize the vascular configuration towards higher peak load or toughness when 4 pores are placed in the middle span of the notched beam under 3-point bending.

In **Chapter 8**, instead of creating a vascular network (or hollow channels) using thermoplastic materials, self-healing mortar is directly printed with hollow channels as vascular network. The influence of printing direction (i.e., longitudinal, inclined and

transverse) on the volume of hollow channels, mechanical properties and healing effectiveness is discussed.

9.2. CONCLUSIONS

B^{ASED} on the obtained results in each chapter, some general conclusions can be drawn:

- *The printing parameters have a marked influence on the properties of self-healing cementitious materials with 3D-printed ABS vascular network.*

The specimens with horizontally printed vascular networks have higher flexural strength than those with vertically printed networks. Vascular networks printed with smaller layer height have less influence on the initial flexural strength of vascular self-healing cementitious composites compared with those printed with a larger layer height. The specimens with 3D-printed vasculature show good self-healing properties when using epoxy resin as the healing agent. When performing multiple healing events, horizontally printed vascular self-healing cementitious materials have higher flexural strength than the vertically-printed counterparts. However, the influence of printing layer height decreases as the number of healing events increases.

- *The dissolution of PVA vasculature in the cementitious matrix is influenced by the printing direction, wall thickness and wax coating.*

The reaction between PVA and the cementitious matrix prevents the PVA tubes from dissolving, making coating of the tubes necessary (e.g., with wax). The vertically-printed PVA tubes dissolve better than the horizontally printed ones. The dissolution of coated PVA tubes in the vascular system is excellent, as shown by X-ray tomography. The water tightness of the cracked 3D vascular specimens is much better than that of the 2D counterpart after the initial 4-point bending test. Besides, the cementitious mortar embedded with 3D vascular network has higher healing potential than the ones with 2D vascular networks.

- *Accurate simulation on the fracture behavior of vascular self-healing cementitious composites could be achieved using CDPM in Abaqus software; The 2D model is the most suitable model for generating dataset.*

The simulated stress-crack width by CDPM in Abaqus has shown excellent agreement with experimental results, in terms of crack width and flexural strength under 4-point bending. The 2D model with different pore configurations shows different flexural response in terms of peak load and toughness. After comparing the computation time and mapping relationship, 2D model with pores in the middle span is the most suitable model for generating dataset for vascular configuration optimization through machine learning (ML) approach.

- *GDNN can be used to optimize the vascular configuration of self-healing concrete; The correction step introduced in the optimization algorithm helps increase the convergence and optimization effectiveness.*

A deep neural network (DNN) can accurately predict peak load or toughness

based on concrete structures, which is a precondition for optimization with GDNN. Compared with the original GDNN, there are less unique structures after the optimization process using corrected GDNN. Besides, the average target properties (peak load/toughness) obtained by corrected GDNN is much higher than that of original GDNN.

- *It is feasible to optimize the vascular configuration through the DRL approach.*
A Markov Decision Process (MDP) can be formed to turn the vascular optimization in the RL framework. The structure with highest peak load or toughness of 3-pore concrete structures is accessed in all runs through two updating strategies. However, compared with peak load, it is more difficult for the RL agent to converge when optimizing concrete for high toughness. The RL optimization method is able to identify the structure with high toughness in the new optimization task for 4-pore concrete structure. As such, the method can be a powerful tool to automatically optimize structure towards higher target property.
- *The printing direction influences the flexural strength and strength recovery of the 3D-printed mortar with hollow channels as vascular networks.*
For the 3D-printed mortar with hollow channels, the actual volumes of hollow channels are much smaller than the designed volume, with more than 40% of the hollow channels being squeezed by the upper layers during the printing process. The amount of “squeezing” depends on the printing direction. The flexural strength of 3D-printed samples is also influenced by the printing direction: the longitudinally printed specimens have the highest initial flexural strength amongst the three groups, followed by inclined printed specimens. The flexural strength regain of the three groups is remarkable since all of the samples have the healing effectiveness of over 100%. The average flexural strength of longitudinally printed samples is the largest amongst the three groups. However, only one healing process could be carried out due to the blockage of hollow channels. The rough surface of the hollow channels makes it difficult to blow the epoxy resin out of the specimens.

9

9.3. RECOMMENDATIONS

IN this research, an investigation was carried out for the utilization of additive manufacturing in vascular self-healing cementitious materials. Although many issues were addressed, there are areas which need further exploration. In the future, the following related topics could be done:

- The potential for real-scale applications of self-healing concrete with 3D printed vascular networks should be explored. In this study, the size of vascular networks printed with plastic materials (i.e., ABS, PLA or PVA) was relatively small due to the limitations of the 3D printer used. Furthermore, mortar was used in all experiments, not concrete. Although some researchers investigated the use of vascular self-healing cementitious materials in practical applications [2, 3], the vascular networks used were relatively simple. Therefore, further research would

be needed before the complex vascular networks developed herein could be applied in practice.

- A reliable method for coating of sacrificial PVA should be developed. Although the coated PVA tubes in the cementitious matrix were dissolvable (Chapter 4), the dissolution process is time-consuming and is greatly influenced by the printing configuration. Furthermore, the PVA tubes were manually coated herein, making the coating layer uneven and susceptible to defects. For practical applications, an automatic and robust coating method should be developed.
- The optimization of vascular configuration should be extended towards more realistic scenarios, e.g., considering different loading conditions and the influence of structural parameters such as presence of steel reinforcement. In the current optimization approach, the vascular network was simplified as pores in the middle span of the 2D beam to reduce the computational burden. It is noted that the optimization of vascular self-healing concrete reinforced by rebars could be much complicated since the influence of vascular configuration on mechanical response will be much smaller compared with the influence from rebar. Furthermore, the vascular network is optimized when the specimens were under 3-point bending. Clearly, these cases are simple, and the methods must be extended before they could be useful for practice.
- Direct ink writing for self-healing composites with hollow channels should be further explored in terms of different printing (cementitious) materials and geometries. The feasibility of direct ink writing of vascular self-healing mortar has been shown in Chapter 8. However, only one healing event could be carried out due to the blockage of vascular network. This could potentially be overcome by using different vascular designs and/or different printing materials (i.e., mortars with adjusted rheology).
- An automatic injection system for healing should be developed. In this thesis, the healing agent was manually injected to seal the cracks. A system enabling the automatic healing process could be developed to realize the aim of “self-healing”, as proposed by Sangadji and Schlangen [4]. The future system could be coupled with an advanced crack monitoring system, which could be either external on the structure or incorporated as part of the (printed) vascular network. Such a system would then automatically trigger the healing event.

REFERENCES

- [1] C. De Nardi, B. L. Freeman, D. Gardner, and T. Jefferson, *Mechanical response and predictive modelling of vascular self-healing cementitious materials using novel healing agents*, *Cement and Concrete Composites* **142**, 105143 (2023).
- [2] R. Davies, T. Jefferson, and D. Gardner, *Development and testing of vascular networks for self-healing cementitious materials*, *Journal of Materials in Civil Engineering* **33**, 04021164 (2021).
- [3] R. Davies, M. Pilegis, A. Kanellopoulos, T. Sharma, O. Teall, D. Gardner, A. Jefferson, and R. Lark, *Multi-scale cementitious self-healing systems and their application in concrete structures*, (2016).
- [4] S. Sangadji and E. Schlangen, *Self healing of concrete structures-novel approach using porous network concrete*, *Journal of Advanced Concrete Technology* **10**, 185 (2012).

ACKNOWLEDGMENTS

PhD study is a journey full of adventures. At the end of this track, I would like to express my sincere gratitude to my colleagues and friends who help me enjoy this journey.

My special appreciation goes to China Scholarship Council (CSC), whose financial support enables me to cozily accomplish the PhD work at Microlab, Section of Materials and Environment, Faculty of Civil Engineering and Geosciences, Delft University of Technology, the Netherlands.

First of all, I would like to thanks my promoter Prof. Erik Schlangen. I appreciate the opportunity to study in TU Delft. Self-healing concrete was totally a new field for me when I obtained the PhD offer 4 years ago, but I am quickly into this field since he is always ready to help. The discussions with him always inspire me. Although the conversations often start with “Hi Erik, do you have five minutes?”, the discussions are much longer for most of the time. In daily life, he is person with kindness and humor. I really enjoy the amazing (*gezellig*) environment he created for the whole research group. Both the coffee break and group meetings are equally academic as well as joyful.

I also would like to thank the other promoter Dr. Branko Šavija. It is really a big fortune for me to have such a promoter. I still remember the time when I learned the basic knowledge about machine learning with him during the lock-down period in 2020. The weekly meeting with him drove me to learn new knowledge in a *gradient-decent* way. Thank him for helping me get in touch with the world of machine learning (ML). He is always energetic and high-efficiency. His rapid review of manuscripts puts me well ahead of (yaoyaolingxian) my Chinese friends from other research groups. So proud of him! His patience significantly encouraged me when I spent almost nine months to uncover one ML algorithm in the literature. More importantly, he is really a self-disciplined guy, who stays in good shape without workouts (at least I have not seen). He is such a person that interprets what an ideal young scholar should be.

Besides my promoters, I would like to give my appreciations to the chairperson and all other committee members for my PhD defence: Prof. E. Gruyaert, Dr. I.B.C.M Rocha, Prof. B. Han, Prof. H.M. Jonkers, Dr. S.J. Garcia, Prof. P. C. Louter. Thanks for spending time to review the manuscript and give insightful comments for improving my thesis.

I would like to give my gratitude to my officemates in the “best office”: Shi Xu, Wenjuan Lyu, Xingliang Yao, Xuhui Liang (Yaowen Xu), Jinbao Xie (Advertise for Rent), and Guilherme da Silva Munhoz. I am so lucky to spend the past four years with all of you. It is an office always full of happiness and warmth. Dear G, keep in mind that the destined site for office dinner is the Greek restaurant although we may have a lot of alternatives.

I also would like to thank my colleagues and friends in Microlab: Dr. Guang Ye, Prof. Klaas van Breugel, Dr. Mohammad Fortouhi, Dr. Oğuzhan Çopuroğlu, Dr. Mladena Luković, Dr. Gozde Ozerkan, Dr. Marc Ottele, Dr. Dessi Koleva, Zhiwei Qian, Tianshi Lu, Jiayi Chen, Bei Wu, Xuliang Hou, Mayank Gupta, Reza Mohammad, Zhenming Li (Na


Li), Yu Zhang, Fernando Mendonca Filho, Emanuele Rossi, Yidong Gan (Jingcun Chen), Yu Chen, Yask Kulshreshtha, Bart Hendrix, Max Veeger, Ze Chang (Lu Cheng), Albina Kostiuhenko, Zhaozheng Meng, Rowin Bol, Hua Dong, Shizhe Zhang (Kelly Mao), Boyu Chen, Zhiyuan Xu, Burcu Aytekin Turkoglu, Yading Xu, Ameya Kamat, Claudia Romero Rodriguez, Stefan Chaves Figueiredo, Marija Nedeljković, Farnaz Aghabeyk, Minfei Liang, Anne Linde van Overmeir, Patrick Holthuizen, Chen Liu, Hu Shi, Ali Ghaderiaram, Luiz Miranda de Lima Junior, Irving Alfredo Flores Beltran, Yu Zeng, Shan He (Zejia Zheng), Fanxiang Xu, Langzi Chang (Xinrui Zhang), Yitao Huang, Zhenxu Qian, Hao Cheng, Yubao Zhou, Dawei Gu, Shozab Mustafa and Kuba Pawlowicz. Thanks for the friendship, the coffee time, the parties and all the great time we shared together.

My great appreciations also go to the support staffs in Microlab. Many thanks to Maiko van Leeuwen and his family! He is such a kind and patient guy. Although he is busy travelling between Microlab and Macrolab every day, he is always ready to help. I was deeply impressed by the safety-instruction when I entered microlab for the first time. He showed me how much he treasured the equipment in “Maiko’s lab”. I enjoy the Dutch-Chinese teaching and learning, BBQ and other fancy activities with him. I also would like to thank (Meneer) Arjan Thijssen, who helps me a lot in CT scanning experiments and shares his marvelous stories. Thank John van den berg and Ton Blom. They always wear smiles on face and say hello to me in any corner of TU when we meet. Besides, I would like to thank the secretaries of 3MD: Jaap Meijer, Jacqueline Bergenhenegouwen, Iris Nederhof-van Woggelum and Sandra Schuchmann-Hagman. They always prepare some surprises on holidays.

My gratitude goes to my fitness friends and coaches in X: Pei He, Yun Chen, Shamangi Kooistra and Salil Luesutthiviboon. Although my weight has not decreased a lot (I believe it will), I really enjoy the time we spend together in the gym. Thanks for encouraging/forcing me to challenge myself for new tracks or larger weight (for body power). *No annoyance cannot be diluted by a 2-hour fitness; if there is, then go to the aerobics track!*

I also would like to thank my teachers and friends in China. Many thanks to my master supervisors Prof. Jian Liu and Prof. Bo Han for encouraging to pursue my dream to be a researcher. Many thanks to Rui Shu, Hongyun Tian, Pengfei Xiang, Zuodong Xiong and Rui Liu. Their friendship helps me pass the most difficult moment during the PhD study.

Finally, I would like to express my deepest gratitude to my family members. Many thanks to my parents and parents-in-law for their understanding and tolerance. Thanks to my lovely wife Jing Chen! Her unconditional support is the greatest driving force for my graduation “on time”. She makes another home for me in Delft.



Delft, Oct 2023

CURRICULUM VITÆ

Zhi WAN

08-10-1991 Born in Hubei, China.

EDUCATION

2010–2014 Undergraduate in Civil Engineering
Huazhong University of Science and Technology, China

2010–2014 Undergraduate in Japanese (Minor)
Huazhong University of Science and Technology, China

2016–2019 Postgraduate in Structural Engineering
Shandong University, China

2019–2023 PhD student
Delft University of Technology, the Netherlands
Thesis: Application of additive manufacturing in vascular
self-healing cementitious materials
Promotor: Dr. B. Šavija & Prof. dr. E. Schlangen

Email zhiwan521@yeah.net

LIST OF PUBLICATIONS

JOURNAL PUBLICATIONS

1. **Z. Wan**, Y. Xu, and B. Šavija, *On the use of machine learning models for prediction of compressive strength of concrete: influence of dimensionality reduction on the model performance*, [Materials](#) **14**, 713 (2021).
2. **Z. Wan**, Y. Xu, Y. Zhang, S. He, and B. Šavija, *Mechanical properties and healing efficiency of 3D-printed ABS vascular based self-healing cementitious composite: Experiments and modelling*, [Engineering Fracture Mechanics](#) **267**, 108471 (2022).
3. **Z. Wan**, Z. Chang, Y. Xu, and B. Šavija, *Optimization of vascular structure of self-healing concrete using deep neural network (DNN)*, [Construction and Building Materials](#) **364**, 129955 (2023).
4. **Z. Wan**, Z. Chang, Y. Xu, Y. Huang, and B. Šavija, *Inverse Design of Digital Materials Using Corrected Generative Deep Neural Network and Generative Deep Convolutional Neural Network*, [Advanced Intelligent Systems](#) **5**, 2200333 (2023).
5. **Z. Wan**, Y. Zhang, Y. Xu, and B. Šavija, *Self-healing cementitious composites with a hollow vascular network created using 3D-printed sacrificial templates*, [Engineering Structures](#) **289**, 116282 (2023).
6. **Z. Wan**, Y. Xu, S. He, Y. Chen, J. Xie, and B. Šavija, *Direct ink writing of vascularized self-healing cementitious composites*, [Cement and Concrete Composites](#) **144**, 105295 (2023).
7. **Z. Wan**, Y. Xu, Z. Chang, M. Liang, and B. Šavija, *Automatic enhancement of vascular configuration for self-healing concrete through deep reinforcement learning approach*, submitted to journal.
8. **Z. Wan**, Y. Xu, S. He, E. Schlangen, and B. Šavija, *Additive manufacturing in self-healing cementitious materials: A state-of-the-art review*, submitted to journal.
9. Z. Chang, **Z. Wan**, Y. Xu, E. Schlangen, and B. Šavija, *Convolutional neural network predicting crack pattern and stress-crack width curve of air-void structure in 3D printed concrete*, [Engineering Fracture Mechanics](#) **271**, 108624 (2022) (Correspondence).
10. Y. Zhang, **Z. Wan**, L.M. de Lima Junior, and O. Çopuroğlu, *Early age hydration of model slag cement: Interaction among C3S, gypsum and slag with different Al₂O₃ contents*, [Cement and Concrete Research](#) **161**, 106954 (2022)
11. S. He, **Z. Wan**, Y. Chen, H. M. Jonkers, and E. Schlangen, *Microstructural characterization of crack-healing enabled by bacteria-embedded polylactic acid (PLA) capsules*, [Cement and Concrete Composites](#) **143**, 105271 (2023)

12. M. Liang, Z. Chang, **Z. Wan**, Y. Gan, E. Schlangen, and B. Šavija, *Interpretable Ensemble-Machine-Learning models for predicting creep behavior of concrete*, [Cement and Concrete Composites](#) **125**, 104295 (2022)
13. J. Xie, Y. Xu, **Z. Wan**, A. Ghaderiaram, E. Schlangen, and B. Šavija, *Auxetic cementitious cellular composite (ACCC) PVDF-based energy harvester*, [Energy and Buildings](#) **298**, 113582 (2023)
14. Y. Xu, Y. Gan, Z. Chang, **Z. Wan**, E. Schlangen, and B. Šavija, *Towards understanding deformation and fracture in cementitious lattice materials: Insights from multiscale experiments and simulations*, [Construction and Building Materials](#) **345**, 128409 (2022).
15. Y. Chen, S. He, Y. Zhang, **Z. Wan**, O. Çopuroğlu, and E. Schlangen, *3D printing of calcined clay-limestone-based cementitious materials*, [Cement and Concrete Research](#) **149**, 106553 (2021)
16. M. Liang, Y. Gan, Z. Chang, **Z. Wan**, E. Schlangen, and B. Šavija, *Microstructure-informed deep convolutional neural network for predicting short-term creep modulus of cement paste*, [Cement and Concrete Research](#) **152**, 106681 (2022)

CONFERENCE PROCEEDINGS

1. **Z. Wan**, and B. Šavija, *Mechanical properties and healing efficiency of 3D-printed ABS vascular based self-healing cementitious composite*, 8th International Conference on Self-Healing Materials, Milan, Italy, 2022.
2. **Z. Wan**, Y. Xu, and B. Šavija, *Influence of printing direction on 3D-printed vascular based self-healing cementitious composites*, [SMARTINCS'23 Conference on Self-Healing, Multifunctional and Advanced Repair Technologies in Cementitious Systems](#), Gent, Belgium, 2023.
3. **Z. Wan**, Y. Xu, Z. Chang, and B. Šavija, *Optimization of vascular structure of self-healing concrete using generative deep neural network (GDNN)*, ASCE EMI 2023 Conference, Atlanta, USA, 2023.